



A U Š R A G A D E I K Y T Ė

**MULTISCALE MODELS
AND ALGORITHMS
FOR THE SIMULATION
OF HEAT AND
MOISTURE TRANSFER
IN TEXTILE
STRUCTURES**

D O C T O R A L D I S S E R T A T I O N

K a u n a s
2 0 2 2

KAUNAS UNIVERSITY OF TECHNOLOGY

AUŠRA GADEIKYTĖ

MULTISCALE MODELS AND ALGORITHMS
FOR THE SIMULATION OF HEAT AND
MOISTURE TRANSFER IN TEXTILE
STRUCTURES

Doctoral dissertation
Natural Sciences, Informatics (N 009)

Kaunas, 2022

This doctoral dissertation was prepared at Kaunas University of Technology, Faculty of Informatics, Department of Applied Informatics during the period of 2015–2020 and 2021–2022.

The doctoral right has been granted to Kaunas University of Technology together with Vytautas Magnus University and Vilnius Gediminas Technical University.

Dissertation is defended externally.

Scientific Advisor:

Prof. Habil. Dr. Rimantas BARAUSKAS (Kaunas University of Technology, Natural Sciences, Informatics, N 009).

Edited by: English language editor Brigita Brasiienė (Publishing House “Technologija”), Lithuanian language editor Violeta Meiliūnaitė (Publishing House “Technologija”).

Dissertation Defence Board of Informatics Science Field:

Prof. Dr. Vacius JUSAS (Kaunas University of Technology, Natural Sciences, Informatics, N 009) – **chairperson**;

Prof. Habil. Dr. Rimantas KACIANAUSKAS (Vilnius Gediminas Technical University, Technological Sciences, Mechanical Engineering, T 009);

Prof. Dr. Alfonsas MISEVIČIUS (Kaunas University of Technology, Natural Sciences, Informatics, N 009);

Prof. Habil. Dr. Minvydas Kazys RAGULSKIS (Kaunas University of Technology, Natural Sciences, Informatics, N 009);

Prof. Dr. Miguel Angel Fernandez SANJUAN (Rey Juan Carlos University, Spain, Natural Sciences, Informatics, N 009).

The official defence of the dissertation will be held at 10 a.m. on 25 March, 2022 at the public meeting of Dissertation Defence Board of Informatics Science Field in the Dissertation Defence Hall at Kaunas University of Technology.

Address: K. Donelaičio St. 73-403, 44249 Kaunas, Lithuania.

Tel. no. (+370) 37 300 042; fax. (+370) 37 324 144; e-mail doktorantura@ktu.lt

Doctoral dissertation was sent on 25 February, 2022.

The doctoral dissertation is available on the internet at <http://ktu.edu> and at the library of Kaunas University of Technology (K. Donelaičio St. 20, 44249 Kaunas, Lithuania), Vytautas Magnus University (K. Donelaičio Str. 52, Kaunas), and Vilnius Gediminas Technical University (Saulėtekio al. 14, 10223, Vilnius).

KAUNO TECHNOLOGIJOS UNIVERSITETAS

AUŠRA GADEIKYTĖ

DAUGIASKALIAI MODELIAI IR
ALGORITMAI ŠILUMOS IR DRĖGMĖS
MAINAMS TEKSTILĖS STRUKTŪROSE
SIMULIUOTI

Daktaro disertacija

Gamtos mokslai, informatika (N 009)

Kaunas, 2022

Disertacija rengta 2015–2020 ir 2021–2022 metais Kauno technologijos universiteto Informatikos fakultete, Taikomosios informatikos katedroje.

Doktorantūros teisė Kauno technologijos universitetui kartu su Vytauto Didžiojo universitetu ir Vilniaus Gedimino technikos universitetu.

Disertacija ginama eksternu.

Mokslinis konsultantas

prof. habil. dr. Rimantas BARAUSKAS (Kauno technologijos universitetas, gamtos mokslai, informatika, N 009).

Redagavo: anglų kalbos redaktorė Brigita Brasienė (leidykla „Technologija“), lietuvių kalbos redaktorė Violeta Meiliūnaitė (leidykla „Technologija“).

Informatikos mokslo krypties disertacijos gynimo taryba:

prof. dr. Vacius JUSAS (Kauno technologijos universitetas, gamtos mokslai, informatika, N 009) – **pirmininkas**;

prof. habil. dr. Rimantas KĄČIANAUSKAS (Vilniaus Gedimino technikos universitetas, technologijos mokslai, mechanikos inžinerija, T 009);

prof. dr. Alfonsas MISEVIČIUS (Kauno technologijos universitetas, gamtos mokslai, informatika, N 009);

prof. habil. dr. Minvydas Kazys RAGULSKIS (Kauno technologijos universitetas, gamtos mokslai, informatika, N 009);

prof. dr. Miguel Angel Fernandez SANJUAN (Rey Juan Carlos University, Ispanija, gamtos mokslai, informatika, N 009).

Disertacija bus ginama viešame Informatikos mokslo krypties disertacijos gynimo tarybos posėdyje 2022 m. kovo 25 d. 10 val. Kauno technologijos universiteto Disertacijų gynimų salėje.

Adresas: K. Donelaičio g. 73-403, 44249 Kaunas, Lietuva.

Tel. (370) 37 300 042; faks. (370) 37 324 144; el. paštas doktorantura@ktu.lt

Disertacija išsiųsta 2022 m. vasario 25 d.

Su disertacija galima susipažinti interneto svetainėje <http://ktu.edu> ir Kauno technologijos universiteto (K. Donelaičio g. 20, 44239 Kaunas), Vytauto Didžiojo universiteto (K. Donelaičio g. 52, Kaunas) ir Vilniaus Gedimino technikos universiteto (Saulėtekio al. 14, 10223 Vilnius) bibliotekose.

TABLE OF CONTENTS

ABBREVIATIONS	7
NOMENCLATURE	8
LIST OF FIGURES	9
LIST OF TABLES	11
INTRODUCTION	12
The aim and objectives of the work.....	13
The object of the research.....	14
Novelty and practical relevance	14
Statements for the defense.....	15
The approbation of research results.....	15
The layout of the thesis.....	15
1. LITERATURE REVIEW.....	15
1.1. The overview of thermal comfort properties of fabrics.....	18
1.2. The concept of multiscale modeling	21
1.3. The applications of finite element analysis in heat and mass transfer through textile.....	22
1.4. Permeability prediction using analytical and numerical models.....	29
1.5. Water-vapor resistance and water-vapor permeability.....	35
1.6. Thermal resistance.....	36
1.7. Concluding remarks	38
2. DEVELOPMENT OF THE RESEARCH TECHNIQUE.....	38
2.1. The concept of finite element method.....	39
2.2. The definition of representative volume element.....	41
2.3. A representative volume element of 3D textile structure in micro-scale	41
2.4. The numerical modeling of measurement of air permeability coefficient	46
2.5. The numerical modeling of measurement of water-vapor resistance.....	51
2.6. The numerical modeling of measurement of thermal resistance.....	54
2.7. Concluding remarks	57
3. NUMERICAL EXPERIMENTS.....	57
3.1. Verification and validation of air permeability coefficient	57
3.2. Verification and validation of water-vapor resistance coefficient	65
3.3. Verification and validation of thermal resistance coefficient.....	66
3.4. Concluding remarks	69
4. APPLICATION OF MODELS TO INVESTIGATE FABRICS WITH ADDITIONAL FUNCTIONALITY	70
4.1. The geometry of forced ventilation model	70
4.2. The boundary conditions of ventilation model.....	72
4.3. The analysis of heat and mass exchange through 3D textile.....	73
4.4. Forced ventilation model in macro-scale	76
4.5. Concluding remarks	79
CONCLUSIONS	80
SANTRAUKA	82

REFERENCES	109
CURRICULUM VITAE.....	118
ACKNOWLEDGEMENTS.....	119
PUBLICATIONS RELATED TO THE DISSERTATION.....	120
Appendix 1. The case study of <i>Model 1_a</i>	122

ABBREVIATIONS

1D – One-dimensional
2D – Two-dimensional
3D – Three-dimensional
CFD – Computational fluid dynamics
CFRP – Carbon fiber-reinforced composite
DSC – Differential scanning calorimetry
EMT – Effective media theory
FEA – Finite element analysis
FEM – Finite element method
ISO – International organization for standardization
PCM – Phase change materials
PES – Polyester
PP – Polypropylene
 Re – Reynolds number
RTM – Resin transfer molding
RVE – Representative volume element
SEM – Scanning electron microscope
 μ CT – Micro-X-ray computed tomography

NOMENCLATURE

Notation	Units	Definition
K	m ²	Permeability
p	Pa	Pressure
Δp	Pa	Pressure difference
p _{sat}	Pa	Saturation pressure
p _v	Pa	Partial pressure
ϵ_p	-	Porosity
AP	mm/s	Air permeability coefficient
T	K	Temperature
t	s	Time
u	m/s	Velocity
RH	%	Relative humidity
ϕ	-	Relative humidity
ρ	kg/m ³	Density
C	J/(kg·K)	Specific heat capacity
λ	W/(m·K)	Thermal conductivity
μ	Pa·s	Dynamic viscosity of the fluid
R	8.31 Jmol ⁻¹ K ⁻¹	Universal gas constant
A	m ²	Surface area
M _v	0.018 kg/mol	Water vapor molar mass
M _a	0.029 kg/mol	Dry air molar mass
D	m ² /s	Vapor diffusion coeff. in air
Δf		Laplacian of f : $\frac{\partial^2 f}{\partial x^2} + \frac{\partial^2 f}{\partial y^2} + \frac{\partial^2 f}{\partial z^2}$
∇f		Gradient of f : $\left[\frac{\partial f}{\partial x}, \frac{\partial f}{\partial y}, \frac{\partial f}{\partial z} \right]$
$\nabla \cdot \mathbf{u}$		Divergence of \mathbf{u} : $\frac{\partial u_1}{\partial x} + \frac{\partial u_2}{\partial y} + \frac{\partial u_3}{\partial z}$

NOTE: symbols in bold sign denote vectors and tensors, except cases commented directly in the text.

LIST OF FIGURES

Fig. 1.1. Levels of manufacturing process of textile composites	16
Fig. 1.2. Classification of three-dimensional textile preforms [7]; samples of 3D textile made from polypropylene and polyester	16
Fig. 1.3. A unit cell of woven fabrics shown three-dimensionally (a), a flat pattern view (b), and a schematic of plain weave pattern (c) [8].....	16
Fig. 1.4. Various weave styles for woven fabrics: plain, twill 2/1, 2 x 2 basket, crowfoot satin [11]; illustration of bi-ply fabrics [11] and a multi-chain unit cell of 2/2 twill weave [12].....	17
Fig. 1.5. Knitted fabric structures: cross-miss 1 x 1 plain knit, lacoste, interlock, and double pique [13], and weft-knit fabric [14]	17
Fig. 1.6. A scheme of multiscale modeling and common modeling techniques [27]	21
Fig. 1.7. Illustration of hierarchical multi-scale modeling strategies [34].....	22
Fig. 1.8. The main steps of FEM [51]	24
Fig. 1.9. A principle scheme of four different configurations of layers of suit and skin, simulated by the model [61]	27
Fig. 1.10. Idealized unidirectional reinforcement and a representative cell for quadratic (a) and hexagonal (b) fiber packing [81]	33
Fig. 1.11. Different scales and mathematical equations [89]	34
Fig. 1.12. Approximation of the plain knitted fabric [83]	35
Fig. 2.1. The geometry of sample 22/15 created with TexGen (a), imported geometry into Comsol Multiphysics (b), the same geometry after booleans operations in the Comsol Multiphysics environment (c)	44
Fig. 2.2. The work plane of xy, at height $z = 0.11$ mm; the work plane is depicted as a blue plane (a), top view of the geometry (b), the intersections between the yarns and the work plain are depicted in green (c)	44
Fig. 2.3. The generated coarser mesh; the blue color depicts the elements that are smaller than the minimum size of the element	44
Fig. 2.4. The general representation of RVE where x denotes the sample number..	46
Fig. 2.5. Boundary conditions of a unit cell of three-dimensional textile	49
Fig. 2.6. Boundary conditions of 3D textile and positions of operators	53
Fig. 2.7. Boundary conditions of one-layer textile, positions of operators and mesh	56
Fig. 3.1. RVE with boundary conditions a) and normalized local permeability, which was obtained with Gebart's analytical model and the proposed finite element model b)	58
Fig. 3.2. A convergence study between solution error and the number of iterations, considering a different number of mesh elements.....	59
Fig. 3.3. The effect of mesh size and air permeability (AP) coefficient.....	60
Fig. 3.4. The effect of different domain sizes of Model 1_a: 1 pore, 4 pores, 9 pores, 16 pores, are illustrated by a), b), c), d), respectively.....	60
Fig. 3.5. RVE of 16 pores of Model 1_a: the air flow distribution is depicted in a), the mesh quality in b), the element size in c)	62
Fig. 3.6. The air velocity distribution of Model 2_e.....	64

Fig. 3.7. The AP coefficients through-thickness of 3D textile models.....	64
Fig. 3.8. The temperature distribution of Model 1_a (solid matrix-polypropylene, fluid matrix-air), and on the right, the element size distribution in μm	68
Fig. 3.9. Temperature distribution of Model 3_e (solid matrix-polypropylene, fluid matrix-moist air) and distribution of element size, μm	68
Fig. 4.1. The heat and moisture exchange scheme in the active cooler system [145]	71
Fig. 4.2. The geometry and mesh of a ventilation model	72
Fig. 4.3. The boundary conditions and average operators of the ventilation model.	72
Fig. 4.4. Temperature distribution in case the ventilation rate is zero.....	74
Fig. 4.5. Temperature distribution in case the mass flow rate is $0.2 \text{ dm}^3/\text{min}$	74
Fig. 4.6. Temperature distribution in case the mass flow rate is $0.8 \text{ dm}^3/\text{min}$	75
Fig. 4.7. Temperature and time relation, considering different ventilation rates.....	75
Fig. 4.8. Numerical scheme, the mass flow rates of fluid (a) and heat fluxes (b) [16]	79
Fig. 4.9. Comparison of numerically predicted and experimental temperatures in 3D textile layer	79
Fig. 4.10. The absolute error between the experimental and numerical solution at 3D textile layer	79
Fig. 1. The 3D velocity field and mesh of the <i>Model 1_a</i>	122
Fig. 2. The 2D velocity distribution of the <i>Model 1_a</i> at a fixed height (z position)	123
Fig. 3. The average air flow, pressure, and residual of the <i>Model 1_a</i> at different height (z position).....	123

LIST OF TABLES

Table 1.1. Analytical models of permeability	31
Table 1.2. Parameter values of equations [81]	33
Table 1.3. Effective thermal conductivity models for two-phase materials [98]	37
Table 2.1. Set and measured construction parameters [8]	43
Table 2.2. Air domain and textile layer parameters.....	46
Table 2.3. Boundary conditions for the simulation of air permeability based on [125]	50
Table 2.4. R_{et} comfort rating system [132]	52
Table 2.5. Boundary conditions of R_{et} model	54
Table 2.6. Boundary conditions of R_{ct} model	56
Table 2.7. Thermal properties of solid matrix [137]	57
Table 3.1. Convergence study of <i>Model 1_c</i>	60
Table 3.2. Air permeability test results of <i>Model 1_a</i> when domain size is considered	61
Table 3.3. Numerical air permeability (AP) coefficients	62
Table 3.4. Numerical air permeability (AP) coefficients of two-layer structures	63
Table 3.5. Numerically predicted water-vapor resistance R_{et} coefficient	66
Table 3.6. Predicted and measured R_{ct} and K_{eff} [137]	66
Table 3.7. Numerically predicted R_{ct} and K_{eff} values of sample 21/15 (<i>Model 1_a</i>). 67	
Table 3.8. Numerically predicted R_{ct} and K_{eff} values of sample 29.3/15 (<i>Model 3_a</i>)	67
Table 3.9. Numerically predicted R_{ct} and h_{eff} of 3D textile.....	68
Table 4.1. Summary of boundary conditions used in the ventilation model	73
Table 4.2. Summary of predicted heat transfer coefficient	76

INTRODUCTION

The computer modeling of physical behavior of materials and structures has long been used in the development and design of new products in civil engineering, mechanical and mechatronics engineering, military industry, and many other technical fields. The numerical models of biomechanical and biomedical structures are used to analyze implant mechanics, develop protective workwear and lightweight armor for wear, plan some surgical and hyper-thermal treatment procedures, etc. Modern finite element computational technologies enable the representation of physical processes in a very realistic way. Often, the results of computer simulations are so adequate and reliable that they allow calculations to replace many field experiments. The total cost and time of computer modeling are almost always substantially lower than the cost and time of the experimental research. The computer resources that are required to model a particular structure become smaller if the model is constructed rationally. This means that the model must depict such details and features of the system that are important in its development and application and not delve into smaller and less significant things.

It is not always possible to give an unambiguous answer which numerical model should be used for a particular study. The same system under study can usually be represented by the models of different complexity and different capabilities of resolution of smaller-scale physical phenomena. The resolution of a model summarizes the fineness of the structural details or elements of its internal structure that are represented by the model, not considering the models that would be fundamentally wrong and misrepresent the very essence of physical behavior. However, the variety of fundamentally correct models of the same system is quite large. A successfully developed model often does not require particularly powerful computers to calculate it, but the information that is obtained is sufficient for the practical purposes.

The textile fabric structures are typical examples that need to be considered at different geometric scales. The thermal comfort of wearing depends on the ability of the fabric to transmit heat, air, and water vapor. At first glance, the textile fabric is a membrane that is characterized by certain physical properties of the heat and mass transfer. By using such an approach, the basic heat, air, and water vapor through the clothes can be more or less correctly modeled. However, the closeness of the calculation results to the reality depends very much on what properties will be given to the membrane elements of the fabric structure. Obviously, the properties of the finite element of the membrane, representing the fabric, are vastly different from, e.g., a sheet metal element, although mechanically and thermally both elements are membranes or shells. In order to determine the properties of an element, another problem has to be solved, i.e., how a small piece of tissue, the structure of which is known, “behaves” under certain conditions of loading. To this end, a model of a small fabric fragment is developed in micro-scale. This refined model may depict the weaving of threads, the internal volumetric structure of 3D textile, and many other case-dependent characteristics that are taking place in particular applications that are encountered in textile engineering. The threads, filaments, and 3D textile structures

are naturally depicted as volumetrically arranged structures of heat conductive rods, whereas the spaces between them represent the gas domain. By numerically experimenting with such a model, the overall properties of the macro-scale fabric element can be determined. When the internal structure is complex, the properties of the membrane element thus determined will be much closer to the reality than when describing them by the approximation with simplified analytical models. The model can be further improved. The assembly of components, comprising the 3D textile layer, as well may have their own internal structure. They are usually composed of thin filaments. Moving on to the next stage of resolution, the physical behavior of a single thread could be modeled by depicting it as a 3D solid body. The revised element can be used to model the 3D textile fabric element, and the adjusted 3D fabric element can be used to create a whole textile structural model. Such a sequence of models, providing the information about essentially the same physical process at different detail resolution scales, is referred to as a multi-scale approach. They comprise a class of heterogenic (i.e., structurally different) models of the same object.

In this work, starting with the micro-models of the smallest structure, the increasingly generalized finite elements were created until there was finally obtained a model of real construction of acceptable measurement, i.e., the one for which the computer resources required for the calculation are practically acceptable. Such a process is called model reduction or simplification, which can be performed in both single and multiple steps.

By examining the sequences of heterogeneous hierarchical models, high-adequacy-level models can be developed. During the history of scientific research, the models of different resolutions have always been used for the study of the behavior of any physical system. However, the choice of the macro-scale model is usually based on the general knowledge of the system under consideration and the researcher's scientific intuition. This thesis examines how models of different resolutions can be related by using mathematical methods. The practical need of such calculation is dictated by the necessity to find the effective heat transfer, effective thermal conductivity, thermal resistance, water-vapor resistance, water-vapor transmission, and air permeability coefficients, of modern textile materials in order to predict their functional properties at the macro-scale.

The aim and objectives of the work

The aim of the work is to develop and investigate the reduced models of finite element structures, representing the heat and mass exchange processes in 3D textile structures that are focused on predicting the air permeability, water-vapor resistance, thermal resistance coefficients, based on the results obtained by calculating the physical behavior of characteristic structural fragments, according to the higher resolution models.

In order, to achieve this aim, the following **objectives** were formulated:

1. To create a computational model of heat and moisture transfer through textile structures at the micro-scale. The outcomes of this computational model are physical parameters such as air permeability, water-vapor resistance, and thermal resistance coefficients.

2. To consider the convergence of numerical models.
3. To verify the developed numerical models in the macro-scale, to create a computational model, using a finite element approach of heat and moisture transfer at macro-scale. In this model, the equivalent material properties are used from micro-scale model simulation.
4. To compare the computational model efficiencies with the experimental measurements. The measurements of water-vapor resistance and thermal resistance were modeled following standard LST EN 31902/ISO 11092:2014(en). The measurement of air permeability was modeled according to the ISO 9237:1995 (E) standard.
5. To extend the computational models in order to evaluate the effective heat transfer coefficients of the 3D textile structures with active ventilation.

The object of the research

The object of the research is the physical process of heat, air, and water vapor exchange between the human skin and 3D textile structures. 3D textile is defined as a volumetric structure, consisting of two outer layers, which are joined by a spacer yarn or a spacer layer.

The methods of the research

The finite element method is applied in order to predict the thermo-comfort properties, such as, air permeability, water-vapor resistance, and thermal resistance coefficients of three-dimensional textile fabric. The steady-state and time-dependent analysis of the representative models was performed by the finite element solution of the heat and mass exchange partial differential equations, as well using general numerical methods for solving algebraic and ordinary differential equations. For the implementation of the created computational models, MATLAB and COMSOL MULTIPHYSICS 5.6 software has been employed.

Novelty and practical relevance

The paper proposes a new methodology for the construction of simplified heat and mass exchange finite element models based on the results of numerical analysis of the higher resolution models. The elements of novelty can be found by combining two models of different resolutions in a single structure. The computational analysis of modern textile materials provides a better understanding of heat and mass transfer processes that occur between human skin and environment. The novelty of this thesis is as well the extension of the methodology for obtaining the equivalent parameters, such as, air permeability, thermal resistance, water-vapor resistance, effective thermal conductivity, and effective heat transfer coefficients in micro and macro scales.

In the course of the work, specific reduced finite element models have been developed, which can be applied to the modeling of relevant and complex processes of heat and mass transfer through 3D textiles, saving computation time and maintaining the practically acceptable correspondence of models to reality. The developed algorithms and computational scripts in MATLAB and COMSOL

Multiphysics to determine the parameters of simplified models can be applied to the synthesis of other simplified heat and mass transfer models.

Statements for the defense

The proposed original approach to replace the high-resolution complex model of heat, air, and water vapor exchange in a 3D textile structure with a simplified model that retains its properties by identifying the parameters of the simplified model is defended. The qualification and skills of creating complex computational numerical models, using the advanced finite element analysis program COMSOL Multiphysics, have been acquired.

The approbation of research results

The main results of the dissertation were published in 4 scientific publications in the journals that are included in the list of scientific international databases, 2 publications were indexed in the Web of Science with Impact Factor, and 2 publications were indexed in the Web of Science without Impact Factor. The findings were presented at 4 international conferences as well.

The layout of the thesis

The dissertation consists of an introductory section where the problem is stated, 4 main sections, conclusions, a list of references, a list of the author's publications, summary, and 1 appendix. The total volume of the dissertation is 123 pages, including 41 figures, 21 tables, and 145 references.

Section 1 presents the literature review of textile structures and thermal comfort properties. It covers the concept of multiscale modeling as well as applications of finite element analysis in heat and mass transfer through textile. Section 2 focuses on the methodology of evaluation of air permeability coefficient, water-vapor resistance coefficient, thermal resistance coefficient. Section 3 includes numerical simulation results and the analysis of air permeability coefficient, water-vapor resistance coefficient, and thermal resistance coefficient. Furthermore, a convergence study of numerical models is presented. Section 4 demonstrates the application of numerical models that allows predicting effective heat transfer coefficients of fabrics under active ventilation.

1. LITERATURE REVIEW

The most advanced textile is widely used in aerospace, automotive, military, medical, human body, and engineering structure protection, sport and leisure clothing as well as many other applications [1]. For instance, in the industry, technical textile is used as filters, abrasive, drive and conveyor belts; in packing, as twine and cordage, sacks, bags, tarpaulins; in construction, as insulation and roofing material. The technical textile in aerospace can be used in specialized clothing (proof jackets, adaptable uniforms); in the automotive industry, as car lining, airbags, fireproof seat covers; in the military and public services, as bulletproof jackets; in medical and healthcare, as bandages [2]. In the practice of orthotics and prosthetics, the materials

such as leather, metal, wood, plastics, composites, and viscoelastic polymer are commonly used in rehabilitation treatment [3].

In the development phase (manufacturing process) of textile composites, there are typically four significant levels: Fiber→ Yarn→ Fabric→ Composite, that are depicted in Fig. 1.1. The manufacturing process can be carried out by using various methods of liquid moldings, such as resin transfer molding (RTM), injection molding [4]. In the RTM process, the employed fiber preform is typically made up of woven fiber bundles. Each of the fiber bundles is called a tow, fiber, or yarn, and each of the yarns, in turn, contains many fibrils or filaments. A set of yarns involves a structure known as a fabric, cloth [5].

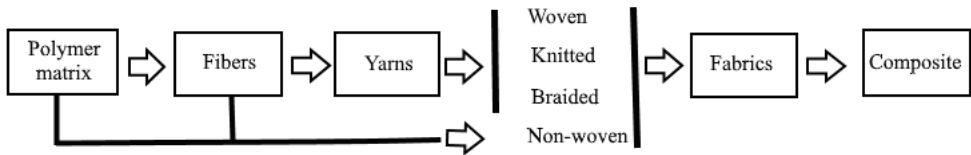


Fig. 1.1. Levels of manufacturing process of textile composites

Textile preforms can be classified on the basis of different criteria, including the degree of reinforcement in the thickness direction (e.g., two- and three-dimensional), the number of fiber orientation (e.g., monoaxial, biaxial), and the method of manufacture (e.g., woven, non-woven, braided, knitted) [6], [7]. The classification of three-dimensional textile preforms is shown in Fig. 1.2. The samples of three-dimensional textile that are made from polypropylene and polyester (PES) are depicted on the right.

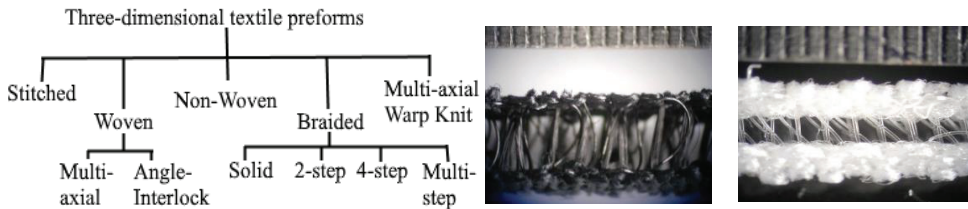


Fig. 1.2. Classification of three-dimensional textile preforms [7]; samples of 3D textile made from polypropylene and polyester

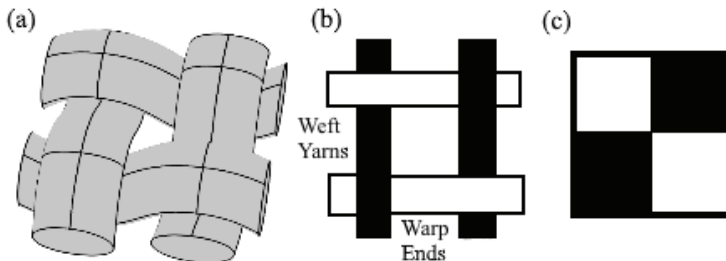


Fig. 1.3. A unit cell of woven fabrics shown three-dimensionally (a), a flat pattern view (b), and a schematic of plain weave pattern (c) [8]

Depending on the form of weaving pattern, the woven fabrics might be divided into three main categories: plain, twill, satin (see Fig. 1.4.). The schematic of one-layer woven fabrics when the plain weave pattern is used is shown in Fig. 1.3. The vertical yarns are called warp yarns, and the horizontal yarns are called weft yarns. Normally, the weave patterns are represented by weaving (squared) paper where each column represents one warp yarn and each row represents weft yarn. On the weaving paper (see in Fig. 1.3. c)), when the warp yarn is above the weft yarn, the square is portrayed in black color [8], [9]. In order, to produce new fabrics, warp and weft raw materials (polymer level, composing fiber), warp and weft linear density (thread level), warp and weft settings, and fabric weave (fabric level) are evaluated [10].

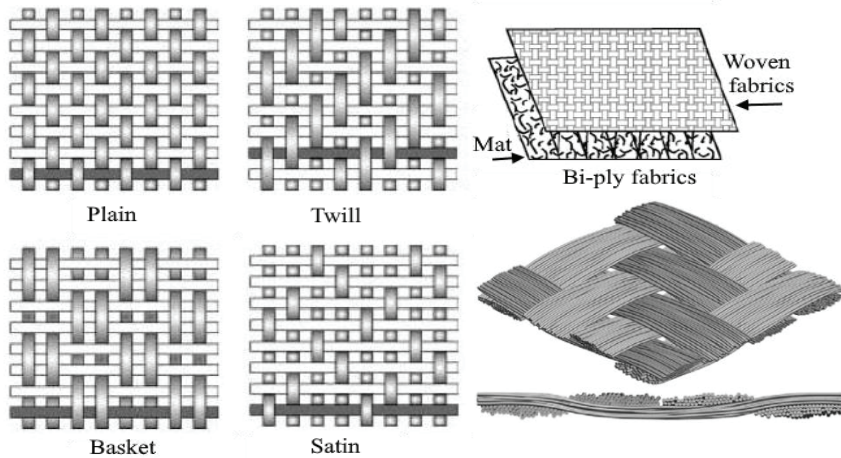


Fig. 1.4. Various weave styles for woven fabrics: plain, twill 2/1, 2 x 2 basket, crowfoot satin [11]; illustration of bi-ply fabrics [11] and a multi-chain unit cell of 2/2 twill weave [12]

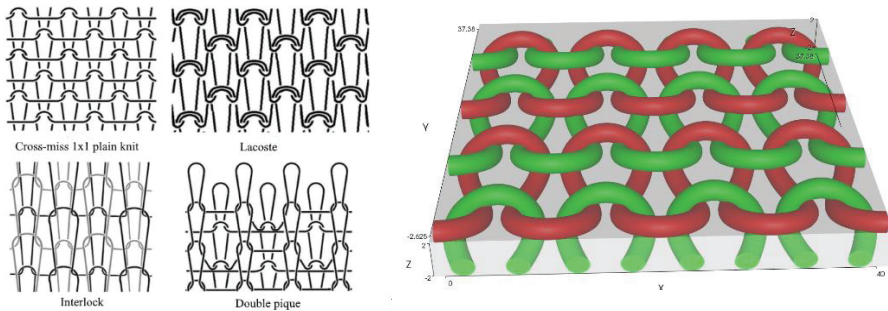


Fig. 1.5. Knitted fabric structures: cross-miss 1 x 1 plain knit, lacoste, interlock, and double pique [13], and weft-knit fabric [14]

The most common types of fabrics are woven, knitted, and non-woven (non-crimp). Woven fabrics are used primarily for suits, shirts, and other garments that do

not require highly elastic properties, whereas the knitted fabrics are used primarily for underwear, sweaters, t-shirts, and other garments that must be able to shrink and stretch [9]. Non-woven fabrics are created without the use of a weaving process, and their raw materials, loose fibers, are transformed into fabrics through chemical, mechanical, or thermal processes that can link the fibers together [9]. Non-woven fabrics can be used in personal care and hygiene (like baby diapers, cosmetic wipes), clothing (like an insulating material for protective wear, firefighting outfits, safety helmets, or industrial shoes), household (vacuum cleaner bags, washing machine bags, food envelopes, etc.), upholstery (furniture, curtains, carpet backing, etc.), etc. [9]. Fig. 1.4. and Fig. 1.5. present various structures of fabric. Fig. 1.4. depicts a bi-ply fabric that is formed by stitching two fabrics together. A chopped strand mat is made from continuous fibers or random cut fibers [11].

Different types of properties can be used to indicate the performance of textile materials, for example, the mechanical properties, such as uniaxial or biaxial tensile properties, compression, shearing properties, and identify the material's resistance to the external force's activities that cause deformations to the material. Thermal and water transport properties, such as air permeability, water-vapor transmission rate, thermal resistance, and physical properties, like yarn diameter, thickness, porosity, structural density, and internal and external factors, as well as fabric and human interactions, can all have an impact on the fabric performance. For instance, the air gap between the human skin and clothes is defined as a 'microclimate' [2]. It might have an impact on the heat and mass transfer from or to the body (e.g., protective clothing, where microclimates are normally thicker, natural convection might take place) [15].

The most important requirement for clothing designers or engineers is to provide thermo-physiological comfort between human skin and fabric. However, theoretical and numerical investigations of the physical behavior of advanced textiles are quite complicated due to the complex internal structure, simultaneously heat and moisture transfer, and other physical processes, which occur in different space and time scales [16].

1.1. The overview of thermal comfort properties of fabrics

The clothing and textile products that are utilized daily are crucial materials for achieving physiological and psychological comfort. The main function of clothing is to protect the body from hazardous environmental conditions [17]. This protection performs several functions, i.e., to preserve right thermal environment for the body and avoid body injury due to abrasion, radiation, wind, chemical substances, etc. [17]. Thermal comfort is a complex term that describes thermo-physiological comfort (as well known as thermal-moisture comfort), in which "thermal balance" is achieved when heat loss is equal to heat production [18]. As a result, the body maintains constant temperature. The most common thermal comfort properties of textile are water-vapor resistance (breathability), thermal resistance, air permeability, liquid wicking rate, water resistance (under hydrostatic pressure), water repellency [18]. Following Saldaeva [19], Umair et al. [20] two main material parameters for characterizing clothing comfort are air permeability and thermal conductivity.

According to the ISO 9237:1995 (E) [21] standard, **air permeability** is defined as the velocity of air flow, passing perpendicularly through the test specimen, under specified conditions of the test area, pressure drop, and time. Air permeability measurements can be performed with the air permeability tester [21]. Air permeability coefficient R mm/s can be experimentally calculated from Eq. 1, where \hat{q} – mean air flow rate dm³/min, A – surface (test) area cm², 167 – conversion coefficient from dm³/min to mm/s [21].

$$R = \frac{\hat{q}}{A} 167. \quad (1)$$

The water-vapor resistance of textile and **the thermal resistance** of textile can be measured by using the Sweating Guarded Hot Plate M259B method known as “Skin Model”. It imitates the heat transfer process between human skin and textiles [18]. Following ISO 11092:2014, **the water-vapor resistance** is a quantity that is specific to textile materials or composites, which determines the “latent” evaporative heat flux across the given area in response to the steady applied water-vapor pressure gradient [22]. The measurement of water-vapor resistance of textile requires that the temperature of measuring and air temperature in the test enclosure is set to 35 °C with a relative humidity of 40 %. The air speed is hold at 1 m/s. Due to these isothermal conditions, the water vapor condensation in the test specimen is prevented [22]. The coefficient of water-vapor resistance can be calculated from Eq. 2.

$$R_{et} = \frac{(p_{sat} - p_v)A}{H - \Delta H_c} - R_{et0}; \quad (2)$$

where p_v – water-vapor partial pressure Pa, p_{sat} – saturation water-vapor partial pressure Pa, A – the area of measuring unit m², H – heating power W required to maintain the plate temperature at $T = 35$ °C, ΔH_c – correction term for heating power, R_{et0} – the apparatus constant m²·Pa/W for the measurement of water-vapor resistance R_{et} without the sample, according to ISO 11092:2014 [22].

The thermal resistance of textile is the temperature difference between the two faces of a material (T_m and T_a), divided by the resultant heat flux H per unit area A in the direction of the gradient [18]. The measurement of thermal resistance of textile requires that the temperature of the measuring unit is 35 °C; the ambient air temperature is 20 °C. The automatically relative humidity is 65% [22].

$$R_{ct} = \frac{(T_m - T_a)A}{H - \Delta H_c} - R_{ct0}; \quad (3)$$

where T_m – mean temperature of the measuring unit K, T_a – air temperature in the test enclosure K, H – heating power W required to maintain the plate temperature at $T = 35$ °C, ΔH_c – correction term for heating power, R_{ct0} – the apparatus constant m²·K/W for the measurement of thermal resistance without sample [22].

The thermal resistance in textiles might consist of one or more conductive, convective, and radiant components [18]. **Thermal conductivity** λ W/(m·K) defines the transport of energy, in the form of heat, through a body of mass as a result of a

temperature gradient (see Eq. 4) [18].

$$\lambda = \frac{(H - \Delta H_c)L}{(T_t - T_0)A} - \lambda_0 = \frac{L}{R_{ct}}; \quad (4)$$

where $(H - \Delta H_c)$ means the net heat flux going through a material of thickness L , and λ_0 is the apparatus constant. The temperature rises from the initial time (T_0) to the test time (T_t), which is measured as a response to the steady applied power (heat flux) [18].

The heat transfer between the skin and textile structures is related to the change of temperature. In case, when the skin temperature is higher than the textile, the heat will flow from skin to the textile. In addition, the person will observe a feeling of coolness. This phenomenon is called a warm-cool feeling of the fabric [23].

Thermal absorptivity b $\text{W}\cdot\text{s}^{0.5}\text{m}^{-2}\text{K}^{-1}$ describes a warm-cool feeling of the fabric. It can be obtained from the equation as follows:

$$b = \sqrt{\lambda\rho C}. \quad (5)$$

The thermal absorptivity values of different textile materials can vary from 20 to $900 \text{ W}\cdot\text{s}^{0.5}\text{m}^{-2}\text{K}^{-1}$ [24], [23]. The case of a fabric with a higher value of thermal absorptivity indicates that there will be a cool feeling within a short time while touching the fabric. For example, dry cotton fabrics have the lowest value, and extremely wet cotton fabrics have the values above $900 \text{ W}\cdot\text{s}^{0.5}\text{m}^{-2}\text{K}^{-1}$ [23].

According to ISO 11092:2014, **water-vapor permeability index** i_{mt} is a dimensionless variable with values ranging from 0 to 1. A value of 0 indicates that the material is water-vapor impermeable. The material has infinite water-vapor resistance. A value of 1 indicates that the material has both thermal resistance and water-vapor resistance of the air layer of the same thickness [22]. The i_{mt} is expressed in Eq. 6, where S is equal to 60 Pa/K .

$$i_{mt} = S \frac{R_{ct}}{R_{et}}. \quad (6)$$

Water-vapor permeability W_d $\left(\frac{\text{g}}{\text{m}^2\text{hPa}}\right)$ is characteristic of a textile material or composite, based on the water-vapor resistance and temperature, following Eq. 7:

$$W_d = \frac{1}{R_{et} \cdot \phi_{T_m}}; \quad (7)$$

where Φ_{T_m} is the latent heat of vaporization of water at the temperature T_m of the measuring unit equals, for example, 0.672 Wh/g at $T_m = 35 \text{ }^\circ\text{C}$, following ISO 11092:2014 [22].

1.2. The concept of multiscale modeling

The physical model of a complex system usually consists of complicated internal structures, large amounts of components (scales), and coupled physical processes. Solution finding, using traditional approaches (focus on one particular scale), usually are not efficient, considering computational time, accuracy level, and a variety of assumptions [25], [26]. The extension of traditional methods is multiscale modeling. A multiscale model is a mathematical model, which considers models simultaneously at different length and time scales in order to portray the phenomena of a complex system [25]. Common modeling methods that depict each continuum scale are shown in Fig. 1.6. [27].

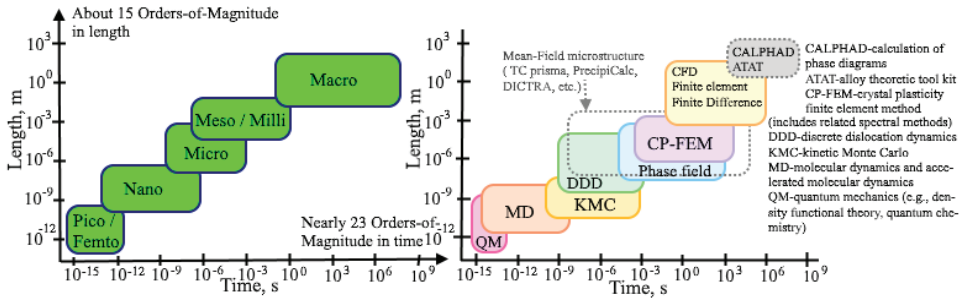


Fig. 1.6. A scheme of multiscale modeling and common modeling techniques [27]

The dashed border boxes display methods for equilibrium conditions (mean-field methods) that provide equilibrium information or average behavior. Finite element, finite difference, and computational fluid dynamics methods are primarily macroscopic continuum methods, although they have many niche applications at other scales [27].

Currently, the strategy of multiscale modeling consists of two main steps. The first one is to develop single-scale methods, and the second is to try to transfer parameters (information) between scales [27]. The number of continuum (length) scales depends on the complexity of the system (nature). According to literature, about five or six length scales can be physically separated [28]. The transfer of information between different scales can be done by using classical techniques: bottom-up (i.e., from small scales to larger scales), top-down, concurrent, and middle-out [25]. However, one of the biggest challenges is to perceive relations between different scale models, for instance, computing transport coefficients that are required in continuum models from molecular dynamics models [26].

Multiscale modeling can be applied to solve complex problems in different scientific disciplines (chemistry, physics, biology, mechanics, and materials engineering), for example, in structural biology, to acquire knowledge into viral structure and dynamics [29], in engineering, for the simulation of optoelectronic, electronic devices [30]; moreover, the mechanical behavior of unidirectional composite textile [31], the heat and moisture transfer in the thermal smart clothing system [32], designing optimally-graded depth filter [33]. To sum up, multiscale modeling allows to reduce computational resources, achieve higher levels of detail,

and improve accuracy. Three length scales might be taken into account for textile structures. According to Saldaeva [19], the microscopic scale is concerned with individual fibers in a yarn, their geometric parameters, such as diameter and shape, and their arrangement within the yarn [19]. The meso scale deals with the behavior of the unit cells. It takes into account the geometric parameters of the yarns, such as width, length, and height, as well as the geometry of gaps between the yarns and their interlacing pattern. Finally, the macroscopic level scale indicates a textile sheet or the garment that has deformed due to the body shape or application [19]. In accordance with Aihua et al. [32] the thermal processes in the multiscale clothing wearing system occur at different scales due to the different dimensions of the entities. The difference between the scales is 1000 times greater [32]. For instance, the heat storage process of PCM particles is in the nanometers; fiber moisture sorption/desorption is in the micrometers; fabric heat and moisture transfer are in the millimeters, and human body thermal regulation is in the meters [32]. Under Stier et al. [34] the investigation of the structural behavior of the ankle-foot orthosis, which consists of multiple layers of the thermoset matrix, reinforced with carbon fibers, a hierarchical multi-scale modeling strategy was used [34]. A two-scale model was proposed for unidirectional CFRP (carbon fiber reinforced composites), which includes the scale transition from the micro- to the macro-scale. Besides, for textile CFRP, a three-scale method was used to achieve scale transitions from micro- to meso-scale and from meso- to macro-scale [34]. The scale transitions are depicted in Fig. 1.7.

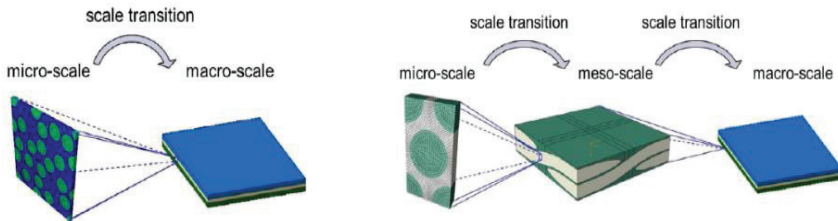


Fig. 1.7. Illustration of hierarchical multi-scale modeling strategies [34]

1.3. The applications of finite element analysis in heat and mass transfer through textile

The finite element method is a modern computational technique in engineering analysis. The advanced use of finite elements began in structural engineering [35]. The first publications can be attributed to the authors A. Hrennikoff [36] and D. McHenry [37] who developed lattice analogies between the actual discrete elements, for instance, bars and beams, and the corresponding portions of a continuous solid. This developed analogy could be used in rectangular areas. R. Courant [38] provided a solution to the problem of torsion with piecewise linear approximations over the triangular mesh. These methods belonged to semi-analytic techniques, which were used for aircraft structural design in the early 1940s [39]. However, the calculation process was limited and time-consuming. M. J. Turner et al. [40] provided a method for calculating stiffness influence coefficients of complex shell-type structures. The

researchers have presented the element stiffness matrix, based on the displacement assumptions, for a triangular element together with the method of direct stiffness calculation for assembling the elements [39]. The first use of the term ‘finite element’ has been coined by R. W. Clough [41] in a published paper, describing the elasticity of the plane in continuous structures.

During the 1950s and 1960s, four academics: J. H. Argyris, R. W. Clough [41], H. C. Martin [42], and O. C. Zienkiewicz, had an important influence on the development of finite element technology and its applications beyond the aerospace industry to various engineering problems [43]. In a book section, J. H. Argyris and his research group [44] summarized the matrix forced method, established the stiffness of triangular elements as used by them since 1956, extended the matrix displacement theory in non-linear problems. J. H. Argyris and R. Kačianauskas [45] presented semi-analytical finite elements, leading to the development of higher-order theory for beams [45]. O. C. Zienkiewicz et al. [46] are the authors of the first book of *The Finite Element Method*, which reached seven editions in total [47]. Moreover, O.C. Zienkiewicz et al. were interested in heat and fluid flow problems [48], [49]. The field problems were solved in the context of torsion, heat transfer, electrical fields, anisotropic seepage problems [47].

The general-purpose computer programs for FEA (finite element analysis) were developed at the end of the 1960s and the beginning of the 1970s. The computer graphics have been included in the Finite Element software, which has made FEA more appealing for design purposes [43]. Nowadays, a lot of FEM-based software like NASTRAN (known as NASA Structural Analysis, founded in 1965), ANSYS (founded in 1970), COMSOL Multiphysics (formerly known as FEMLAB (the first version released 1998) founded in 1986), and others are available. The applicability of finite element analysis to heat and mass transfer problems has been reported in a significant amount of publications. The developed numerical models were useful to identify and characterize the effect of various parameters such as physical and thermo-physical properties of fabrics, air gap, and moisture [50].

The solution steps of the continuum problem (e.g., heat transfer problem), using the finite element method, are depicted in Fig. 1.8. The main steps of the finite element procedure are to discretize the continuum, select interpolation or shape functions, form element equations (formulation), assemble the element equations to obtain a system of simultaneous equations, solve the system of equations, and calculate the secondary quantities [51].

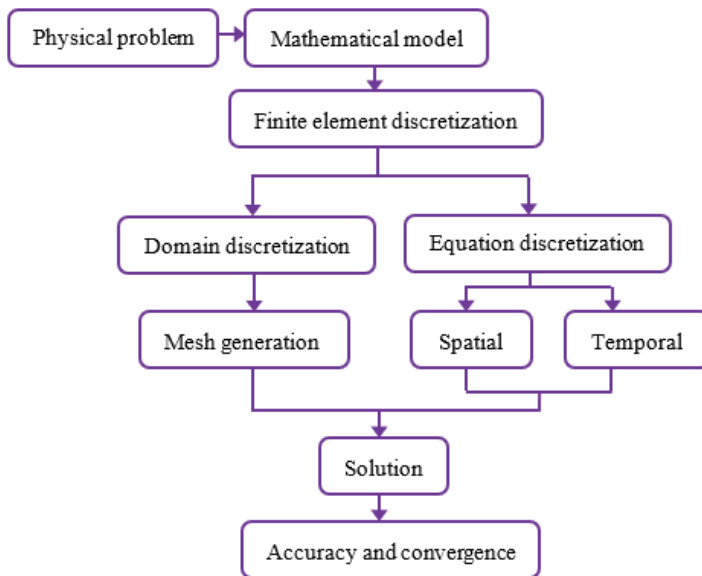


Fig. 1.8. The main steps of FEM [51]

In recent decades, various aspects of textile behavior were presented. Cimilli et al. [52] created a FEM model to simulate the heat transfer of plain weft-knitted cotton fabrics. The proposed model evaluates the effective heat conduction coefficients of socks. The geometry of the fabric was generated by using CATIA V5R16 software, then imported into the ANSYS Workbench software for the finite element analysis [52]. The model had some simplifications: yarns were considered as homogeneous elastic rods, the fabric was formed of planar loop structures with identical configuration, and the plastic deformation (that occurs in the yarn when the fibers make contact with each other) was neglected [52]. This model was designed, according to the actual experiment setup (ISO 8302); thus, the virtual model was finalized by adding three plates of steel, where the outer two plates indicate the cold plates ($T = 23.88\text{ }^{\circ}\text{C}$) and the middle plate indicates the hot plate ($T = 36.59\text{ }^{\circ}\text{C}$) [52]. A good agreement was found between the FEM outcomes and the experimental data that demonstrated the applicability of FEA. Santos et al. [15] investigated the fluid flow and heat transfer across cylindrical clothing microclimates. The Model's geometry consisted of a 2D horizontal impermeable cylinder (limb), surrounded at a varying distance by a layer of porous material (fabric) with a constant diameter that is surrounded by the external air [15]. The performed simulations took into account forced convection, natural convection, and radiation. The incompressible Navier–Stokes equations of continuity, momentum, and energy equation were combined and solved, using the FEM approach. The researchers have analyzed the impact of different values of the microclimate thickness ratio [15]. A numerical simulation of the heat transfer in the direction of thickness of single woven layers, based on the jet system theory, was presented by Angelova et al. [53]. The geometry of the threads

and the pores in the woven textile layer (macrostructure) was approximated into a virtual 3 x 3 in-corridor ordered jet system. The simulations were based on the Reynolds-averaged Navier–Stokes partial differential equations (RANS) and the energy equation (in order to simulate the heat transfer). In order to close the system of partial differential equations, two turbulence models were tested: $k-\epsilon$ and Reynolds Stress Model (RSM) [53]. The numerical results demonstrated that there was no significant difference between the temperature field, the heat rate, and the thermal resistance of the samples, using different turbulence models. The mathematical model was performed by using the control volume discretization method. SIMPLE algorithm and second-order upwind difference scheme were applied to solve the system of algebraic equations. The simulations were done by using FLUENT 6.3 CFD software [53].

There was a lot of attention paid to the investigations of the multi-layer textile packages. Barauskas et al. [16] developed a 1D finite element model for heat and water-vapor exchange through multilayer textile packages with a three-dimensional spacer fabric ventilation layer on a macro-scale. Two schemes with and without ventilation layer were proposed of flow rate and heat balance equations through the 3D textile. The computational model considered air and water-vapor flow rates and heat fluxes through all layers of the multi-layer textile package [16]. Puzkarz et al. [54] investigated the heat transfer through 3D weft-knitted polypropylene fabric. 3D model geometry was designed, according to the scanning electron microscope (SEM) images of polypropylene knitted fabric, which were imported into SolidWorks software. The fabric was depicted as a monolayer that is made of solid monofilaments and fluid (air) in the void spaces. One of the goals of the study was to analyze the thermal behavior of the fabric by using a different number of layers. The heat transport was done by using SolidWorks software (tool based on FEA) that allowed to take into account the heat conduction in a solid material, convection, radiation, gravitational effects, laminar and turbulent fluid flow within the void spaces [54]. In a research article [55], numerically and experimentally transient heat transfer through the multilayer textile assembly induced by radiation was investigated. The virtual model consisted of the heat radiation source (rectangular plate), air domain, and sample from five layers: woven fabric (outer shell), membrane (moisture barrier), two nonwoven fabrics, inner woven fabric (lining). Porosity, woven fabric thickness, the distance between the weft yarns, the distance between the warp yarns, the elliptic shape of the yarn cross-section of layers were determined from the SEM images by using Image J software application. Nonwoven fabrics, membrane, and yarn in both woven fabrics due to the complex internal geometry were mapped as homogenized 3D objects with physical parameters (density, specific heat, thermal conductivity coefficient) [55]. The simulation was carried out on energy conservation and Navier–Stokes equations. The Solidworks Flow Simulation package allowed to simulate thermal radiation based on the so-called discrete transfer model. Numerically and experimentally, the thermal protection properties (transmitted heat flux density, heat transmission factor, radiant heat transfer index) were calculated. The relative differences between the experimental and simulated parameters were 3–20 % [55]. The simulations of heat

transfer through multi-layer protective clothing exposed to flame were investigated by Puszkarz and Machnowski [56]. The proposed numerical models allowed to determine the time dependence of temperature of the outer layer of the two assemblies models for two intensity levels of the heat flux ($45 \text{ kW}\cdot\text{m}^{-2}$ and $58 \text{ kW}\cdot\text{m}^{-2}$). Moreover, the heat transfer index and the heat transmission factor were predicted. The models assumed the simplification of the geometry and the internal structure of the individual layers [56].

The amount of studies has been undertaken in recent years to investigate the phase change materials (PCM). Barauskas et al. [57] developed the finite element models to predict transient heat exchange through fabrics, which surface is coated with stearic acid butyl ester butyl stearate (BS). The PCM can be utilized as a core material for the development of microcapsules that are intended to be applied for thermo-regulative textiles [57]. The equations of heat transfer can be expressed as follows:

$$\mathbf{C}\dot{\mathbf{T}}(t) + \mathbf{K}\mathbf{T}(t) = \mathbf{Q}(t); \quad (8)$$

where \mathbf{C} – structural heat capacity matrix, \mathbf{K} – structural heat conduction matrix, $\mathbf{T}(t)$ – nodal temperature vector, $\mathbf{Q}(t)$ – nodal heat power vector due to the external heat sources [57]. The finite element model is nonlinear due to the specific heat capacity of PCM dependence on temperature in melting and solidification phases [57]. The specific heat capacity of the material curves at temperature change rate was obtained experimentally and directly taken into the finite element heat capacity matrix. The experimental measurements were done by using differential scanning calorimetry (DSC). The study allowed verifying the suitability of samples for heat capacity against temperature (HCT) relationships measurements in terms of sample size and the temperature change rate. It plays an important role in the investigation of effective HCT relationships in composite fabrics with PCM [57]. Furthermore, there was developed a finite element model of thermal behavior of a PCM-coated spacer fabric, subjected to the infrared irradiation. The model allowed to simulate the thermal response of the fabric in the case of multi-cycle infrared heating-cooling [57].

The heat transfer behavior of woven fabric constructed from yarn, incorporated with microencapsulated phase change materials (MicroPCM), was analyzed by Iqbal et al. [58]. This study contains two parts: the recreation of realistic geometry and the heat transfer analysis. The geometry of a unit cell of woven fabric was created with TexGen software, then exported into ABAQUS software for the FEA. The three-dimensional model consisted of air domain, yarns (polypropylene), capsules (melamine-formaldehyde), and phase change material (n-octadecane). The effect of radiation and convection was neglected. The computational model allowed predicting the heat fluxes values, study time-dependent thermo-regulating effect with different amounts of PCM in fabric. This model is valid only for plain weave structures [58]. The finite element models to determine the effective thermal conductivity of MicroPCMs coated composite fabrics were proposed by Siddiqui and Sun [59]. The main stages of modeling were to create and analyze the unit cell models of MicroPCMs and binder, uncoated fabric, fabric with coated material. Then, the

separate unit cell models were combined into a fabric composite model. The simulation of temperature distribution was done by using ABAQUS software [59]. The effective thermal conductivity was calculated by the following equation:

$$K_{eff} = Q_z \cdot \frac{t}{\Delta T_z}; \quad (9)$$

where Q_z – the overall heat flux value, ΔT_z – the temperature difference in the z-direction (fabric thickness direction), t – thickness of the fabric [59]. A detailed description of the calculation of Q_z can be found in their previous work [60]. In the proposed models, in order to determine the thermal conductivity and thermal resistance, the researchers evaluated the actual cross-section of yarn, fiber orientation, and non-homogeneous behavior of fibers [60], [59]. Phelps and Sidhu [61] developed a mathematical model of heat transport through incorporated PCM into the fabric of the fire-fighting suit in conjunction with air gaps. The one-dimensional model considers the heat transfer through different configurations of the fire-fighting suit (see Fig. 1.9.). The moisture transport was neglected in the proposed simulation [61].

Clothing				Skin				
	Outer 0.7 mm	Thermal Inner 2 mm		Air Gap 5 mm	Epi- dermis	Dermis	Subcutaneous	Case A
Outer 0.7 mm	Thermal Inner 1 mm	Air Gap 1 mm	Thermal Inner 1 mm	Air Gap 5 mm	Epi- dermis	Dermis	Subcutaneous	Case B
	Outer 0.7 mm	PCM 1 mm	Thermal Inner	Air Gap 5 mm	Epi- dermis	Dermis	Subcutaneous	Case C
Outer 0.7 mm	PCM 1 mm	Air Gap 1 mm	Thermal Inner 1 mm	Air Gap 5 mm	Epi- dermis	Dermis	Subcutaneous	Case D

Fig. 1.9. A principle scheme of four different configurations of layers of suit and skin, simulated by the model [61]

In a one-dimensional model, the governing equations read as follows:

$$\rho C \frac{\partial T}{\partial t} = \frac{\partial}{\partial x} \left(\lambda \frac{\partial T}{\partial x} \right) - G_{\rho_b} C_b (T - T_c) - \rho Q \frac{\partial}{\partial t} (Z), \quad (10)$$

$$Z = 0.5 \times \operatorname{erfc} \left(\frac{T - T_{melt}}{T_{range}} \right); \quad (11)$$

where t – time (s), x – a spatial variable through the skin and clothing layers (m), G – blood perfusion rate ($\text{m}^3 \cdot \text{s}^{-1} \cdot \text{m}^{-3}$), Q – the heat of fusion of the PCM ($\text{J} \cdot \text{kg}^{-1}$), subscripts b and c refer to blood and core body temperatures, respectively [61]. Z has a value between 0 and 1 and indicates the proportion of PCM that is solid at any given time, T_{melt} – melting temperature of the PCM ($^{\circ}\text{C}$), and T_{range} – temperature range when the PCM melts over ($^{\circ}\text{C}$). The parameters k , C , G , Q , and ρ vary from one layer to the next, which is allowed within the model [61]. The conservation of energy equations was solved for all four cases of the fire-fighting suit, using a finite element package FLEXPDE™. The numerical simulations allow to examine the effectiveness of the suit configurations with the PCM and additional air layer in order to prevent the

firefighter from suffering burns. The numerical results have shown that the addition of an air gap with a width of just 1 mm beneath the PCM layer increases the thermal protection provided by the suit [61]. Fonseca et al. [62] proposed guidelines for specifying a PCM layer in firefighter protective clothing ensembles [62]. The mathematical model evaluates the situation in the protective clothing–skin system that there is no microclimate layer between the garment inner layer and the skin. The geometry of the suit consists of an outer layer, a PCM layer, a thermal inner layer, and skin layers, containing epidermis, dermis, subcutaneous. In order to initiate the flash fire conditions, three different heat flux values were used as a boundary condition in a 1D model to describe high-, medium-, and low- intensity heat exposures. The phase change in the PCM layer was modeled by using the apparent heat capacity approach. The energy equation in the PCM domain reads as follows:

$$\rho C_{app} \frac{\partial T}{\partial t} = \nabla \cdot (\lambda \nabla T); \quad (12)$$

where C_{app} is apparent specific heat in J/(kg·K) [62]. The apparent specific heat curve was measured with DSC. The experimental curve was approximated by a function via minimizing square technique. In all cases of simulation, this function was used and adapted. The C_{app} function in Eq. 13 can be defined as follows:

$$C_{app} = \frac{dH}{dT} = \lambda_* \times \frac{\exp\left(-\frac{T-T_m}{T_0}\right)^2}{T_0 \sqrt{\pi}} + C_{PCM}; \quad (13)$$

where H – the total enthalpy in J/kg, T_m – the melting temperature in K, λ_* – the latent heat in J/kg, and C_{PCM} denotes the specific heat in J/kg/K [62]. The variable T_0 is the floating variable that is used to fit the experimental curve [62]. Numerical simulations were done by using a FEM platform. A numerical study allows to explore the effect of PCM latent heat, mass, melting temperature, and position within the garment ensemble, assess the implications in terms of thermal performance and time to second-degree burns, under high-, medium-, and low-intensity heat exposures [62].

The numerical analysis of heat transfer that occurs by convection through nonwoven fabrics with and without hydrophobic amorphous silica aerogel was investigated by Venkataraman et al. [63]. The stationary thermal analysis was carried out with Ansys and Comsol Multiphysics software. For Ansys simulation, a unit cell model was created of highly random individual polyester and polyethylene fibers of nonwovens that were assembled to one realistic fabric structure. The fibers occupy 26.27 % of the space inside the unit cell. In order to assess the impact of aerogel to heat loss, two simulations were investigated. In the first configuration, the unit cell model consists of fibers and stagnant air, and in the second configuration, the stagnant air is changed into the aerogel. It has been found that the heat retention in nonwoven fabric with aerogel was higher than the nonwoven fabric without aerogel [63]. Comsol Multiphysics software was used to simulate and analyze four configurations: fabric with aerogel and with forced convection (2.5 m/s wind at the outer surface); fabric with aerogel and without forced convection, fabric without aerogel and with forced

convection (2.5 m/s wind at the outer surface), and fabric without aerogel and without forced convection [63]. The conjugate heat transfer module was applied to couple the heat transfer module and the fluid flow module. In the proposed model, the laminar and compressible flow regime was assumed. The numerical simulations demonstrated that the aerogel improves the thermal insulation of the fabric [63].

In the works [64], [65], there was developed a 3D model to simulate the reactive transport within a light photocatalytic textile, used to decontaminate industrial effluents. The photocatalytic textile consists of fabric and optical fibers. The geometry domain in micro-scale represents a RVE of the photocatalytic textile with periodic boundary conditions. There were coupled fluid flow governing equations, species convection-diffusion equations, and a heterogeneous reaction equation in the model. The numerical simulation was performed by using Comsol Multiphysics software [65].

The finite element analysis helps to analyze various aspects of heat and mass transfer through the fabric. Numerous researches analyze the heat transfer through textile fabrics that includes the conduction heat transfer through solid yarn and air space between yarns, natural convection through a gap between yarns and radiation through yarns, and a gap between yarns [50]. There have been developed numerical models that consider the basic structure of fabrics and determine effective thermal conductivity or thermal resistance. The thermal protective performance of fabric was investigated, neglecting the moisture transfer effects; some studies considered the surface to surface radiation in the air gap. A great deal focused on the heat transfer through the multi-layer arrangement of the fabric assembly, containing PCM in between the fabric layers. The coupled analyses of heat and moisture transfer through fabric allowed to analyze the condensation, wicking, absorption, phase change, radiation attenuation, and other phenomena [50]. Various factors, affecting thermal protective performance, were studied, including the effect of fabric physical/structural properties, the effect of thermo-physical properties of the fabric, the effect of the air gap width, the effect of moisture, the effect of PCM, and the effect of aerogel [50].

1.4. Permeability prediction using analytical and numerical models

The air permeability coefficient (AP) and water-vapor permeability coefficient are essential properties of textile structures that significantly contribute to the physiological comfort felt by a dressed person [66]. These properties as well influence the performance of technical/advanced textiles, particularly in the use of protective products, including airbags, parachutes, and tents [67]. The experimental measurements or theoretical investigations to determine the AP are crucial, as it defines the properties of keeping warm, windproof, and breathability [68]. The AP and water vapor permeability coefficients are mainly affected by the porous structure characteristics of textile materials. The air permeability (AP) coefficient of textile materials is generally understood as the ability of the air-permeable fabric to transmit air under the given well-defined conditions [66]. The permeability can be evaluated by using empirical methods, analytical models, and numerical simulations [53], [69].

The earliest studies of porous material permeability were carried out by Henry Darcy in the middle of the 19th century. In 1856, in a report on the construction of the Dijon, France, municipal water system, the researcher published a relationship for the flow rate of water in the sand filters [70]. It has been found that the flow rate is directly proportional to the pressure drop causing the flow. This linear relation is known as Darcy's law (see Table 1.1.) [71], [70], [5]. According to [71], [72], the first studies of air permeability of fabrics were done by Rubner in 1896, which were based on Darcy's law. Darcy's law is a macroscopic law that does not describe the effect of microscopic properties, such as capillary, tortuosity, porosity. The local permeability is ultimately determined by these properties. Local permeability (\mathbf{K} , m^2) is the average cross-sectional area of a medium that allows fluid flow. Darcy's law is valid when the fluid is chemically inert, the porous medium's solid matrix is rigid and stationary, the flow is laminar, and Reynolds's number is in the range $0 < Re < 10$ [73].

The Reynolds number Re is defined as follows:

$$Re = \frac{\rho v d}{\mu}; \quad (14)$$

where v – the superficial velocity (m/s), i.e., the flow rate divided by the cross-sectional area of the cavity (m/s), d – fiber diameter (the hydraulic diameter of a pore (m)) [68]. Normally, the air velocity through the pores of the (knitted) fabric does not have a high value, and the fluid flow in the pores is laminar [68]. The flow regime of fluid (liquid or gas) through porous media (e.g., textiles) is generally characterized by the Reynolds number. According to the kinetic theory, the flow in the tube is fully laminar when $Re \leq 2,300$, transient flow in the range of $2,300 < Re < 4,000$, for $Re \geq 4,000$, the flow is turbulent [74].

Darcy's law is not always applicable, e.g., an increase of pressure gradient leads to a higher Re value (a larger fluid velocity), and the inertia effects must be considered. The inertia effect occurs when the flow regime is approaching the transition region between laminar and turbulent flow [75]. However, Darcy's law does not relate structural parameters of porous materials (porosity, tortuosity, and capillary effect) to their local permeability [67]. Two major modifications of Darcy's law were made by Forchheimer in 1901 and Brinkman in 1947 (see Table 1.1.). In Forchheimer's proposed model, the higher Reynolds number effects were evaluated by adding a non-linear term to the Darcy equation. However, the Forchheimer equation is not accurate enough to solve the flow of highly porous and confined media. Brinkman analyzed the viscous and higher porosity effects. Brinkman equation included a second-order viscous term with an equivalent viscosity for the porous medium. The Laplacian operator in the equation enables to simulate the flow around the finite porous media with a boundary between the open and the porous regions [51], [5].

Table 1.1. Analytical models of permeability

Analytical model	Relation	Explanation
Darcy's law [67]	$v = K \frac{\Delta p}{\mu L}$ or $K = \frac{\mu L v}{\Delta p}$	v – the fluid velocity (m/s), K – local permeability coefficient (m ²), Δp – pressure drop (Pa), μ – dynamic viscosity of the fluid (Pa·s), L – thickness of the fabric (m) or the flow length [67].
Hagen–Poiseuille model with consideration of the Stokes equation [71]	$q = \frac{\pi \mu d_p^4 \Delta p}{128 \mu L}$	d_p – diameter of the pore (m), m – number of pores, q – the flow rate of the liquid through the pore (m ³ /s) [67]. The air permeability R m/s can be obtained from relation $R = \frac{q}{S_t}$; S_t is the tested fabric area [83].
Kozeny–Carman equation used in the publication [67]	$K = \frac{\varepsilon^3}{180(1 - \varepsilon)^2} d_y^2$	ε – porosity, d_y – yarn diameter (m).
Modified Kozeny–Carman equation [82]	$K = C_f \left(\frac{\varepsilon}{1 - \varepsilon} \right)^{(1+D_T)/2} \lambda_{max}^2$	In $C_f = \frac{(\pi D_f)^{(1-D_T)/2} [4(2-D_f)]^{(1+D_T)/2}}{128(3+D_T-D_f)}$, λ_{max} – the maximum pore diameter, the fractal dimensions D_f for pore spaces, D_T for tortuosity. The maximum pore diameter can be obtained from the expression $\lambda_{max} = \sqrt{\frac{\varepsilon}{1-\varepsilon}} \cdot d$, d – particle diameter [82].
Kozeny–Carman equation [84], [82]	$K = \frac{\varepsilon^3}{c S_0^2 (1 - \varepsilon)^2}$ It should be noted that the determination of $c S_0^2$ from the experimental data, using the cover factor, was presented by [85]. In the case of the tortuosity of the capillaries: $K = \frac{\varepsilon^3}{k S_0^2 (1 - \varepsilon)^2}$	S_0 – specific surface area exposed to the fluid per unit volume of solid material (or a shape factor), c – Kozeny constant, k – Kozeny–Carman constant as follows $k = c \tau^2$, where τ is tortuosity and is defined as the ratio of the actual length of the flow path to the straight length [82]. In literature [5], [82], Kozeny constant is approximately $c = 5$ for beds that are packed with spherical particles.
One form of Kozeny–Carman equation [81]	$K = \frac{R^2 (1 - V_f)^3}{4c (V_f)^2}$	R – radius of circular fibers, V_f – volume fraction of fiber $V_f = 1 - \varepsilon$.
Forchheimer equation used in the publication [67]	$\frac{\Delta p}{L} = \frac{\mu}{K} v + \frac{c}{\sqrt{K}} \rho v^2$ Note: in the case of $c = 0$, the equation becomes Darcy's equation.	According to [51], d_y – the solid particle size in a porous medium. The parameters c and K can be determined by empirical relationships, such as given by Ergun in 1952. K denotes the medium permeability. $c = \frac{1.75}{\sqrt{150} \varepsilon^2}$, $K = \frac{\varepsilon^3 d_y^2}{150(1-\varepsilon)^2}$.

In the middle of the 20th century, the scientists investigated the rate of liquid/gas passage through porous materials. It has been found that with an improvement in the filtration rate, the dependence of the permeability on the pressure differential is non-linear [71]. Many researchers, like Zhu et al. [76], Lamb and Costanza [77], Kothari and Newton [78], have studied the influence on air permeability of various characteristics of textile structures. The common approach is to assume that the inter yarn pores of woven fabrics are parallel tubes, and the viscosity flow in one single long tube obeys Hagen–Poiseuille expression [79].

According to Ngo and Tamma [5], one of the significant developments in porous media flow was done by Kozeny in 1927. The main idea was that the porous media can be displayed by using an assemblage of channels of various cross-sections that are of specific length [5]. Carman [80] presented Kozeny–Carman equation based on the capillary theory (see Table 1.1.), which portrayed a better agreement with the experimental data than Kozeny’s equation. The Kozeny–Carman equation was initially introduced to predict isotropic local permeability of granular beds, consisting of ellipsoids. The equation is valid for porous media that is made of fibers [81]. The Kozeny–Carman equation is a semi-empirical relation, where the local permeability K depends on the porosity ε , Kozeny constant c , and specific surface area S . Generally, the constant c is obtained from the experimental data or numerically. For this reason, the relation is frequently modified in different application fields in order to improve the estimation of permeability by taking into account the non-isotropic properties of the porous media. In accordance with [82], the Kozeny–Carman constant k is not a constant (fixed). The researchers presented a summary of modifications of the Kozeny–Carman equations and proposed an analytical model for the permeability in homogeneous porous media, which was based on the fractal parameters of porous media and capillary model [82]. The Kozeny–Carman constant k was presented as a function, depending on the microstructural parameters, i.e., porosity and fractal dimensions (see Table 1.1.). This modification of the Kozeny–Carman equation can be applied to the fully developed laminar Newtonian fluid flow and isotropy unconsolidated porous media whose pore distribution follows the fractal scaling law [82]. The most common analytical models of permeability are shown in Table 1.1.

Gebart [81] proposed a model for the resin flow in non-isotropic porous media. The methodology and equations of longitudinal and transverse local permeability are based on the assumption of circular fiber cross-section and the specified ideal fiber arrangements in the intra-tow region. The local permeability to flow along the fibers is defined by Eq. 15. The expression (Eq. 15) for the longitudinal flow has the same form as the Kozeny–Carman equation. The permeability to cross-flow is characterized by Eq. 16. Two types of quadratic and hexagonal fiber arrangement were analyzed and compared with the experimental data [81]. Fig. 1.10. depicts idealized intra-tow filaments and the representative cell for quadratic and hexagonal fiber packing [81].

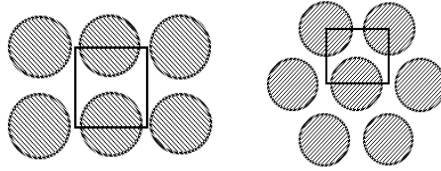


Fig. 1.10. Idealized unidirectional reinforcement and a representative cell for quadratic (a) and hexagonal (b) fiber packing [81]

$$K_{\parallel} = \frac{8R^2 (1 - V_f)^3}{c V_f^2}, \quad (15)$$

$$K_{\perp} = C_1 \left(\sqrt{\frac{V_{fmax}}{V_f}} - 1 \right)^{\frac{5}{2}} R^2; \quad (16)$$

where R – radius of fiber, V_f – fiber volume fraction, V_{fmax} – maximum fiber volume fraction. The parameters C_1 and V_{fmax} depend on the fiber arrangement [81]. The parameter c (equivalent Kozeny constant) depends on the fiber volume fraction and fiber arrangement. The constant parameters of different fiber arrangements that are used in Eq. 15 and Eq. 16 are shown in Table 1.2. [81]. Ngo and Tamma [5] proposed a numerical model to predict the local permeability of porous fibrous media on micro-scale by using a finite element approach. In the intra-tow region, the local permeability of the porous media (i.e., fiber tow) was determined by Eq. 15 and Eq. 16 [5].

Table 1.2. Parameter values of equations [81]

Fiber arrangement	C_1	V_{fmax}	c	k
Quadratic	$\frac{16}{9\pi\sqrt{2}}$	$\frac{\pi}{4}$	57	1.78
Hexagonal	$\frac{16}{9\pi\sqrt{6}}$	$\frac{\pi}{2\sqrt{3}}$	53	1.66

Note: in work [86], it was suggested to use $c = 100$ instead of 57 for the lower volume fractions.

Parada et al. [87] have investigated wicking behavior in cotton textiles, considering the dual-porosity diffusivity. Wicking is the spontaneous liquid imbibition due to the capillary forces in textiles [87]. This study intended to develop a simulation of complex dynamic wicking behavior inside the yarns (porous from itself) and between the yarns (voids). The diffusivity model was based on the Richards equation in order to simulate water transport in textile. The model relies on the relation between diffusivity and permeability. 2D geometry consisted of a rectangle of 20 mm width and 80 mm height. A Dirichlet boundary condition with the moisture content was set on the bottom of the computational domain. The time-dependent simulation

was carried out by Comsol software. This model explores the effect of gravity on moisture transport [87]. Nordlund and Lundstrom [88] modeled the local permeability of multiscale reinforcements (biaxial non-crimp fabric). Three representative unit cell models were developed in order to study the effect of multi-scale porosity in local permeability models. The first model geometry consists of the porous fiber bundles and the inter-bundle channels, the second model consists of the inter-bundle channels, and the third model is an extension of the second model with modifications of boundary conditions that take into account the effect of the flow inside the fiber bundles [88]. The permeability of models was determined from Darcy's law. The governing equations of multi-scale fabrics models for the incompressible Newtonian flow in the inter-bundle channel domain were expressed as Navier–Stokes equation (momentum equation) and the continuity equation; the creeping flow in a fiber bundle domain was described by Brinkman's equation. In the third model, the influence of the flow through the fiber bundles was represented by slip velocities at the channel/bundle interfaces, parallel to the pressure gradient [88]. The numerical simulations were done by using ANSYS CFX5.7.1 software. Furthermore, the permeability of textile reinforcements was investigated by Verleye et al. [89], [86]. The scheme of different scales and equations is shown in Fig. 1.11.

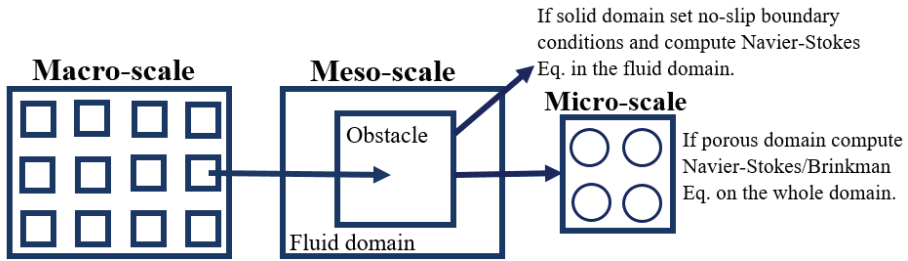


Fig. 1.11. Different scales and mathematical equations [89]

The mathematical model was made under the following assumptions that the fluid flow is creeping, single-phase, isothermal, unidirectional saturated flow of a Newtonian fluid [89]. The geometry of a single layer and multi-layered model of the reinforcement was designed with the WiseTex software and LamTex software. The numerical simulations were done by using FlowTex software that is based on a Lattice Boltzmann for fluid flow and finite-difference algorithms that allows solving (Navier-) Stokes and Brinkmann equations. In order to determine the permeability in the macro-scale of textile structure, Darcy's law was applied after the simulation of fluid flow through a unit cell, since textile has a periodic pattern. The computational models took into account the possible porosity of the material's yarns and local permeability tensor [89]. The local permeability was approximated according to the investigations of [90], [91]. Indeed, in the case of architectural composites, the resin flow can be observed between the yarns, formed by thousands of unidirectional fibers (inter-yarn zone), and even within them (intra-yarn zone) [92]. Geoffre et al. [92] investigated the influence of intra-yarn flows on the whole 3D woven fabric numerical

permeability. The dual-scale permeability problem was solved by using a mixed velocity-pressure finite element formulation for the Stokes–Darcy coupled flow.

The air permeability of knitted fabric with rib and interlock structures was investigated by using CFD by Dehkordi et al. [93]. Two turbulent models, i.e., $k-\varepsilon$ and $k-w$ from the group of the Eddy Viscosity Models (EVMs), were applied on a unit cell of the knitted fabric structure. One of the tasks was to create the 3D geometry of a knitted fabric loop. It was done by using the CATIA software. It has been found that an increase in the loop density of the knitted fabric led to a decrease in the air permeability. It has been demonstrated that by using the same loop density knitted fabric with an interlock structure contains less air permeability than with the knitted fabric with a rib structure [93]. The air permeability of plain knitted fabrics, using CFD (Fluent software), was studied by Mezarcioc et al. [83]. The 3D flow was simulated, assuming that it is a laminar flow. The interstices between the threads were depicted as circular shapes (see Fig. 1.12.). The numerical results of the CFD showed a good agreement with the experimental and theoretical results [83].

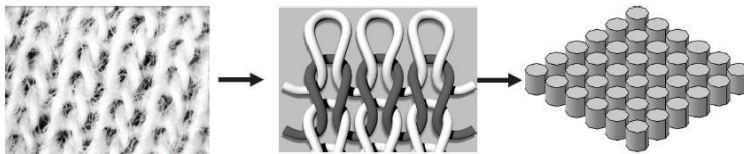


Fig. 1.12. Approximation of the plain knitted fabric [83]

The air permeability of one-layer woven structures based on the jet system was presented by Angelova et al. [94]. The interstices between the threads were depicted as the systems of jets, forming circular or square orifices. CFD simulation demonstrated that the shape of the interstices has no practical effect on the flow field after the woven structure [94]. One of the results was that 4×4 yarns with 9 interstice systems are enough to simulate the 3D fluid flow through a one-layer of the woven fabric. This approximation of the woven structure to the jet systems was a compromise between the time of the CPU and the necessary flow development [94]. Puszkarz et al. [95] have numerically investigated the air permeability of the double layer knitted fabrics. The application of SolidWorks Flow simulation was performed on the mono-fiber model and the multi-fiber model in micro-scale. The results showed that one of the important factors for the theoretical prediction efficiency was the inclusion of fibers and free space between them [95].

1.5. Water-vapor resistance and water-vapor permeability

The water-vapor permeability (WVP) coefficient of textile materials is generally understood as the ability of a permeable fabric to transmit water vapor through textile structure, usually expressed in units $\text{g/m}^2/24\text{h}$ [66]. The researchers Gidik et al. [96] measured the water-vapor permeability of different textiles; the experiment was carried out by using “the cup method” described by the British Standard (BS 7209). It has been found that the water-vapor permeability values reduce with an increase in the thickness of the air layer and the number of textile layers. The other outcome was that an increase in the water pressure gradient leads to an increase in the water-vapor

permeability value. Furthermore, the researchers have investigated the impact of the air velocity on the water-vapor permeability measurements. The results on both hydrophilic and hydrophobic fabrics demonstrated a high variation in the results when the location of the cups inside the climatic chamber has been changed [96].

1.6. Thermal resistance

The heat transfer through textile is primarily associated with conductive, convective, and radiative heat transfer mechanisms. The heat transfer via conduction is highly influenced by the temperature gradient. Fourier's law of conduction can be used to calculate the effective thermal conductivity (K_{eff}) of textile structures (see Eq. 17) [51], [97].

$$K_{eff} = \frac{Q \cdot h}{A \Delta T}, \quad (17)$$

$$R_{ct} = \frac{\Delta T}{Q/A}; \quad (18)$$

where Q – the heat flow, A – the surface area, h – the thickness of fabric, and ΔT is the temperature difference [97].

The most significant thermal property of a fabric is insulation against the heat flow in a cold environment in order to maintain the normal body temperature [97]. The insulation property of a fabric is measured by the thermal resistance. The thermal resistance (R_{ct}) of the fabric can be expressed by electrical analogy, according to Ohm's Law (see Eq. 19) [97]. By combining Eq. 17 and Eq. 18, the thermal resistance of fabric can be expressed as its effective thermal conductivity (see Eq. 19) [97].

$$R_{ct} = \frac{h}{K_{eff}}. \quad (19)$$


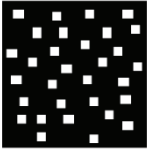
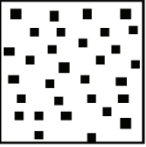

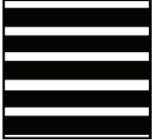
The effective thermal conductivity of two-phase materials with simple physical structures can be calculated by using existing fundamental structural models (see Table 1.3.) [98]. The series and parallel models illustrate a laminate (layered) structure of the phases [98]. In addition, two forms of Maxwell–Eucken (ME1 and ME2) and EMT (Effective Media Theory) are based on the phases being continuous and/or dispersed: the Maxwell–Eucken model represents one continuous phase and one or more dispersed phases, while EMT represents all phases that are being mutually dispersed [98]. The thermal conductivity of textile fabrics is determined by the thermal conductivity of fibers, yarns, and fabric construction, which accounts for the majority of fabric porosity [99]. Militky et al. [99] used two-phase models (parallel and serial) to investigate the thermal conductivity of the woven fabric. The parallel arrangement denoted the upper limit of the thermal conductivity value, while the serial arrangement denoted the lower limit. The researchers have suggested to compute the arithmetic mean between the upper and lower limits of the thermal conductivity. In the proposed model, k_1 is the thermal conductivity of yarns (moist), k_2 – thermal conductivity of air, v_1 – volume porosity. This modification for wool PES blended woven fabrics demonstrated a good agreement with the experimental data. Dias et al.

[100] presented a theoretical model (see Eq. 20) for determining the effective thermal conductivity of knitted structures with different porosity and moisture content. It has been found that the effective thermal conductivity increases when the thermal conductivity of the fibers increases. Moreover, the water content in the pores increases, the thermal conductivity increases because of the higher thermal conductivity of the water [100].

$$K_{eff} = \frac{k_m k_a k_w}{(1 - \varepsilon_p) k_a k_w + (\varepsilon_p - \varepsilon_p w) k_m k_w + \varepsilon_p w k_m k_a}; \quad (20)$$

where w – moisture in the pores (water by volume fraction), k_a, k_w, k_m – thermal conductivities of air, water, moisture in the pores, respectively.

Table 1.3. Effective thermal conductivity models for two-phase materials [98]

Model	Effective thermal conductivity equation	Structure schematic
Parallel model Note: v_1, v_2 – volume fractions for two phases, $v_2 = 1 - v_1$.	$K_{eff} = v_1 k_1 + v_2 k_2$ Note: limit arrangement of yarns (black) and air (white) in conductivity model [99].	
Maxwell–Eucken1 (ME1) (k_1 = continuous phase, k_2 = dispersed phase)	$K_{eff} = \frac{v_1 k_1 + v_2 k_2 \frac{3k_1}{2k_1 + k_2}}{v_1 + v_2 \frac{3k_1}{2k_1 + k_2}}$	
Maxwell–Eucken 2 (ME2) (k_1 = dispersed phase, k_2 = continuous phase)	$K_{eff} = \frac{v_2 k_2 + v_1 k_1 \frac{3k_2}{2k_2 + k_1}}{v_2 + v_1 \frac{3k_2}{2k_2 + k_1}}$	
EMT model	$v_1 \frac{k_1 - K_{eff}}{k_1 + 2K_{eff}} + v_2 \frac{k_2 - K_{eff}}{k_2 - 2K_{eff}} = 0$	
Series model	$K_{eff} = \frac{1}{\frac{v_1}{k_1} + \frac{v_2}{k_2}} = \frac{k_1 k_2}{v_1 k_2 + (1 - v_1) k_1}$	

1.7. Concluding remarks

According to the literature overview, nowadays, the analysis and usage of smart materials and smart textile structures is a very important topic in the textile engineering. All textile fabrics by their essence are composite non-homogeneous structures; the analysis of physical behavior is complicated and requires sophisticated mathematical models. The physical behavior analysis of textile fabrics has been widely performed in a pre-computer era as well by developing and solving simplified analytical models. However, the really deep and physically comprehensive analysis is strongly related to the modern computing technologies. The power computational software, supported primarily by the finite element method, enables to represent the internal micro-geometry of fabrics as well as multi-physical phenomena adequately.

Obviously, the real full-sized textile garments cannot be investigated on a micro-scale because of the inherent limitations of computer resources. In reality, many engineering textile solutions are based on the standardized tests, such as thermal resistance, air permeability, water vapor resistance, etc. The results of such tests were practically acceptable for ordinary woven textile layers. However, the tests do not provide reliable information in case of new internal designs of fabric structures, such as 3D textiles. As most standard tests are based on the comprehension of fabric as a thin planar membrane, the physical phenomena taking place in the volume of the fabric (e.g., circulation of air and convective heat transfer within the fabric) may go “unnoticed”. Therefore, the micro-scale simulation of physical processes that are taking place by performing tests is an important issue. In recent decades, numerous researchers have made efforts to analyze and develop numerical models in order to simulate complex heat and mass transfer phenomena through thermal protective clothing.

This research is focused on applying the multiscale approach with the application to thermal resistance, air permeability, and water vapor resistance tests, performed on 3D textile structures. It enables to obtain the effective physical properties applicable in macro-scale and get deeper physical insight into the micro-scale physical phenomena, taking place during the tests.

2. DEVELOPMENT OF THE RESEARCH TECHNIQUE

The simulation of heat and mass transfer through textile by using computational fluid dynamics (CFD) tool requires solving two different problems. The first problem is the method of real textile approximation to a virtual model, and the second one is the modeling of the heat-transfer process itself [53]. The approximation of fabric is difficult due to the complex geometry that consists of yarns (meso-scale) and fibers (micro-scale). However, this is the multi-scale task from its nature (see Fig. 1.7.) of the fibrous medium. The fabrics usually consist of two types of porosity: the microporosity caused by the void spaces among the fibers in the yarns (pores inside the yarns) and the macroporosity, resulting from the void/open spaces among the yarns (pores between warp and weft yarns) [67].

The heat is transferred from the body via conduction, convection, radiation evaporation, and respiration [101]. The heat exchange between the human body and the environment may be described by the general heat balance equation [102].

$$M - W = C + R + E_{sk} + (C_{res} + E_{res}) + C_k; \quad (21)$$

where M denotes metabolic rate (internal energy production), W – external work (is small and usually ignored), C – heat loss by convection, R – heat loss by thermal radiation, E_{sk} – heat loss by evaporation from the skin, C_k – heat loss by thermal conduction, C_{res} – sensible heat loss due to respiration, and E_{res} – evaporative heat loss due to respiration in W/m^2 [102]. The rate of the heat transfer through respiration is typically at a lower level than the other rates of the heat transfer [102]. The heat transfer due to radiation can be ignored in cases of small temperature gradients [97].

The temperature and humidity of the environment can have a significant impact on the skin and internal temperature of the body. The metabolic heat is produced throughout the human body and is transferred to the skin layer via the thermo-regulatory system; in order to maintain the internal temperature of 37 ± 0.5 °C under different climatic conditions, the blood flows into the skin layer via the vasodilatation mechanism, releasing the heat to the environment [9], [102].

2.1. The concept of finite element method

The finite element method (FEM) is a powerful tool that enables various engineering and physical phenomenon problems to be solved numerically [35]. The FEM consists of governing equations and boundary conditions formulation, division of the computational domain into elements (discretization), interpolation function selection, determination of element properties, global equations assemble or merge, solutions for global equations, verification of the solution [103]. The fundamentals of the FEM for solving fluid flow and heat transfer can be represented by the system of differential equations (Eq. 22) with boundary conditions (Eq. 23) [35]:

$$Au = f \text{ in } \Omega, \quad (22)$$

$$Bu = t \text{ in } \Gamma; \quad (23)$$

where A is a system of governing equations, defined in the domain Ω , B is a system of some boundary functions, defined in the boundary Γ , and f , t are some functions. The solution can be obtained by applying the weighted residual method and yield [35]:

$$\int_{\Omega} W_j(A\bar{u} - f)d\Omega + \oint_{\Gamma} W_j(B\bar{u} - t)d\Gamma = 0; \quad (24)$$

where W_j ($j = 1, \dots, n$) are weighting functions and \bar{u} is an approximation to the unknown u :

$$u \approx \bar{u} = \sum_{j=1}^n N_j u_j; \quad (25)$$

where N_j are basis functions and u_j are the nodal values of the unknown. Substituting Eq. 25 with Eq. 24, Eq. 26 can be obtained, where \mathbf{K} is a square matrix, and \mathbf{u} , \mathbf{f} vectors [35].

$$\mathbf{Ku} = \mathbf{f}. \quad (26)$$

The Galerkin version of FEM is when $W_j = N_j$. It means that the minimum energy norm errors and preserves the symmetry of matrix \mathbf{K} [35].

The formulation of equations of the heat and mass transport through textile were represented by different authors. According to Neves et al. [104] a textile can be represented as a porous material composed of fibers, bound water in fibers, and gas (air and water-vapor). The 1D transient diffusion of heat and mass through hygroscopic porous materials was investigated by Gibson and Charmchi [105]. In accordance with [105], the textile can be defined as a homogeneous medium with two phases, i.e., a gaseous phase (air and water vapor) and a solid phase (fiber and bound water in fibers). There were made assumptions that the bounded water in fibers can be assumed immobile and in equilibrium with the water vapor in the pores, and the gas phase follows the ideal gas law. In the proposed model, the heat transfer along the textile thickness was expressed by the conservative energy equation for the textile control volume, see Eq. 27 [105].

$$\rho C_p \frac{\partial T}{\partial t} + \frac{\partial}{\partial x} \left(-k_{eff} \frac{\partial T}{\partial x} \right) + (Q_l + \Delta h_{vap}) \dot{m}_{sv} = 0. \quad (27)$$

The first term in Eq. 27 is the accumulation of energy in the volume of textile control, the second term represents the heat transfer due to conduction, and the third term is the energy associated with the sorption/desorption of water between the fibers and the gaseous phase [104]. There, C_p denotes the mass fraction weighted average constant pressure heat capacity, $J/(kg \cdot K)$, k_{eff} – effective thermal conductivity of the porous material, $J/(s \cdot m \cdot K)$, \dot{m}_{sv} – mass desorption rate of water from fiber to the gaseous phase $kg/(s \cdot m^3)$, Δh_{vap} – enthalpy of water vaporization, J/kg , Q_l – enthalpy of water desorption from the solid phase (fiber) to liquid phase, J/kg [105].

The continuity equation of the solid phase (textile) is expressed by Eq. 28. The continuity equation of the gas phase is expressed by Eq. 29.

$$\rho_w \frac{\partial}{\partial t} (\varepsilon_{bw}) + \dot{m}_{sv} = 0 \text{ or } \frac{\partial}{\partial t} (\varepsilon_{bw}) + \frac{\dot{m}_{sv}}{\rho_w}, \quad (28)$$

$$\frac{\partial}{\partial t} (\varepsilon_\gamma \rho_v) - \dot{m}_{sv} = \frac{\partial}{\partial x} \left(D_{eff} \frac{\partial \rho_v}{\partial x} \right); \quad (29)$$

where D_{eff} – effective diffusivity of gas m^2/s , ε_{bw} denotes the volume fraction of the water dissolved in the solid phase and ε_γ is the volume fraction of the gas phase, ρ_w – density of water kg/m^3 , ρ_v – density of water vapor kg/m^3 [105].

2.2. The definition of representative volume element

In this thesis, the representative volume element (RVE) identifies the microstructure's physical and geometrical properties. The selection of the RVE is quite a sensitive task. The RVE should be large enough to represent the microstructure and/or the flow characteristics [73] and should be small enough to provide efficient computational modeling. The RVE is a material microstructure model that can be used to calculate the response of a homogenized macroscopic continuum in a macroscopic material point [106]. The accuracy of the modeling of a heterogeneous material (e.g., porous media, composites) is strongly influenced by the selection of the RVE. The minimum size of a material RVE is a crucial question in the application of such constitutive models that describe the composite response via homogeneous "overall" properties [107].

There seem to be two different ways, according to [107], to define a RVE. The first definition is based on the idea that in order to characterize the macroscopic composite constitutive response, the statistical nature of the microstructure of actual composites must be recognized. The smallest RVE should include virtually a sampling of all possible microstructural configurations that occur in the composite (such as voids, cracks, fibers, etc.) [106], [107]. Such definition leads to a considerably large RVE in the case of a non-regular and non-uniform microstructure. For the approach to be valid, the RVE must be chosen to be "sufficiently large" in comparison to the microstructural size. This concept is often used when a microstructure computer model is developed, based on the statistical data that was obtained experimentally [106]–[108]. However, when all geometrical information is considered, the challenges such as non-periodic RVEs or small geometric features are difficult to mesh [109]. According to [107], the second definition of the RVE is the smallest material volume element of the composite for which the usual spatially constant "overall modulus" macroscopic constitutive representation is a sufficiently accurate model to represent the mean constitutive response. The idea is to take the average representation of characteristics by using this computational homogenization approach.

According to the literature [108], RVE is the infinite length scale limit that is relative to the micro-scale (or the length scale of a single heterogeneity), where the material appears uniform and thus the continuum concepts apply. Alotaibi et al. [110] have investigated the effect of local tow curvature on dual-scale permeability in woven fabrics. RVE was defined as the smallest volume at the fiber/tow level, in which a measurement can be taken to represent the entire volume (macro-scale) [110]. According to literature [109], the smallest periodic RVE of plain weave woven structures consists of at least two warp and two weft yarns.

2.3. A representative volume element of 3D textile structure in micro-scale

Spacer fabrics are 3D textile structures that are made up of two separate outer fabric layers, joined by the spacer yarns (which are generally monofilaments) or a layer. Spacer fabrics can be made by using warp knitting, weft knitting, weaving, non-woven, or braiding technologies [111], [112]. The space between the two layers (top

and bottom) is filled with air and compression-resistant threads, allowing for the realization of several functions, such as mechanical cushioning, mechanical pressure distribution, air and moisture permeability, and thermal insulation [113]. For these reasons, spacer fabrics are used as moisture- and thermal-regulating functional components in a variety of applications, including the medical textiles, automotive textiles, outdoor textiles, protective textiles, geotextiles, and sport textiles. Furthermore, the materials that are most commonly used for spacer fabrics are polyester multifilament and monofilament, which are highly commercialized and low-cost products [113], [114].

The spacer yarns are used to connect two fabric layers, and their inclination angle and length depend on the number of needles underlapped between front- and back-needle bars [114]. When the spacer yarns are perpendicular to the outer layers, the maximum inclination angle is 90° . Increasing the inclination angle causes the fabric thickness to increase [112]. The compression behavior of warp-knitted spacer fabric was analyzed in work [114], where two different diameters 0.2 and 0.16 mm of spacer yarns were performed, whereas the angles that were formed between the outer layers and the left oblique spacer yarns are 84.14° , 67.85° , and 52.58° ; the angles between the outer layers and the right oblique spacer yarns are 76.34° , 66.87° , and 56.45° [114]. These angle differences are due to the difficulty of producing fabrics with precisely symmetrical spacer yarns in a complicated manufacturing and finishing process [114]. The spacer layer in the publication [112] was made of polyester monofilaments with diameters of 0.08, 0.09, and 0.1 mm. The air permeability of two-layer woven structure ensembles was investigated by Kyosov et al. [115]. The lowest air permeability coefficient was achieved when the layers were separated by 3–5 mm. However, most studies of the woven “sandwich” structures are orientated into the mechanical behavior (like compression [116], tensile properties [117], [118]).

One of the challenges is to recreate the precise geometry of a RVE of 3D textile structures. Probably, the most realistic reconstruction of 3D spacer fabric can be done by using μ CT scan system or SEM. In literature [119], there was used both techniques because μ CT has some resolution limitations. The intention was to obtain more details of the fabric's outer layer structure in order to gain a better understanding of how the spacer monofilaments are bound by the outer layers [119]. It was demonstrated that each outer layer of 3D spacer fabric could be divided into the top layer and the bottom layer of equal thickness. However, it was impossible to define well the shapes of monofilament loops that are embedded in the outer layer [119]. The mechanical simulation of 3D mesh fabric (a special type of warp-knitted spacer fabric whose outer layers are meshed) was investigated by Lotz et al. [120]. A μ CT scan of the mesh fabric was performed to create the exact 3D reconstruction from the obtained slices. However, the multifilament loops in the outer layers are not well reconstructed due to the resolution limitations of the μ CT system. As a result, in most cases, the 3D geometry cannot be directly meshed and implied into the FE software for additional modeling [120]. These studies demonstrated the realistic reconstruction of 3D spacer fabric. However, it requires the time of experimental research, specific laboratory

equipment, or quite expensive measurements. Unfortunately, there has been very little research on heat and moisture transfer through 3D spacer fabrics.

There are software packages like Wisetex, TexGen, GeoDict for contact modeling between the yarns of 3D textile structures [113]. In this thesis, firstly, the author tried to use free and open-source TexGen software to create one-layer geometry of 3D woven structures. After geometry generation, the RVE of the textile structure was exported and imported into Comsol Multiphysics software for further modeling. The intention was to create close to real geometry of one-layer textile, then add one more layer and investigate the behavior of the textile structure. Finally, in order to approximate the geometry of two-layer RVE and spacer yarn/spacer layer, all these procedures are done, considering the air permeability value. However, the quality of the mesh was quite poor. For this reason, the final simulations were performed by generating the geometry in the Comsol Multiphysics environment.

In this study, the RVE of 3D textile structure in micro-scale is based on a literature review. The air permeability (AP) coefficient of one-layer woven fabrics was experimentally investigated by Zupin et al. [8]. The researchers set and measured the construction parameters for 36 woven fabric samples. The air permeability measurements were carried out with the Air Permeability tester FX 3300 Labotester III (Textest Instruments) [8]. Three samples of plain weave were analyzed to reproduce a RVE of one-layer textile. The experimental results of the settings and the measurements that were considered are shown in Table 2.1.

Table 2.1. Set and measured construction parameters [8]

Sample number	Set density warp/weft	Measured warp density (ends/cm)	Measured weft density (picks/cm)	Thickness (mm)	Measured air permeability (mm/s)	Coeff. of var. (%)
1	22/15	21	15	0.439	2,391.67	8.20
2	22/20	21	20	0.438	1,571.67	1.58
3	29.3/15	28	15	0.468	1,268.33	1.42

Firstly, the TexGen software was used to generate complex internal geometry of one-layer textile. The RVE consists of yarns that are considered repetitive and only modeled at their minimum repetitive length. The yarn is depicted as a solid volume without individual fibers, from which it is composed. The main reason why yarn can be represented as a solid volume is much more useful for computational analysis of textile properties (mainly due to the CPU speed and memory limitations) [14]. Two factors were taken into account: the path of the yarn through the textile and the cross-section shape. A series of vectors, representing the center lines of the yarns in 3D space, is used to specify the yarn paths. The cross-section of the yarn is the 2D shape of the yarn, when cut by a plane perpendicular to the tangent path of the yarn. Various cross-section shapes and the path of the yarn were defined by using parametric equations in 2D, such as the ellipse [121], a modified lenticular shape [122]. The cross-section shape of yarns is different due to the deformation that occurs during the weaving process.

In this work, it was first assumed that the shape of the yarns is lenticular. The generated geometry model of the textile layer was imported into Comsol Multiphysics software by using the STEP file format (see Fig. 2.1. a)). In Comsol Multiphysics, the author of the dissertation did booleans operations (difference and union) to receive a solid volume of yarns. The result is depicted in Fig. 2.1. c). Moreover, using the work plane of the xy axis, at height $z = 0.11$ mm, the view of the top is demonstrated (see Fig. 2.2. b)). Green lines denote intersections between the work plane and the yarns. However, considering the first sample, which has 22/15 structural density, the RVE had warnings with meshing. The main warnings were due to the narrow intersection regions, sharp edges. As a result, some mesh elements have a low quality (0.002822). Furthermore, the edges were much shorter than the specified minimum element size. Fig. 2.3. depicts the coarser mesh. The blue color depicts the narrow regions that are much smaller than the minimum element size.

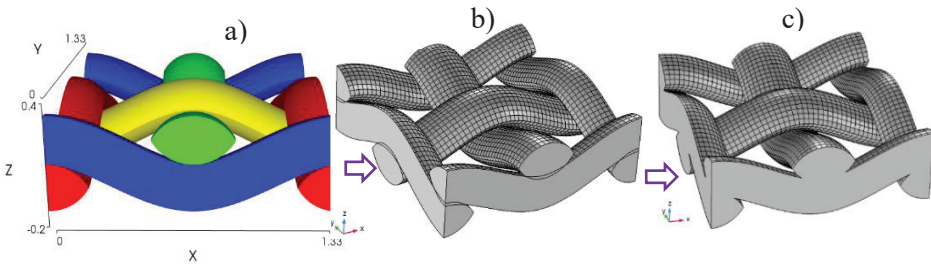


Fig. 2.1. The geometry of sample 22/15 created with TexGen (a), imported geometry into Comsol Multiphysics (b), the same geometry after booleans operations in the Comsol Multiphysics environment (c)

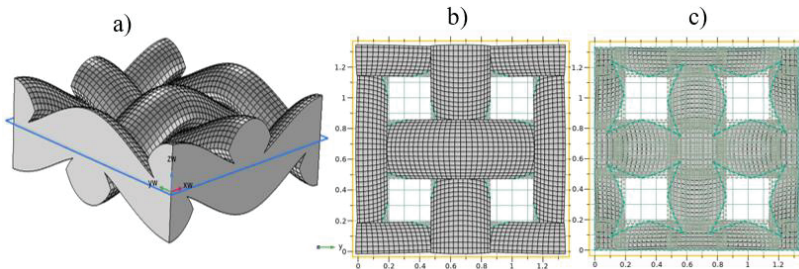


Fig. 2.2. The work plane of xy, at height $z = 0.11$ mm; the work plane is depicted as a blue plane (a), top view of the geometry (b), the intersections between the yarns and the work plain are depicted in green (c)

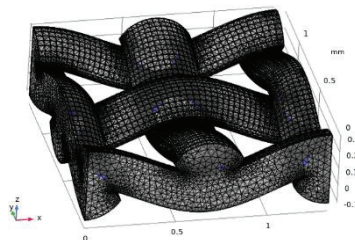


Fig. 2.3. The generated coarser mesh; the blue color depicts the elements that are smaller than the minimum size of the element

A low mesh element quality leads to the inverted mesh elements, which can cause convergence problems [123]. The quality of the mesh element is a dimensionless number between 0 and 1, where 1 indicates a perfectly regular element and 0 indicates a degenerated element. In this thesis, the *Skewness measure* was considered. The *Skewness measure* is a measure of the equiangular skew and is defined as the minimum of the following quantity:

$$1 - \max\left(\frac{\theta - \theta_e}{180 - \theta_e}, \frac{\theta_e - \theta}{\theta_e}\right); \quad (30)$$

where θ denotes the angle over a vertex (2D) or edge (3D) in the element, θ_e is the angle of the corresponding edge or vertex in an ideal element, and the minimum is taken over all vertices (2D) or edges (3D) of the element [123]. It is generally accepted that the elements with a quality of less than 0.1 are of low quality. In many cases, it is recommended to avoid the elements with a quality of less than 0.01 (extremely low quality). If these low-quality elements are placed in an important part of the domain, it can cause convergence issues [123].

Avoiding the convergence problems, for a detailed analysis of the air permeability coefficient, it was assumed that the cross-section shape of the yarn is an ellipse, and instead of importing geometry from the TexGen software, the geometry in Comsol Multiphysics software was directly created. The created model is flexible, which allowed to change the number of loops. In addition, from Fig. 2.2. b, it could be seen that the void space between the inter yarn can be approximated to squares. Thus, there has been made one more simplification of one-layer textile that inter yarn pores are squares. The internal geometry structure has been simplified to save computational time for the simulation. Following the experimental measures (see Table 2.1.), the one-layer textile was built. In this thesis, three samples were investigated. The purpose was to create a realistic RVE of the 3D textile. For this reason, there were combined two replicas of one-layer structure respectively to each sample. In order to create an equivalent 3D textile layer, the top and bottom layers were connected with spacer yarn. In all cases, the RVE consists of the air domain and the textile layer in the developed simulation. The textile domain size varies due to the structural density differences. The spacer yarn radius was selected 0.08 mm and inclination angle 90° , the initial distance e between the layers was 3.06 mm. All models that were used in this research are described in Table 2.2. and depicted in Fig. 2.4. For example, the model title *Model x_a* represents the sample number x that was measured (see Table 2.1.), and the letter a denotes the geometry modification.

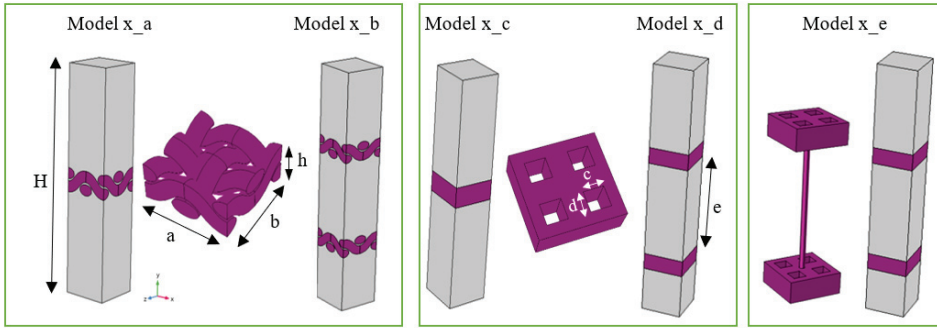


Fig. 2.4. The general representation of RVE where x denotes the sample number

Table 2.2. Air domain and textile layer parameters

Model	Length and width of domain $a \times b$ (mm)	Height of air domain H (mm)	The thickness of the textile layer h (mm)	Length and width of pore $c \times d$ (mm)	Distance between two layers of textile e (mm)
<i>Model 1 a</i>	1.1 x 1.1	10	0.439	-	-
<i>Model 2 a</i>	0.98 x 0.98	10	0.438	-	-
<i>Model 3 a</i>	0.85 x 0.85	10	0.468	-	-
<i>Model 1 b</i>	1.1 x 1.1	10	0.439	-	3.06
<i>Model 2 b</i>	0.98 x 0.98	10	0.438	-	3.06
<i>Model 3 b</i>	0.85 x 0.85	10	0.468	-	3.06
<i>Model 1 c</i>	1.1 x 1.1	10	0.439	0.263 x 0.263	-
<i>Model 2 c</i>	0.98 x 0.98	10	0.438	0.195 x 0.195	-
<i>Model 3 c</i>	0.85 x 0.85	10	0.468	0.155 x 0.155	-
<i>Model 1 d</i>	1.1 x 1.1	10	0.439	0.263 x 0.263	3.06
<i>Model 2 d</i>	0.98 x 0.98	10	0.438	0.195 x 0.195	3.06
<i>Model 3 d</i>	0.85 x 0.85	10	0.468	0.155 x 0.155	3.06
<i>Model 1 e</i>	1.1 x 1.1	10	0.439	0.263 x 0.263	3.06
<i>Model 2 e</i>	0.98 x 0.98	10	0.438	0.195 x 0.195	3.06
<i>Model 3 e</i>	0.85 x 0.85	10	0.468	0.155 x 0.155	3.06

The equivalent 3D textile geometry represents *Model 1_e*, *Model 2_e*, and *Model 3_e*, which consist of two replicas of *Model 1_c*, *Model 2_c*, and *Model 3_c* respectively, and the space yarn. The *Model x_c* presents simplified internal textile geometry based on *Model x_a*. *Model x_b* and *Model x_d* depict two-layer textile with distance e between the top and bottom layers.

2.4. The numerical modeling of measurement of air permeability coefficient

It is generally considered that the air permeability (AP) coefficient is a very important clothing comfort property that affects liquid and vapor transmission properties, and thermal resistance of clothing [9]. In many cases, it is the decisive factor for determining the comfort of clothes, regarding their thermal properties [67],[8]. In this thesis, AP models were developed, taking into account internal (local)

permeability \mathbf{K} , m^2 of yarns. A common approach is that the permeability of a unit cell of textile is calculated from Darcy's law. The general form of Darcy's law is expressed below [88]:

$$\frac{\mathbf{Q}}{A_s} = \mathbf{K} \frac{\Delta p}{\mu \cdot L}; \quad (31)$$

where \mathbf{Q} – volumetric flow rate (m^3/s), \mathbf{K} – local permeability coefficient (m^2), Δp – pressure drop (Pa), μ – dynamic viscosity of the fluid ($\text{Pa}\cdot\text{s}$), and L – thickness of the textile (m), A_s – cross-sectional area (m^2). The volumetric flow rate \mathbf{Q} can be obtained by integrating the velocity field \mathbf{u}_{cfd} , resulting from the CFD computations, over a cross-sectional area A_s (m^2) of the fluid domain with normal vector \mathbf{n} , according to [88]:

$$\mathbf{Q} = \iint_{A_s} \mathbf{u}_{\text{cfd}} \cdot \mathbf{n} \, dA. \quad (32)$$

According to Swery et al. [124], the resulting mass flow rate of the fluid (resin) through the outlet boundary can be used to compute the local permeability. Furthermore, local permeabilities can be computed in different directions (e.g., weft and warp). Most of these studies consider resin flow that is used in liquid composite molding (LCM) processes. The numerical simulations cover Stokes flow (with impervious yarns), Stokes–Darcy coupled flow (with permeable yarns) [92]. Furthermore, the local permeability can be obtained from the analytical models (see Table 1.1.).

In this thesis, the prediction of the air permeability (i.e., average velocity) AP coefficient through textile was made under the assumptions that the flow is incompressible Newtonian single-phase flow. Besides, the steady-state simulation was made, considering that the fluid has a low Re number, denoting that the airflow is laminar. The computational domain Ω consists of two subdomains Ω_1 and Ω_2 that depict air domain and porous media domain (textile), respectively. In order to determine the air permeability (AP) coefficient of textile structure, Navier–Stokes equations (Eq. 33) with the continuity equation (Eq. 34) were applied in Ω_1 subdomain, and Brinkman equations (Eq. 37) with the continuity equation (Eq. 34) were applied in Ω_2 subdomain. Fig. 2.5. illustrates the domains and boundary conditions $\partial\Omega$ that were used in the simulation. The summary of boundary conditions is shown in Table 2.3., where vector \mathbf{n} stands for the outer unit normal vector and \mathbf{t} is the tangential vector [125].

The Navier–Stokes equation Eq. 33 is known as the conservation of momentum equation. According to [126], the Eq. 33 consists of inertia (convection) term $(\mathbf{u} \cdot \nabla)\mathbf{u}$, divergence of the stress $-\mathbf{p}\mathbf{I} + \mu(\nabla\mathbf{u} + (\nabla\mathbf{u})^T)$, and external forces \mathbf{F} like gravity or vibrational excitation. In this study, it was assumed that there are no external forces. The term $-\nabla\mathbf{p}\mathbf{I}$ stands for pressure difference forces. It should be noted that in case of incompressible flow, the diffusion term is $\nabla \cdot \mu(\nabla\mathbf{u} + (\nabla\mathbf{u})^T) = \mu\nabla^2\mathbf{u}$.

$$\rho(\mathbf{u} \cdot \nabla)\mathbf{u} = \nabla \cdot [-p\mathbf{I} + \mu(\nabla\mathbf{u} + (\nabla\mathbf{u})^T)] + \mathbf{F} \text{ in } \Omega_1, \quad (33)$$

$$\rho\nabla \cdot (\mathbf{u}) = 0 \text{ in } \Omega_1; \quad (34)$$

In Comsol software, there is implemented the extended form of the Brinkman momentum equation that reads as Eq. 35 and continuity Eq. 36.

$$\begin{aligned} \frac{\rho}{\varepsilon_p} \left((\mathbf{u} \cdot \nabla) \frac{\mathbf{u}}{\varepsilon_p} \right) = \nabla \cdot \left[-p\mathbf{I} + \frac{\mu}{\varepsilon_p} (\nabla\mathbf{u} + (\nabla\mathbf{u})^T) - \frac{2}{3} \frac{\mu}{\varepsilon_p} (\nabla \cdot \mathbf{u})\mathbf{I} \right] - \\ - \left(\mu\mathbf{K}^{-1} + \beta_F \varepsilon_p \rho |\mathbf{u}| + \frac{Q_m}{\varepsilon_p^2} \right) \mathbf{u} + \mathbf{F} \text{ in } \Omega_2, \end{aligned} \quad (35)$$

$$\rho\nabla \cdot (\mathbf{u}) = Q_m \text{ in } \Omega_2; \quad (36)$$

The term Q_m stands for mass source, β_F – Forchheimer drag coefficient (inertial flow coefficient), ε_p – porosity, \mathbf{K} intrinsic/local permeability tensor in m^2 , the term $\frac{\mu}{\varepsilon_p}$ is known as effective viscosity. Assuming that there is no mass source, Eq. 36 reduces to Eq. 34. Furthermore, β_F is set to zero, there is no external forces \mathbf{F} , the term $-\frac{2}{3} \frac{\mu}{\varepsilon_p} (\nabla \cdot \mathbf{u})\mathbf{I}$ is zero due to incompressible flow ($\nabla \cdot \mathbf{u} = \mathbf{0}$). Eq. 35 is simplified to Eq. 37, which is applied in computational simulation.

$$\frac{\rho}{\varepsilon_p} \left((\mathbf{u} \cdot \nabla) \frac{\mathbf{u}}{\varepsilon_p} \right) = \nabla \cdot \left[-p\mathbf{I} + \frac{\mu}{\varepsilon_p} (\nabla\mathbf{u} + (\nabla\mathbf{u})^T) \right] - (\mu\mathbf{K}^{-1})\mathbf{u} \text{ in } \Omega_2. \quad (37)$$

The Brinkman equation (Eq. 37) is not straightforward due to the local permeability \mathbf{K} value as an input of intra-yarn (intra-tow region). The local permeability of a porous medium can be determined according to the analytical formulas (more details in subsection 1.4.) that demonstrate the relations between permeability and yarn porosity. According to [86], the local permeability of the textile reinforcements varies from 10^{-7} to 10^{-11} m^2 . In this study, the local permeability \mathbf{K} and porosity ε_p were used from literature [9]. The permeability \mathbf{K} was obtained according to Gebart's model [81], which takes into account the fiber arrangement. The experimental data that is used in the determination of coefficients were presented by Zupin et al. [8]. It was assumed that the porosity $\varepsilon_p = 0.58$, and the local permeability $\mathbf{K} = 1.64 \cdot 10^{-11} [\text{m}^2]$, in case the textile is isotropic and fiber arrangement is quadratic [9]. These material properties were applied in Ω_2 . It should be noted that in the general case, the local permeability tensor \mathbf{K} can be applied in Comsol environment, using Eq. 38. According to [5], [81], $k_{xx} = k_{\parallel}, k_{yy} = k_{zz} = k_{\perp}$, where k_{\parallel} indicates the flow-direction permeability, k_{\perp} – cross-flow permeability. The terms $k_{xy} = k_{yz} = k_{zx} \approx 0$. However, the different components of local permeability values are quite difficult to measure [92].

$$\mathbf{K} = \begin{bmatrix} k_{\parallel} & 0 & 0 \\ 0 & k_{\perp} & 0 \\ 0 & 0 & k_{\perp} \end{bmatrix}. \quad (38)$$

According to [8], the measurements with the Air Permeability tester FX 3300 Labotester III (Textest Instruments) were performed, the pressure drop was set at 200 [Pa] on the area of 20 cm². The summary of the boundary conditions that were used in the simulation is shown in Table 2.3. and illustrated in Fig. 2.5.

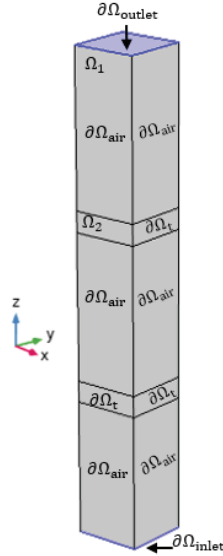


Fig. 2.5. Boundary conditions of a unit cell of three-dimensional textile

Table 2.3. Boundary conditions for the simulation of air permeability based on [125]

Surface	Boundary conditions	Settings and assumptions
on $\partial\Omega_t$	$\mathbf{u} = \mathbf{0}$	Wall condition: no slip. No-slip condition is assumed on the 3D textile surface. The fluid (air) velocity on this surface is zero.
on $\partial\Omega_{\text{air}}$	$\mathbf{u} \cdot \mathbf{n} = 0$ $\mathbf{K}_n - (\mathbf{K}_n \cdot \mathbf{n})\mathbf{n} = 0$ $\mathbf{K}_n = \mathbf{K}\mathbf{n}$ In the case of the air domain: $\mathbf{K} = \mu(\nabla\mathbf{u} + (\nabla\mathbf{u})^T)$ In case of porous media domain: $\mathbf{K} = \frac{\mu}{\varepsilon_p}(\nabla\mathbf{u} + (\nabla\mathbf{u})^T)$	Wall condition: slip. A slip condition is on the air surface that has no contact with the 3D textile layer.
on $\partial\Omega_{\text{inlet}}$	$\mathbf{n}^T[-p\mathbf{I} + \mathbf{K}]\mathbf{n} = -\hat{p}_0$ $\hat{p}_0 \geq p_0, \mathbf{u} \cdot \mathbf{t} = 0$ $p_0 = 200\text{Pa}$	Inlet (suppress backflow). According to the experiment, the pressure difference is 200 Pa. The pressure condition $p_0 = 200\text{ Pa}$ on $\partial\Omega_{\text{inlet}}$ surface was set on. In this simulation, two pressure boundary conditions on $\partial\Omega_{\text{inlet}}$ and $\partial\Omega_{\text{outlet}}$ surface were set on. For the solver, it takes extra time to recalculate velocity ($\mathbf{u} \cdot \mathbf{t} = 0$).
on $\partial\Omega_{\text{outlet}}$	$[-p\mathbf{I} + \mathbf{K}]\mathbf{n} = -\hat{p}_0\mathbf{n}$ $\hat{p}_0 \leq p_0$ $p_0 = 0\text{Pa}$	Outlet. Relative pressure $p_0 = 0\text{ Pa}$ on $\partial\Omega_{\text{outlet}}$ surface was set on. Physical meaning is that absolute pressure is equal to the reference pressure (1 [atm]). It can be expressed as: $p_A = p_{\text{ref}} + p_0$.

Navier–Stokes/Brinkman equations were solved by using the steady-state nonlinear solver. The first-order discretization for velocity and pressure approximation was applied (P₁+P₁).

The most common method to solve the nonlinear systems of equations is Newton’s method. The general idea is presented below. Given $\mathbf{F}: \mathbb{R}^n \rightarrow \mathbb{R}^n, \mathbf{F} = (\mathbf{f}_1, \dots, \mathbf{f}_n)^T$ and the task is to find the solution of nonlinear systems of equations Eq. 39 [127].

$$\mathbf{F}(\mathbf{x}) = \mathbf{0}. \quad (39)$$

\mathbf{F} is well defined and has continuous partial derivatives on the open set of \mathbb{R}^n [127]. Jacobian matrix $\mathbf{J}(\mathbf{x})$ was denoted (see Eq. 40). The first step is to assume that solution $\bar{\mathbf{x}}$ can be written as $\bar{\mathbf{x}} = x_0 + s$, where x_0 is some known guess of x , and s is a correction.

$$J(x) \equiv F'(x) \equiv \begin{bmatrix} f'_1(x) \\ \vdots \\ f'_n(x) \end{bmatrix} \equiv \begin{bmatrix} \nabla f_1(x)^T \\ \vdots \\ \nabla f_n(x)^T \end{bmatrix} \equiv \begin{bmatrix} \frac{\partial f_1}{\partial x_1}(x) & \dots & \frac{\partial f_1}{\partial x_n}(x) \\ \vdots & \dots & \vdots \\ \frac{\partial f_n}{\partial x_1}(x) & \dots & \frac{\partial f_n}{\partial x_n}(x) \end{bmatrix}. \quad (40)$$

Given the initial estimation x_0 of the solution of Eq. 39, Newton's method considers the approximation at each iteration [127]:

$$F(x) \approx L_k(x) \equiv F(x_k) + J(x_k)(x - x_k). \quad (41)$$

And computes x_{k+1} as a solution of $L_k(x) = 0$. This solution exists if $J(x_k)$ is non-singular. Therefore, an iteration of Newton's method is described as follows:

$$J(x_k)s_k = -F(x_k), \quad (42)$$

$$x_{k+1} = x_k + s_k. \quad (43)$$

At each iteration of Newton's method, Jacobian $J(x_k)$ was computed, and linear system was solved [127]. In this work, Eq. 42 was solved by using PARDISO solver, which was well documented in the literature [128]. The Newton's algorithm is presented below.

Algorithm 1. Newton's method for non-linear equation [129]

- 1: Choose a starting guess x^0 and accuracy ϵ .
- 2: **for** $k = 0, 1, 2, \dots$ **do**
- 3: compute the correction s_k . Solve $J(x_k)s_k = -F(x_k)$ by the direct solver.
- 4: update the solution guess $x_{k+1} = x_k + s_k$.
- 5: **if** $|s_k| < \epsilon$ **then**
- 6: stop.
- 7: **end if**
- 8: **end for**

Note. For highly non-linear problems, there can be used a damped update of the form $x_{k+1} = x_k + \alpha s_k$ with $0 < \alpha < 1$, where α is a damping parameter.

2.5. The numerical modeling of measurement of water-vapor resistance

In order to understand the effect of water-vapor resistance R_{et} on the comfort rating system better, the obtained R_{et} values are ranked into categories. The water-vapor resistance of clothing layers is classified into three categories, according to the European Standard EN 343:1996 (clothing for protection against foul weather). Impermeable materials are considered in the first category with R_{et} values greater than $150 \text{ m}^2\text{PaW}^{-1}$. It does not provide a perceivable comfort to the wearer. In the second category, the materials are rated as a medium-performance material with R_{et} values between 20 and $150 \text{ m}^2\text{PaW}^{-1}$ and provide a breathable performance. In the third category, the R_{et} values are less than $20 \text{ m}^2\text{PaW}^{-1}$ and have the best performance in terms of 'breathability' [130]. The European Standard EN 343:1996 was superseded

by the European Standard EN 343:2003, which changed the lower threshold for R_{et} of materials from R_{et} 150 $\text{m}^2\text{PaW}^{-1}$ to 40 $\text{m}^2\text{PaW}^{-1}$ in the second category [131]. According to the European Standard EN 343:2003, water-vapor permeability is tested by measuring the resistance to water vapor R_{et} . The lower R_{et} indicates the higher water-vapor permeability (breathability) of the material. According to [132], the Hohenstein Institute (Germany) extended R_{et} measure method to R_{et} comfort rating system (see Table 2.4.).

Table 2.4. R_{et} comfort rating system [132]

Rating	R_{et} value	Description
Very good	0–6	Extremely breathable and comfortable at a higher level of activity.
Good	7–13	Very breathable and comfortable at a moderate rate of activity.
Satisfactory	14–20	Breathable, but uncomfortable at a higher rate of activity.
Unsatisfactory	21–30	Slight breathable, giving moderate comfort at a low rate of activity.
Very unsatisfactory	31+	Not breathable and uncomfortable with a short tolerance time.

In order to predict the water-vapor resistance R_{et} coefficient of a material, there were used density and dynamic viscosity of water-vapor at temperature $T = 35$ °C and relative humidity $RH = 40$ %. The moist air properties were obtained, according to the ideal gas law that is well explained by [133]. The experimental values of R_{et} can be determined following Eq. 2. The relation between relative humidity and vapor-partial pressure follows Eq. 44 and Eq. 45 [134].

$$RH = \frac{p_v}{p_{sat}(T)} \cdot 100\% = \varphi \cdot 100 \%, \quad (44)$$

$$p_{sat}(T) = 610.7[\text{Pa}] \cdot 10^{7.5 \frac{T-273.15[\text{K}]}{T-35.85[\text{K}]}}. \quad (45)$$

From Eq. 44 and Eq. 45, it can be obtained that $p_v = 2,248.5$ Pa and $p_{sat} = 5,621.3$ Pa. These parameters are constant. According to [135], the local permeability can be neglected due to the high-pressure compression. During the water-vapor resistance test, the fluid velocity is fixed. With different samples, the pressure drop across the fabric changes. For this reason, during numerical simulations of the water-vapor resistance test, the local (intra-yarn) permeability was ignored. The assumptions of the model that allows evaluating water-vapor resistance coefficient:

- Stationary isothermal flow (it means that there are no temperature and RH changes). Besides, an incompressible flow indicates constant mass density.
- Single-phase flow.
- Low Re number.
- Newtonian fluid (constant dynamic viscosity).

The simulations were performed by using *Laminar Flow (.spf)* and *Moisture Transport in Air (.mt)* interfaces. *Moisture Transport in Air* interface allows determining moist air properties (density and dynamic viscosity) that are used in the *Laminar Flow* interface. It should be noted that fluid density and dynamic viscosity can be directly applied to the *Laminar Flow* interface.

The *Laminar flow interface (.spf)* allows solving a set of Navier–Stokes equations (see Eq. 33 and Eq. 34). The governing equations of the *Moist Transport in Air* interface are represented below:

$$M_v \mathbf{u} \cdot \nabla c_v + \nabla \cdot \mathbf{g}_w = G; \quad (46)$$

where $\mathbf{g}_w = -M_v D \nabla c_v$, $c_v = \varphi c_{sat}$. c_{sat} stands for the saturation concentration $c_{sat} = \frac{p_{sat}}{RT}$ [123]. Diffusive moisture flux indicates \mathbf{g}_w in Comsol; it can be defined as *mt.dfluxz*. In this case, it is equal to 0. There, G denotes the moisture source or sink. In this case, $G = 0 \text{ kg}/(\text{m}^3 \cdot \text{s})$. Only the convective moisture transport occurs and is expressed as *mt.cfluxz*. There has been used diluted species formulation, which means that the spatial changes of the vapor concentration c_v is small to cause significant differences in the moist air density.

The boundary conditions that are applied to the RVE, using both Comsol Multiphysics interfaces, are depicted in Fig. 2.6.

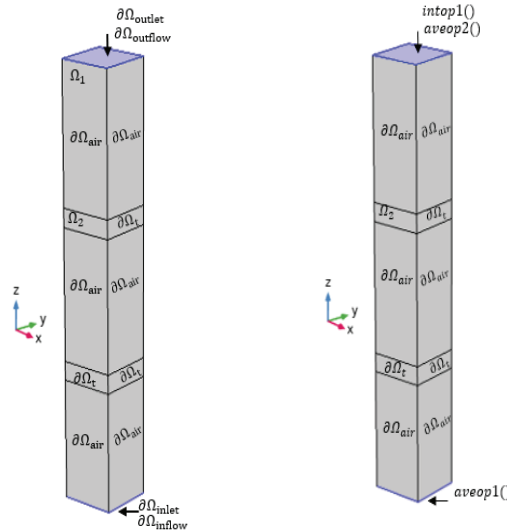


Fig. 2.6. Boundary conditions of 3D textile and positions of operators

Table 2.5. Boundary conditions of R_{et} model

Surface	Boundary conditions	Settings and assumptions
on $\partial\Omega_{inlet}$	$\mathbf{u} = -U_0\mathbf{n}$ $U_0 = 1\text{m/s}$	Inlet (suppress backflow). According to the experiment, the normal inflow velocity is 1 m/s [125].
on $\partial\Omega_{inflow}$	$c_{ustr} = \phi_{w,ustr}c_{sat}(T_{ustr})$ $-\mathbf{n} \cdot \mathbf{g}_w = M_v d_z(c_v - c_{ustr})\mathbf{u} \cdot \mathbf{n}$	Inflow. The upstream temperature and upstream RH are $T_{ustr} = 35\text{ }^\circ\text{C}$ and $\phi_{w,ustr} = 0.4$, respectively. c_{ustr} -upstream vapor concentration. This condition corresponds to the <i>Danckwerts</i> condition [123].
on $\partial\Omega_{outflow}$	$-\mathbf{n} \cdot \mathbf{g}_w = \mathbf{0}$	Outflow. The zero diffusive flux is applied to the outlet boundary.

In order to predict R_{et} , there was made a change in the laminar flow regime. The $\partial\Omega_{inlet}$ boundary condition was changed to the normal inflow velocity condition. No changes were made to the other boundary conditions. In addition, by including a moist air interface, two boundary conditions $\partial\Omega_{inflow}$ and $\partial\Omega_{outflow}$, which represent the moist air flow, according to the experiment, were applied. The boundary conditions that were used in the model are summarized in Table 2.5. and depicted in Fig. 2.6. This finite element model represents a closed system with fixed temperature and relative humidity. However, the R_{et} evaluation is not straightforward. Eq. 2 was recalculated, according to [16]. It was assumed that the heating power H that is required to keep the plate temperature at $T = 35\text{ }^\circ\text{C}$ can be converted to the power of water vapor, which penetrates the textile layer [16]. The water-vapor resistance coefficient can be defined as follows: $R_{et} = \frac{\rho_v}{\delta_p(p_{sat}-p_v)}$ s/m. The water-vapor transmission coefficient is expressed as $\delta_p = \frac{w_v}{A\Delta p}$ s/m. The moist air properties were applied to the laminar flow regime; thus, for the global evaluation, the ρ_v represents moist air density kg/m^3 , w_v is the mass flow rate of water vapor kg/s , Δp is the pressure difference between boundaries $\partial\Omega_{inlet}$ and $\partial\Omega_{outlet}$. Before the simulation, the integration *intop1* and average operators *aveop1*, *aveop2* were created on boundaries as shown in Fig. 2.6.

In the Comsol environment, the global expression to evaluate δ_p can be expressed as follows:

$\text{intop1}(spf.U) \cdot \text{aveop1}(mt.wc_v) / (\text{intop1}(1) \cdot (\text{aveop1}(p) - \text{aveop2}(p)))$ and R_{et} is $\text{aveop1}(mt.rho_moist) / (\text{intop1}(spf.U) \cdot \text{aveop1}(mt.wc_v) / (\text{intop1}(1) \cdot (\text{aveop1}(p) - \text{aveop2}(p))) \cdot (\text{aveop2}(mt.psat) - \text{aveop1}(mt.pv)))$. It should be noted that the units of R_{et} and δ_p are the same $\frac{\text{m}^2\text{Pa}}{W} = \frac{\text{kg/s}}{\text{m}^2\text{Pa}} = \frac{\text{s}}{\text{m}}$.

2.6. The numerical modeling of measurement of thermal resistance

In the solution of heat transfer through solids, the convection heat transfer coefficient usually appears as a boundary condition. The convection can be either natural (or free), forced, or mixed [51]. Natural convection takes place when fluid

motion occurs due to the density variation that is caused by the temperature differences. There is no interference from the external environmental parameters, such as airflow. For instance, in extremely cold climates, clothing assemblies are used to counteract different environmental conditions. Forced convection is when the external force causes fluid motion. One of the most important factors, resulting in forced convection of heat through the clothing assembly, is a wind blowing over the outer surface of the clothing. A mixed convection state has both natural and forced convection [101], [51].

Newton's cooling law gives the heat transfer due to the convection as follows:

$$q = h(T_s - T_a); \quad (47)$$

where q is the convective heat flux, (W/m^2), ($T_s - T_a$) is the temperature difference between the solid wall and the fluid, and h is the convection heat transfer coefficient, (W/m^2K) [51].

On a macro-scale, Shen et al. [136] proposed the torso thermal manikin model that solves the conjugate heat transfer problem. Generally, the conjugate heat transfer model is made up of equations that describe the fluid flow and heat transfer equations. In the developed model, it was assumed that the clothing system is a porous media domain and fluid flow is laminar in that region. The fluid flow in the air (ambient) domain with different velocities was modeled as turbulent flow. The heat transfer process was imitated by the convection, conduction, and radiation. The natural convection was taken into account by modeling buoyant force (Boussinesq approximation) [136]. On a micro-scale, Siddiqui and Sun [97] as well used the conjugate heat transfer approach to predict the effective thermal conductivity and thermal resistance. The model was created to imitate one-plate method.

In this thesis, a numerical model that predicts the thermal resistance coefficient R_{ct} was proposed. Commonly, the thermal resistance is determined from the experimental test. The sweating guarded-hotplate device is a part of two-plate method that allows measuring thermal resistance and effective thermal conductivity. During the experiment, the fabric is placed between hot and cold plates [137]. According to Siddiqui [137], the heat convection can be neglected when the fabric is placed between the two plates with a temperature gradient, and the radiation mode can be ignored due to a small temperature gradient. The thermal resistance coefficient can be used to estimate the heat transfer coefficient h , $W \cdot m^2/K$. The heat transfer coefficient h , $W \cdot m^2/K$ is inverse to the thermal resistance coefficient R_{ct} [138].

The simulations of thermal resistance coefficient R_{ct} can be performed in Comsol software by using *Heat transfer in solids and fluids(ht)* interface. The governing equations of the model are based on the energy conservation (heat transfer equation, see Eq. 48), where C_p stands for specific heat capacity in [$J/kg K$], Q is the overall heat transfer in [W], $\mathbf{q} = -k\nabla T$, where k denotes the thermal conductivity of the fluid-solid mixture in [$W/m \cdot K$] [123].

$$\rho C_p \mathbf{u} \cdot \nabla T + \nabla \cdot \mathbf{q} = Q. \quad (48)$$

The assumptions of the model that allows evaluating thermal resistance:

- Stationary non-isothermal flow (it means that there are temperature changes).
- The heat was transferred due to conduction (it was stated that convection and radiation can be ignored).
- The fluid matrix was treated as dry air/moist air.

The boundary conditions of thermal resistance are summarized in Table 2.6. Two temperature boundaries were applied on $\partial\Omega_{inlet}$ and $\partial\Omega_{outlet}$. The thermal insulation boundary was left as default on other surfaces. The model geometry of dry air/moist air had been changed concerning textile thickness. The model's geometry with boundary conditions is depicted in Fig. 2.7. Furthermore, Fig. 2.7. depicts the mesh of *Model 1_a* that consists of 40,326 elements.

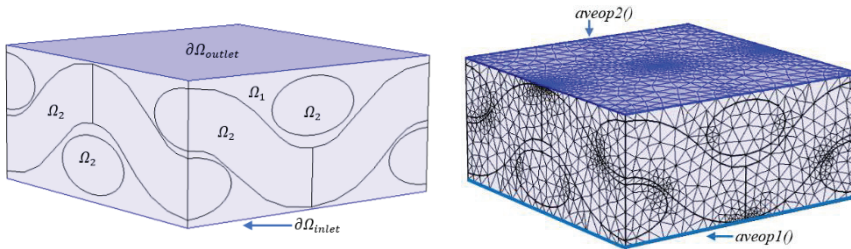


Fig. 2.7. Boundary conditions of one-layer textile, positions of operators and mesh

Table 2.6. Boundary conditions of R_{ct} model

Surface	Boundary conditions	Settings and assumptions
on $\partial\Omega_{inlet}$	$T = 35\text{ }^{\circ}\text{C}$	Temperature. The constant temperature $T = 35\text{ }^{\circ}\text{C}$ was applied on $\partial\Omega_{inlet}$ surface, which represents skin.
on $\partial\Omega_{outlet}$	$T = 20\text{ }^{\circ}\text{C}$	Temperature. The constant temperature $T = 20\text{ }^{\circ}\text{C}$ was applied on $\partial\Omega_{outlet}$ surface.

The numerical simulation of the thermal resistance coefficient R_{ct} was developed by using different material properties. The solid matrix properties are shown in Table 2.7. The thermal conductivity can be represented as a diagonal matrix (tensor). The thermal conductivity along the fiber axis is K_{11} . K_{22} and K_{33} stand for thermal conductivity perpendicular to the fiber axis [137]. In this simulation, the material orientation is not considered. Two cases of the fluid matrix were set. The first simulations were performed by using air as a fluid. However, according to the experiment, the relative humidity is $RH = 65\%$. Thus, the second case was to use a moist air domain instead of a fluid (air) domain. A similar experiment of thermal resistance was measured and numerically predicted by Siddiqui [137].

Table 2.7. Thermal properties of solid matrix [137]

Material properties	Nomex III	Cotton	Polyester (PES)	Polypropylene
ρ , (kg/m ³)	1,380	1,520	1,390	910
K_{11} , (W/m·K)	1.3	2.88	1.26	1.241
$K_{22} = K_{33}$, (W/m·K)	0.13	0.243	0.157	0.111
C_p , (J/kg·K)	1,200	1,350	1,030	1,680

2.7. Concluding remarks

The mathematical models of textile fabrics have been presented in micro-scale for the representative volume element (RVE). The RVE is the smallest volume of the fabric, which fully represents the geometrical arrangement of the internal structure of the fabric. Depending on the physical process under the investigation, the appropriate models of physical behavior have been constructed, using the finite element discretization of the RVE geometry.

1. In fact, 15 different geometrical configurations of RVE's were investigated to numerically simulate the air permeability (AP) coefficient, water-vapor resistance (R_{et}) coefficient, and thermal resistance (R_{ct}) coefficient's experimental tests. Three models represent a simplified 3D textile structure. The RVE was designed according to the experimental data that is presented in literature.

2. The value of the air permeability (AP) coefficient can be determined by using the model based on Navier–Stokes equations in the free flow domain and Brinkman equations in the porous media domain of the RVE. In this case, the pressure is constant. The local permeability tensor that requires Brinkman equations may be determined according to the analytical Gebart's model.

3. The water-vapor resistance coefficient (R_{et}) and water-vapor transmission coefficient (δ_p) can be determined by solving Navier–Stokes equations in the free flow domain. The local permeability can be neglected due to the high-pressure compression. The moist air properties are applied instead of the dry air. In this case, the inlet velocity is 1 m/s, and it is applied as a boundary condition on $\partial\Omega_{inlet}$.

4. The thermal resistance (R_{ct}) coefficient can be determined by solving the heat transfer equation in the computational domain. The fluid velocity is constant.

5. The skewness measure was used to determine the quality of the mesh. In this work, the minimum element quality is more than 0.01.

3. NUMERICAL EXPERIMENTS

3.1. Verification and validation of air permeability coefficient

In order to demonstrate the validation of the proposed methodology, the simplified case of the used finite element model and the analytical model results on a micro-scale were compared. Gebart's [81] analytical model was used to determine the local permeability coefficient. The transverse local permeability was obtained according to Eq. 15. The case of the hexagonal arrangement (see Fig. 1.10.) of the fibers was investigated. The Gebart's analytical model is valid for porosities, varying from 0.10 to 0.65 [139], [81]. In subsection 2.4., a 3D finite element model was

presented with a set of Navier–Stokes and Brinkman equations in subdomains Ω_1, Ω_2 (see Eq. 33, Eq. 34, Eq. 37). In this case, there has been presented a simplified 2D finite element model with assumptions that fibers are impermeable, the Reynolds number is low ($Re \ll 1$), there are no external forces, no inertia effect. The Navier–Stokes momentum and mass conservation equations (see Eq. 33, Eq. 34) are reduced to the set of Stokes equations (see Eq. 49) [92].

$$\begin{aligned} \nabla \cdot [-p\mathbf{I} + \mu(\nabla\mathbf{u} + (\nabla\mathbf{u})^T)] &= 0 \quad \text{in } \Omega_s, \\ \nabla \cdot \mathbf{u} &= 0 \end{aligned} \quad (49)$$

The boundary conditions of Stokes (or known as creeping) flow are depicted in Fig. 3.1. a). The fluid properties were selected according to the literature [81], [92], [139]. The local permeability coefficient was determined by applying Darcy’s law (see Eq. 31). The numerical and analytical results of normalized local permeability are depicted in Fig. 3.1. b).

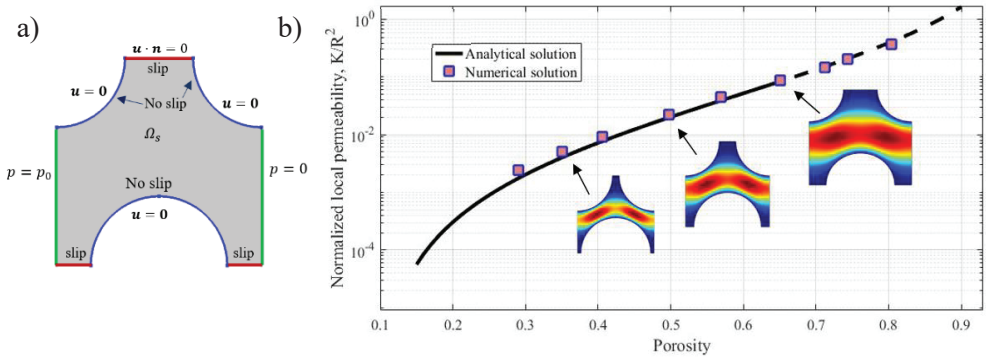


Fig. 3.1. RVE with boundary conditions a) and normalized local permeability, which was obtained with Gebart's analytical model and the proposed finite element model b)

The results demonstrate (see Fig. 3.1. b)) a good agreement between the analytical solution and simplified case of the proposed model on a micro-scale. The relative error was approximately 4 %. The convergence plot is depicted in Fig. 3.2. In all cases, the solution error is 10^{-15} , considering a different number of mesh elements.

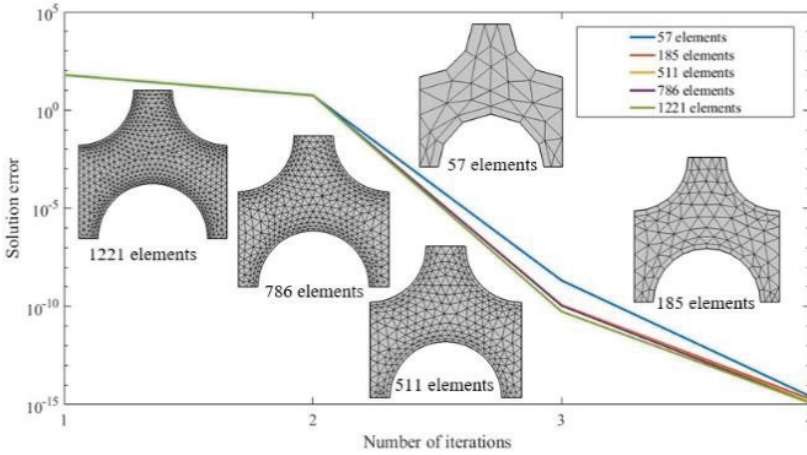


Fig. 3.2. A convergence study between solution error and the number of iterations, considering a different number of mesh elements

In addition, the proposed finite element model in subsection 2.4. in the mesh size analysis is presented below. The mesh size should be taken into consideration for simulating the air permeability (AP) test. One of the reasons is to find an optimal mesh size that is acceptable, considering the computation time and accuracy. In all simulations, the minimum element quality was greater than 0.01. The relative error between the numerical solution and experimental air permeability (AP) coefficient was estimated.

For the convergence study, *Model 1_c*, which represents one layer of simplified geometry of 22/15 sample, was investigated. The geometry of the RVE was fixed, and the total number of mesh elements was increased from 3,194 to 125,512 (see Table 3.1.). Fig. 3.3. depicts the convergence of the AP coefficients with increasing mesh size. The green dotted line and the area represent the experimental values of the average AP and standard deviation of AP (in this case 8.2 %). The squares indicate the average AP that was obtained from the numerical simulations. The relative error, considering experimental data, is less than 5 %, using coarser mesh (see Table 3.1.). This relative error reduces to 0.25 % and 0.16 %, using coarse and normal mesh, respectively. In terms of computation time, the normal mesh can be considered quite costly. The total number of elements and number of degrees of freedom (DOF) will increase by using more complex geometry, consisting of two layers, or use the geometry that has sharp edges and narrow regions that requires higher computational resources. The optimal mesh size, taking into account the computational time and accuracy, is between the coarser and coarse mesh that consists of 18,270 and 57,795 elements. In this thesis, for further simulations, the coarse mesh was used for the approximated geometry domain and coarser mesh for close to the real geometry.

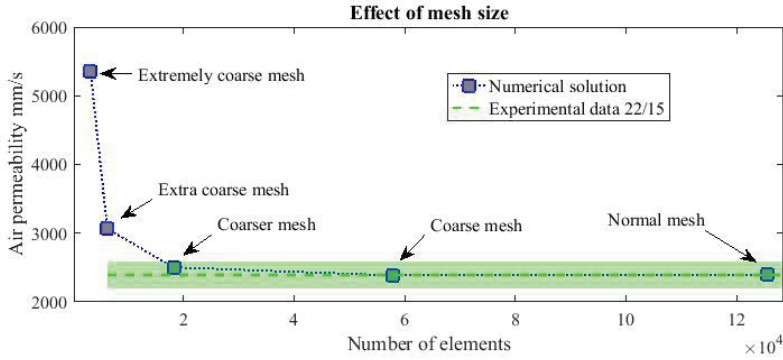


Fig. 3.3. The effect of mesh size and air permeability (AP) coefficient

Table 3.1. Convergence study of *Model 1_c*

Mesh	Total number of elements/DOF	Computation time, s	AP, mm/s	Error, %
Extremely coarse	3,194/3,304	4	5,358.4	124.05
Extra coarse	6,249/5,980	4	3,061.9	28.02
Coarser	18,270/15,744	9	2,503.1	4.66
Coarse	57,795/46,596	24	2,385.6	0.25
Normal	125,512/96,432	111	2,395.6	0.16

Furthermore, the effect of the RVE domain size of *Model 1_a* was investigated. Different cell size that consists of 1 pore (0.55 x 0.55 mm), 4 pores (1.1 x 1.1 mm), 9 pores (1.65 x 1.65 mm), and 16 pores (2.2 x 2.2 mm) with fixed height (10 mm) are depicted in Fig. 3.4.

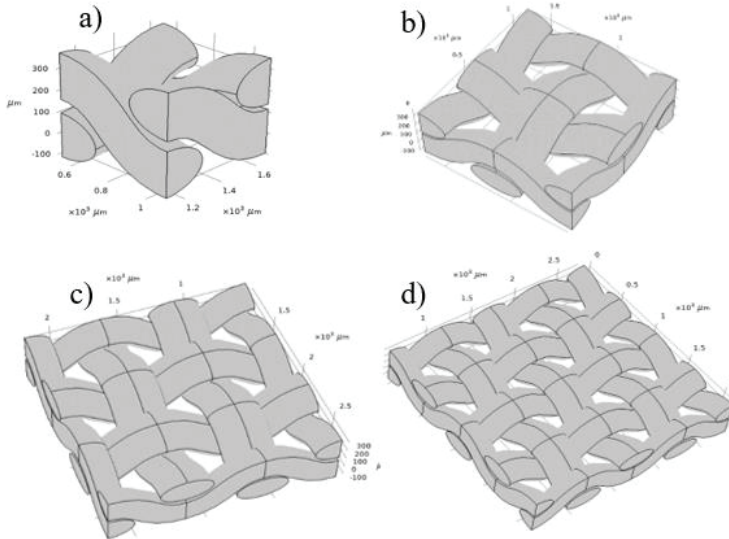


Fig. 3.4. The effect of different domain sizes of *Model 1_a*: 1 pore, 4 pores, 9 pores, 16 pores, are illustrated by a), b), c), d), respectively

The results of different pore numbers are summarized in Table 3.2. In all cases, the relative error did not exceed 7 %. However, it is important to estimate the mesh size. For this reason, in some cases, different mesh size was automatically generated. The precise results were obtained by avoiding the minimum element quality less than 0.01. It has been found that there is no difference between the pore numbers. In the case study of 1 pore using coarser mesh, 4 pores using coarser mesh, 9 pores using coarse mesh, and 16 pores using normal mesh, the relative errors are less than 1 %. The simulation results of 4 pores are described in Appendix 1. In this study, a textile domain size was selected that consists of 4 pores. It was done to create a simplified 3D textile domain, taking into consideration a spacer yarn. However, a larger domain size of 1.5 and 2 times (representing 9 and 16 pores, respectively) requires more computation time than the 4 pores domain.

Table 3.2. Air permeability test results of *Model 1_a* when domain size is considered

Pore	Mesh	Total number of elements/DOF	Min element quality	Average element quality	Computation time, s	AP, mm/s	Error, %
1	Extra coarse	8,605/ 8,508	0.1269	0.6221	6	2,332.0	2.495
1	Coarser	19,707/ 17,612	0.1078	0.6437	10	2,392.5	0.035
4	Coarser	39,397/ 31,984	0.1006	0.6484	23	2,399.3	0.319
9	Coarser	52,582/ 42,184	0.1033	0.6434	26	2,479.4	3.668
9	Coarse	110,294/ 86,000	0.1165	0.6545	49	2,393.0	0.056
16	Coarse	124,889/ 95,468	0.0944	0.6523	50	2,546.5	6.474
16	Normal	231,887/ 175,900	0.0951	0.6605	213	2,407.2	0.649

Fig. 3.5 . a) illustrates an example of the velocity field of *Model 1_a*, which has 16 pores. Furthermore, the element quality distribution and mesh element size distribution (the length of the longest edge of the element [123]) are depicted in b) and c). The mesh of the air domain consists of 158,951 elements with minimum element quality of 0.171 and the average element quality of 0.670; the textile domain consists of 72,936 elements with the minimum element quality 0.0951 and the average element quality of 0.6399. The skewness quality measure was used to determine the quality of the elements. The average AP on the outlet boundary was obtained 2,407.2 mm/s.

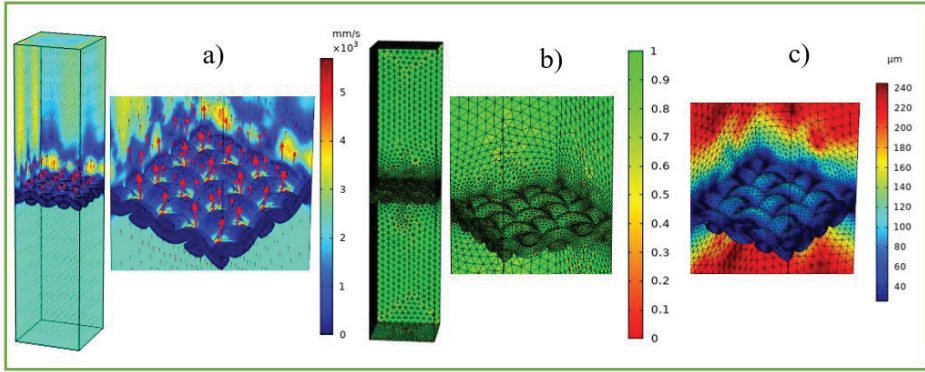


Fig. 3.5. RVE of 16 pores of *Model 1_a*: the air flow distribution is depicted in a), the mesh quality in b), the element size in c)

Table 3.3. Numerical air permeability (AP) coefficients

Model	Description of geometry	AP, mm/s	Error, %
<i>Model 1_a</i>	1 layer / structural density 22/15	2,399.3	0.319
<i>Model 2_a</i>	1 layer / structural density 22/20	1,645.6	4.7039
<i>Model 3_a</i>	1 layer / structural density 29.3/15	1,363.8	7.5272
<i>Model 1_b</i>	2 layer / structural density 22/15	1,484.5	-
<i>Model 2_b</i>	2 layer / structural density 22/20	972.34	-
<i>Model 3_b</i>	2 layer / structural density 29.3/15	778.21	-
<i>Model 1_c</i>	Simplified 1 layer / structural density 22/15	2,385.6	0.2538
<i>Model 2_c</i>	Simplified 1 layer / structural density 22/20	1,613.6	2.6679
<i>Model 3_c</i>	Simplified 1 layer / structural density 29.3/15	1,220.3	3.7869
<i>Model 1_d</i>	Simplified 2 layer / structural density 22/15	1,533.8	-
<i>Model 2_d</i>	Simplified 2 layer / structural density 22/20	974.14	-
<i>Model 3_d</i>	Simplified 2 layer / structural density 29.3/15	706.71	-
<i>Model 1_e</i>	3D textile model based on <i>Model 1_d</i>	1,522.4	-
<i>Model 2_e</i>	3D textile model based on <i>Model 2_d</i>	948.83	-
<i>Model 3_e</i>	3D textile model based on <i>Model 3_d</i>	701.49	-

The results of all air permeability tests are summarized in Table 3.3. The relative error was not over 7.53 % when close to the real one-layer model (*Model 1_a*, *Model 2_a*, and *Model 3_a*) was used. In simplified one-layer models (*Model 1_c*, *Model 2_c*, and *Model 3_c*), the relative error was obtained less than 3.79 %. These findings demonstrate a good agreement with the experimental data. The two-layer air permeability coefficient has been evaluated by numerical experiments as well. As expected, the air permeability values were lower than one layer. Considering the same pressure difference, the AP coefficient decreases as the number of layers increases due to the increasing airflow resistance through the pores in the layers of the textile. The flow resistance is influenced by the alignment of pores in one layer with that of another layer, the air gap between each layer of the textile and the distortion of the

yarn caused by the airflow [140]. According to [140], the AP coefficient of an N-layer system can be determined by the following expression:

$$AP_N = \frac{AP_1}{N^{0.86}}. \quad (50)$$

This expression is valid, considering the same textile materials. The AP_1 represents the air permeability through one layer, N-number of layers.

Table 3.4. represents a two-layer system, where AP is two-layer air permeability values that were obtained numerically, considering close to real geometry and simplified geometry. AP_2 was evaluated according to Eq. 50, taking numerical AP_1 values from Table 3.3. Error1 indicates a relative error between AP_2 and AP. Moreover, the AP_2 value can be predicted from the experimental data (see Table 2.1.). It was 1,317.70 mm/s, 865.92 mm/s, and 698.79 mm/s, respectively to the sample 22/15, 22/20, and 29.3/15. Error2 indicates a relative error between AP_2 , which was obtained from the experimental data and the AP.

Table 3.4. Numerical air permeability (AP) coefficients of two-layer structures

Model	AP, mm/s	AP_2 , mm/s	Error1, %	Error2, %
Model 1 b	1,484.50	1,321.90	12.3	12.66
Model 2 b	972.34	906.65	7.25	12.29
Model 3 b	778.21	751.39	3.57	11.37
Model 1 d	1,533.80	1,314.35	16.70	16.40
Model 2 d	974.14	889.02	9.57	12.50
Model 3 d	706.71	672.33	5.11	1.13

For all cases, Error1 varies from 3.57 to 16.70 % and Error2 from 1.13 to 16.40 %. The main reason for relative errors can be due to the different geometrical parameters. The air gap between layers, the alignment of pores in each layer are unknown. Moreover, Eq. 50 was based on the regression analysis, in which regression coefficients are determined from a limited number of constructions and layers [140]. These relative errors could be acceptable, while demonstrating a good accuracy, which varies from 83.30 to 98.87 %.

The effect of spacer yarn represents *Model 1_e*, *Model 2_e*, and *Model 3_e* (see Table 3.3.). By adding the spacer yarn, the AP values decrease from 1,533.80 to 1,522.40 mm/s, from 974.14 to 948.83 mm/s, and from 706.71 to 701.49 mm/s, respectively to *Model 1_e*, *Model 2_e*, and *Model 3_e*. This means that the resistance to air flow increases by adding a spacer yarn. The example of velocity field through the height of a *Model 2_e* is demonstrated in Fig. 3.6. The average velocity flow through the 3D textile models are illustrated in Fig. 3.7.

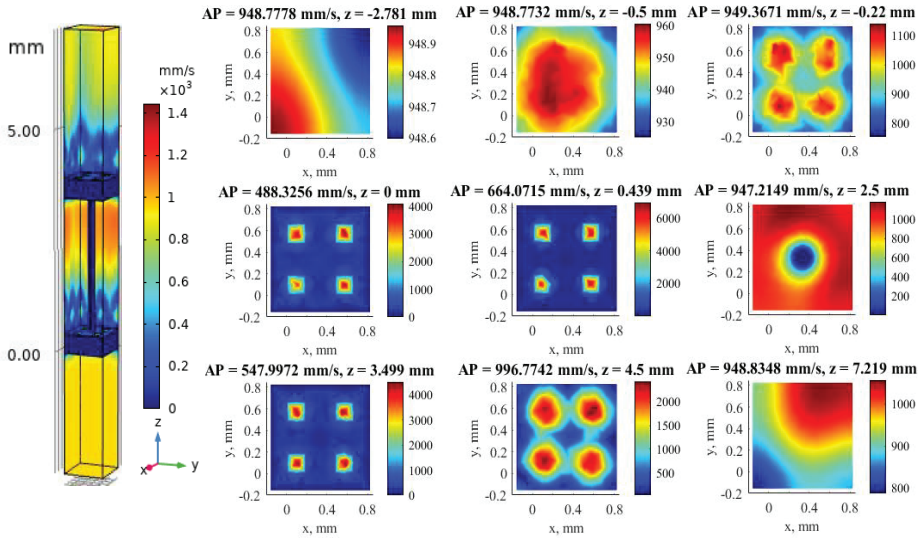


Fig. 3.6. The air velocity distribution of *Model 2_e*

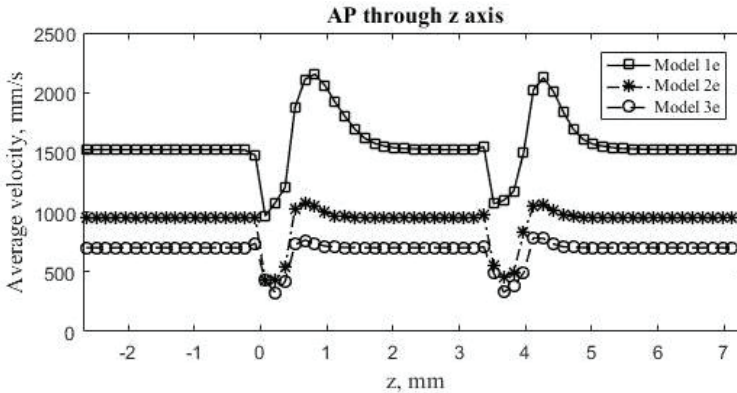


Fig. 3.7. The AP coefficients through-thickness of 3D textile models

More specifically, when CFD tools are used to simulate the air flow through the textile, the air permeability (velocity) is determined by solving Navier–Stokes/Brinkman equations that require the fluid properties dynamic viscosity, density, which is constant, considering that there are no temperature changes. Moreover, the AP simulation result is impacted by the pressure drop, geometrical

parameters, including the porosity and permeability. However, the material properties of the textile domain do not have an influence. The AP and thermal behavior experimental tests of the 3D textile that are made from 3D PES knit with different bioceramic additives were performed by [138], where the pressure drop was set at 100 Pa. The experimental AP values vary from 414 to 641 mm/s. The thickness of samples varies from 2.6 to 2.7 mm. In the used simulation, it has been found that by changing the pressure drop from 200 to 100 Pa, AP values decreased to 982.47 mm/s, 562.67 mm/s, and 403.71 mm/s, respectively to *Model 1_e*, *Model 2_e*, and *Model 3_e*. This demonstrates that *Model 2_e* and *Model 3_e* can be compared as representative models.

3.2. Verification and validation of water-vapor resistance coefficient

The numerical simulation of R_{et} and δ_p are presented in Table 3.5. It was obtained that R_{et} coefficient increases with the number of layers. The R_{et} coefficients are lower in simplified geometry models due to the approximation. All models demonstrate that R_{et} coefficients are highly dependent on the internal geometry. The lowest R_{et} coefficients were obtained in these models where AP was higher. The lowest R_{et} coefficients were estimated in a sample with a structural density of 22/15.

The R_{et} coefficients of one-layer structures are in the range of 1.3105–3.5904 s/m and 0.80729–3.4658 s/m, respectively to close to the real and simplified geometry. The experimental values of the R_{et} of one-layer woven textile were obtained in reference [141], where it varies from 1.6067 to 3.1477 s/m. Analyzing two-layer models *Model 1_b* and *Model 1_d*, R_{et} , the values are 2.6309 s/m and 1.6443 s/m, respectively. Considering the comfort rating system proposed by the Hohenstein Institute (see Table 2.4.), the structure can be rated as very good (extremely breathable and comfortable). *Model 2_b* and *Model 2_d* R_{et} coefficients are 6.4468 s/m and 4.0220 s/m, respectively. These models belong to very good and good breathable classes. *Model 3_b* and *Model 3_d* R_{et} values are 7.1580 s/m and 6.9473 s/m, respectively. These models can be considered as good, breathable. The 3D textile R_{et} coefficients vary from 1.6368–6.9149 s/m. However, 3D textile models are built from simplified geometry models (*Model 1_c*, *Model 2_c*, *Model 3_c*) that have a rough approximation, which is the reason why the errors occur. The experimental value of 3D textile was presented in literature [16] where $R_{et} = 6.36$ s/m. *Model 3_e* demonstrates a good agreement with experimental data from the literature. Besides, two-layer models, such as *Model 2_b*, *Model 3_b*, and *Model 3_d*, can be considered acceptable for further investigation.

The cause of the differences between close to real geometry and simplified is that near such a rough surface, certain amounts of the fluid are trapped and temporarily immobilized [125]. The obtained differences of simulated pressure values in models (close to real and simplified geometry models) demonstrate the necessity to be very careful when using simplified models and establishing their effective geometrical parameters [125].

Table 3.5. Numerically predicted water-vapor resistance R_{et} coefficient

Model	Layer/ structural density	Pressure, Pa	Water-vapor transmission, δ_p , s/m	Water-vapor resistance, R_{et} , s/m
Model 1 a	1/22/15	61.423	2.5723E-4	1.3105
Model 2 a	1/22/20	151.48	1.0429E-4	3.2324
Model 3 a	1/29.3/15	168.34	9.3893E-5	3.5904
Model 1 b	2/22/15	120.26	1.2814E-4	2.6309
Model 2 b	2/22/20	302.21	5.2291E-5	6.4468
Model 3 b	2/29.3/15	336.24	4.7096E-5	7.1580
Model 1 c	Simplified 1/22/15	37.829	4.1759E-4	0.80729
Model 2 c	Simplified 1/22/20	94.366	1.6740E-4	2.0138
Model 3 c	Simplified 1/29.3/15	162.41	9.7268E-4	3.4658
Model 1 d	Simplified 2/22/15	77.053	2.0501E-4	1.6443
Model 2 d	Simplified 2/22/20	188.47	8.3817E-5	4.0220
Model 3 d	Simplified 2/29.3/15	325.56	4.8524E-5	6.9473
Model 1 e	3D textile	76.761	2.0595E-4	1.6368
Model 2 e	3D textile	187.43	8.4318E-5	3.9981
Model 3 e	3D textile	324.03	4.8752E-5	6.9149

3.3. Verification and validation of thermal resistance coefficient

The thermal resistance test was performed according to subsection 2.6. A similar experiment of woven structures was performed by Siddiqui [137]. The main results of measurements and predicted values are summarized in Table 3.6.

Table 3.6. Predicted and measured R_{ct} and K_{eff} [137]

Fabric	Experimental R_{ct} , $K \cdot m^2/W$	Experimental K_{eff} , $W/(m \cdot K)$	Predicted R_{ct} , $K \cdot m^2/W$	Predicted K_{eff} , $W/(m \cdot K)$
Nomex III	0.010000	0.05000	0.009058	0.0552
Cotton	0.008643	0.056	0.007446	0.065
Poly-viscose	0.007045	0.04840	0.006702	0.05088
F3-polyester	0.012159	0.04030	-	-
Sample-1 polypropylene	0.014464	0.037335	-	-
Sample-2 polypropylene	0.009683	0.036146	-	-

The experimental thermal resistance coefficient R_{ct} and effective thermal conductivity K_{eff} can be obtained from Eq. 3 and Eq. 4. The numerically predicted R_{ct} and K_{eff} coefficients can be estimated from Eq. 18 and Eq. 17, respectively. In Comsol multiphysics software, the heating power H that is required to maintain the constant temperature (see Eq. 3) can be recalculated differently. The first option is to use an integration operator on $\partial\Omega_{inlet}$ and integrate the heat flux (e.g., $intop1(ht.nflux)$). In this way, the heating power is obtained, and it can be directly used in Eq. 3. The second option is to use Eq. 18 where the average heat flux on $\partial\Omega_{inlet}$ represents the term Q/A . In this thesis, the postprocessing of thermal resistance R_{ct} was done by using Eq. 18.

The global evaluation of Eq. 18 is $(aveop1(T)-aveop2(T))/aveop1(ht.ntflux)$, where $aveop1()$, $aveop2()$ are the average operators on $\partial\Omega_{inlet}$ and $\partial\Omega_{outlet}$ (see Fig. 2.7.). It should be noted that $ht.ntflux$ denotes normal total heat flux W/m^2 that is a sum of components: $ht.ncflux$, $ht.ndflux$, and $ht.rflux$, that represent convective, conductive, and radiative heat fluxes, respectively. In this case, $ht.ntflux=ht.ndflux$ because there was assumed that the heat is transmitted due to the conduction, and other heat transmission modes (convection, radiation) were neglected.

In this study, the numerically predicted thermal resistance R_{ct} and effective thermal conductivity K_{eff} of samples 21/15 and 29.3/15 are summarized in Table 3.7. and Table 3.8. The notation of dry air or moist air indicates what type of fluid was used in the simulation. The solid matrix properties were applied from Table 2.7. The example of temperature distribution and element size distribution is depicted in Fig. 3.8. During the simulations, the fine mesh was applied in all cases. It has been found that in all cases, using moist air properties, the thermal resistance is higher than using dry air. In addition, the effective thermal conductive values were obtained higher by using dry air properties. It is due to the relationship between the thermal resistance and the effective thermal conductivity that follows Eq. 17. The outcomes of literature on thermal resistance are described in Table 3.6., which can be compared to Table 3.7. and Table 3.8. The relative error of effective thermal conductivity between the experimental data [137] and the proposed *Model 1_a* is approximately 2 % (Nomex III), 11 % (Cotton), 29 % (PES), and 24 % (Polypropylene). However, a slight difference between thermal resistance R_{ct} coefficients might be due to the thickness of the fabric or the orientation of the fabric. The thickness effect can be seen in Table 3.7. and Table 3.8. The fabric thickness of *Model 1_a* and *Model 3_a* are 0.439 mm and 0.468 mm, respectively. In thicker samples, the thermal resistance is higher.

Table 3.7. Numerically predicted R_{ct} and K_{eff} values of sample 21/15 (*Model 1_a*)

Sample 21/15 (<i>Model 1_a</i>)	R_{ct} , $K \cdot m^2/W$ (dry air)	K_{eff} , $W/(m \cdot K)$ (dry air)	R_{ct} , $K \cdot m^2/W$ (moist air)	K_{eff} , $W/(m \cdot K)$ (moist air)
Nomex III	0.0089328	0.049145	0.0089585	0.049004
Cotton	0.0070739	0.062059	0.0070969	0.061858
Polyester (PES)	0.0082983	0.052902	0.0083232	0.052744
Polypropylene	0.0095373	0.046030	0.0095639	0.045902

Table 3.8. Numerically predicted R_{ct} and K_{eff} values of sample 29.3/15 (*Model 3_a*)

Sample 29.3/15 (<i>Model 3_a</i>)	R_{ct} , $K \cdot m^2/W$ (dry air)	K_{eff} , $W/(m \cdot K)$ (dry air)	R_{ct} , $K \cdot m^2/W$ (moist air)	K_{eff} , $W/(m \cdot K)$ (moist air)
Nomex III	0.0092219	0.050749	0.0092472	0.050610
Cotton	0.0071805	0.065176	0.0072030	0.064973
Polyester (PES)	0.0085249	0.054898	0.0085493	0.054741
Polypropylene	0.009884	0.047328	0.0099147	0.047203

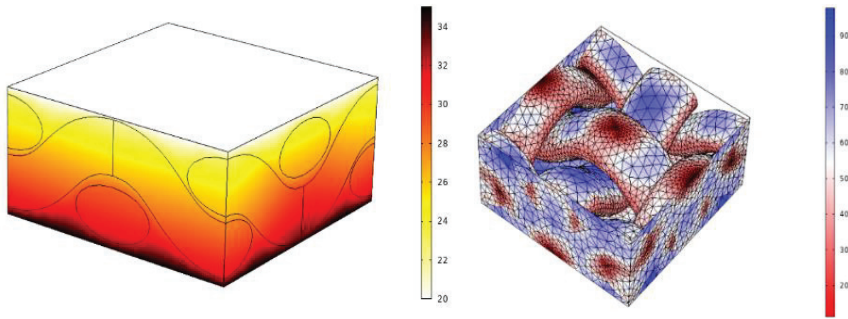


Fig. 3.8. The temperature distribution of *Model 1_a* (solid matrix-polypropylene, fluid matrix-air), and on the right, the element size distribution in μm

Moreover, the numerical experiments of thermal resistance were performed on 3D textile models (*Model 1_e*, *Model 2_e*, and *Model 3_e*), considering that the fluid trapped between solid domain is moist air ($\text{RH} = 65\%$). In this part, polyester (PES) and polypropylene that is widely used in applications of 3D textile were analyzed. The numerical results are summarized in Table 3.9. The effective heat transfer h_{eff} coefficient was obtained as an inverse coefficient to the thermal resistance coefficient. Fig. 3.9. illustrates the temperature distribution in $^{\circ}\text{C}$ and element size distribution in μm of 3D textile (*Model 1_e*).

Table 3.9. Numerically predicted R_{ct} and h_{eff} of 3D textile

Sample	R_{ct} , $\text{K}\cdot\text{m}^2/\text{W}$ polyester (PES)	h_{eff} , $\text{W}/(\text{K}\cdot\text{m}^2)$ polyester (PES)	R_{ct} , $\text{K}\cdot\text{m}^2/\text{W}$ polypropylene	h_{eff} , $\text{W}/(\text{K}\cdot\text{m}^2)$ polypropylene
<i>Model 1_e</i>	0.11419	8.7577	0.11962	8.36
<i>Model 2_e</i>	0.11163	8.9582	0.11758	8.5046
<i>Model 3_e</i>	0.10891	9.1815	0.11592	8.6265

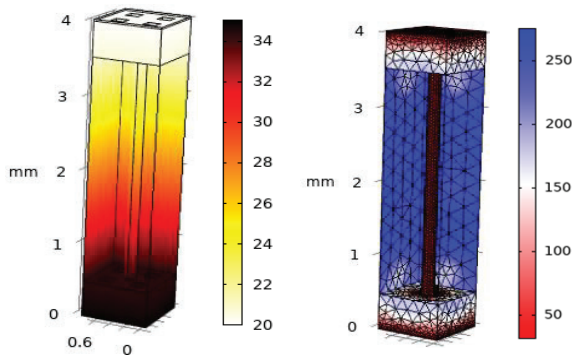


Fig. 3.9. Temperature distribution of *Model 3_e* (solid matrix-polypropylene, fluid matrix-moist air) and distribution of element size, μm

According to the obtained findings, polypropylene has a higher thermal-resistance coefficient than polyester. The heat transfer coefficient of polypropylene varies from 8.36 to 8.63 W/(K·m²), and polyester varies from 8.76 to 9.18 W/(K·m²). These results might be reasonable because in literature [16], the 3D textile measured thermal resistance was 0.118 (K·m²)/W, and the heat transfer coefficient was 8.4746 W/(K·m²). However, the sample thickness was 7.5 mm. In the performed simulations, the height of the spacer was constant 3.06 mm; thus, the heat transfer coefficient slightly increases with the increased thickness. The total height of the samples is about 4 mm. However, it requires analysis on how the spacer yarn height (including different configurations) or air gap between the top and bottom layers affects the thermal resistance coefficient or heat transfer coefficient. Furthermore, it is quite difficult to select properly initial material properties that are used in a solid matrix. One of the reasons is that 3D textile materials can be made from different types of yarn, including bioceramic additives.

3.4. Concluding remarks

The computational models of air permeability, water-vapor resistance, thermal resistance tests that were presented in section 2 have been tested and validated by performing calculations of real fabric RVE structures. It has been found that there is no significant difference between the size of RVE that was selected: 0.55 x 0.55 mm, 1.1 x 1.1 mm, 1.65 x 1.65 mm, and 2.2 x 2.2 mm, considering a different number of pores (empty spaces between yarns). The appropriate finite element mesh refinements have been established by analyzing the convergence of the models. In this work, no physical experiments were performed; therefore, the experimental values that had been published elsewhere in the scientific literature were used for comparison.

The simulation performed for establishing the value of the air permeability coefficient demonstrated a good agreement with the experiment. The relative errors did not exceed 1 % for the sample with a structural density of 22/15, 5 % for the sample with a structural density of 22/20, and 8 % for the sample with a structural density of 29.3/15, considering one-layer structures. The air permeability coefficients of two layers and 3D textile models were predicted. The relative errors of two-layer textile vary from 3.57 % to 16.70 %. The relative errors were due to the unknown air gap between layers, the alignment of pores in each layer. The reason for errors that predicted air permeability coefficient was compared with the empirical formula that was based on regression analysis. From a statistical point of view, there were a limited number of experiments, and the samples had their structural geometry. The proposed 3D textile models (*Model 2_e* and *Model 3_e*) demonstrated a good agreement with the experimental data from the literature.

The water-vapor resistance test revealed that it is extremely sensitive to the changes in geometry. The simplified geometry should be carefully chosen to simulate the water-vapor resistance coefficient. The developed model allows determining the water-vapor transmission and the water-vapor resistance coefficients.

The thermal resistance test was performed, considering that heat is transmitted due to the conduction. The developed model enables the evaluation of thermal resistance, effective conductivity, and heat transfer coefficients. The model was

tested, considering different solid/fluid matrix properties. The thermal resistance of one-layer structures have been compared with measured and predicted data from literature. There was demonstrated a quite good agreement with literature.

The developed models demonstrated a good agreement with experimental data and illustrated the situations where the results were very sensitive to the small changes of RVE geometry. The models can be easily expanded to different geometries, environmental conditions, and more complex functionality of smart textile fabrics.

4. APPLICATION OF MODELS TO INVESTIGATE FABRICS WITH ADDITIONAL FUNCTIONALITY

In section 2 and section 3, there was presented a methodology and numerical investigations of the air permeability (AP), water-vapor resistance (R_{et}), and thermal resistance (R_{ct}) coefficients. The obtained coefficients can be used to determine other thermal comfort properties, like thermal absorptivity, water-vapor permeability, water-vapor permeability index (see subsection 1.1), effective thermal conductivity coefficient, water-vapor transmission coefficient, or effective heat transfer coefficient. In this section, the main intention is to demonstrate the practical applicability of performed investigation. A brief introduction to FEM applications was provided in subsection 1.3. Different aspects of heat and moisture exchange between the skin and textile were analyzed. In this section, there has been developed a numerical model to investigate the effect of forced ventilation through 3D textile. The numerical experiments are presented below.

4.1. The geometry of forced ventilation model

The simulations of heat and moisture exchange due to the forced convection are still interesting and challenging. Several models were developed by Venkataraman et al. [142] where thermal properties of aerogel-coated material were investigated under extreme weather conditions to identify the utility of different materials. The numerical model of the forced-air ventilation cooling system was proposed by Sun and Jasper [143]. The computational model evaluates the local and average convective and evaporative heat transfer coefficients, considering various air velocities and configurations of fans. The numerical model of periodic ventilation of fibrous material was investigated by Ghali et al. [144]. In order to demonstrate the effect of textile motion, a three-node adsorption numerical model was developed. The experimental and numerical investigations of active cooling systems of multi-layer textile packages

were proposed by Barauskas et al. [16], [145]. The basic heat and moisture exchange scheme in the active cooling system is depicted in Fig. 4.1.

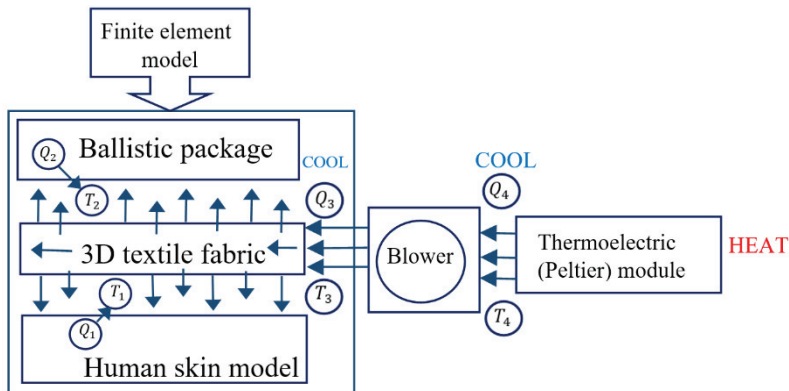


Fig. 4.1. The heat and moisture exchange scheme in the active cooler system [145]

During such simulations, different effects can be investigated, such as insulation properties under different multi-layer packages, the effect of ‘microclimate’ thickness, the effect of air gaps between layers, or even examine the influence of extreme environmental conditions. However, it requires knowledge and understanding of physical phenomena as well as proper selection of material properties, governing equations, and boundary conditions.

In this study, the *Model 3_e* geometry is used as an equivalent to the 3D textile geometry. The ‘microclimate’ thickness was set to 1 mm. The geometry and mesh of the computational domain are depicted in Fig. 4.2. The coarse mesh was set on the computational domain. The total number of elements is 56,513; the minimum element quality is 0.22; the average element quality is 0.66. Lagrange linear discretization was used for the temperature, velocity, and pressure. It was assumed that 3D textile is made from polyester (PES) (see Table 2.7.), and the fluid is moist air (RH = 65 %, T = 20 °C). The temperature of the inlet mass flow (the standard temperature of the ventilation surface) was set to 10 °C.

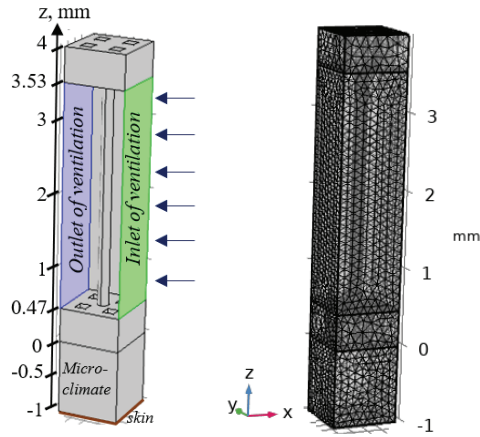


Fig. 4.2. The geometry and mesh of a ventilation model

4.2. The boundary conditions of ventilation model

In this simulation, the governing equations consist of a set of Navier–Stokes (see Eq. 33, Eq. 34) and energy (Eq. 48) equations. It was assumed that the flow is laminar incompressible flow. The boundary conditions that are used in the ventilation model are summarized in Table 4.1.

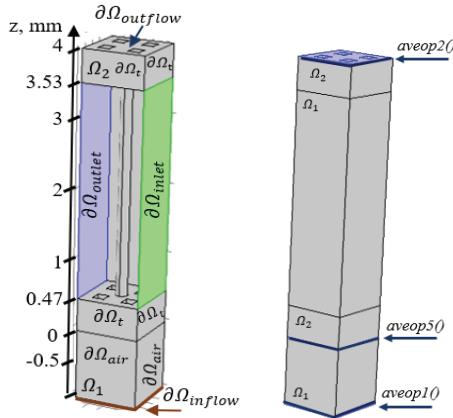


Fig. 4.3. The boundary conditions and average operators of the ventilation model

Table 4.1. Summary of boundary conditions used in the ventilation model

Boundary	Fluid flow (.spf) interface	Description [123]
on $\partial\Omega_{\text{inlet}}$	$-\int_{\partial\Omega} \frac{\rho}{\rho_{st}} (\mathbf{u} \cdot \mathbf{n}) d_{bc} dS = Q_{sv}$ <p>Q_{sv} – standard flow rate, in this study: 0, 0.2, and 0.8 dm³/min. When $Q_{sv} = 0$, it means that there is no ventilation.</p>	Inlet boundary condition was used to apply the mass flow rate . Where d_{bc} stands for the fluid-flow domain boundary thickness, the standard density is defined as $\rho_{st} = \frac{p_{st} \cdot M_n}{R \cdot T_{st}}$. In this study, the standard temperature $T_{st} = 10$ °C, M_n – mean molar mass of the fluid (0.032 kg/mol), R – the universal molar gas constant, and p_s – the standard pressure 1[atm].
on $\partial\Omega_{\text{outlet}}$	$[-p\mathbf{I} + \mathbf{K}]\mathbf{n} = -\hat{p}_0\mathbf{n}$ $\hat{p}_0 \leq p_0, \mathbf{K} = \mu(\nabla\mathbf{u} + (\nabla\mathbf{u})^T)$ $p_0 = 0\text{Pa}$	Outlet on $\partial\Omega_{\text{outlet}}$ is a boundary where the fluid (net) outflows from the domain. The term \hat{p}_0 stands for “suppress backflow”.
on $\partial\Omega_{\text{air}}$	$\mathbf{u} \cdot \mathbf{n} = 0$ $\mathbf{K}_n - (\mathbf{K}_n \cdot \mathbf{n})\mathbf{n} = 0$ $\mathbf{K}_n = \mathbf{K}\mathbf{n}$	Wall on the other boundary (on $\partial\Omega_{\text{air}}$) was used as a default condition. The wall condition slip was applied. It should be noted that textile domain boundaries $\partial\Omega_t$ are not applicable.
Boundary	Heat flow (.ht) interface	
on $\partial\Omega_{\text{inflow}}$	$T = 37$ °C	Temperature. The inlet constant temperature was applied to represent skin temperature.
on $\partial\Omega_{\text{outflow}}$	$-\mathbf{n} \cdot \mathbf{q} = q_0$ $q_0 = h(T_{\text{ext}} - T)$	Heat flux. The h denotes a heat transfer coefficient. The $h = 9.1815$ W/(K·m ²) was selected from Table 3.9. T_{ext} is the external temperature. It was assumed that $T_{\text{ext}} = 20$ °C.
on $\partial\Omega_t, \partial\Omega_{\text{air}}$	$-\mathbf{n} \cdot \mathbf{q} = 0$	Thermal insulation. A zero flux is applied to the external boundaries.

4.3. The analysis of heat and mass exchange through 3D textile

This study demonstrates the effect of a different ventilation rate for the process of force convection via the 3D textile layer. The steady-state temperature distributions through 3D textile, considering the mass flow rate of 0, 0.2, and 0.8 dm³/min, are illustrated in Fig. 4.4, Fig. 4.5, and Fig. 4.6, respectively. The surface average temperature T °C and the position of the cut plane z , mm (x and y positions are fixed), is displayed as the title of each temperature distribution. The ‘microclimate’ can be identified at $z = -0.5$ mm position (the positions of z , mm is shown in Fig. 4.3.). In the center of the ‘microclimate’, when the mass flow rate is 0 dm³/min, the temperature is $T = 35.72$ °C, and with the mass flow rate 0.8 dm³/min, $T = 35.21$ °C, a tendency can be seen that the increased mass flow rate leads to a decrease in temperature. The temperature difference between 0 and 0.8 dm³/min flow rate is approximately 1 °C, at

$z = 1.76$ mm (air gap with space yarn between the top and bottom layers). The temperature is $T = 27.12$ °C (no ventilation), $T = 26.53$ °C ($Q_{sv} = 0.2$ dm³/min), and $T = 26.41$ °C ($Q_{sv} = 0.8$ dm³/min) on $\partial\Omega_{\text{outflow}}$. This as well indicates that the temperature reduces with increased mass flow rate. However, there is a slight difference between the average temperatures through the 3D textile layer, considering the case when there is no ventilation and with a mass flow rate of 0.2 dm³/min.

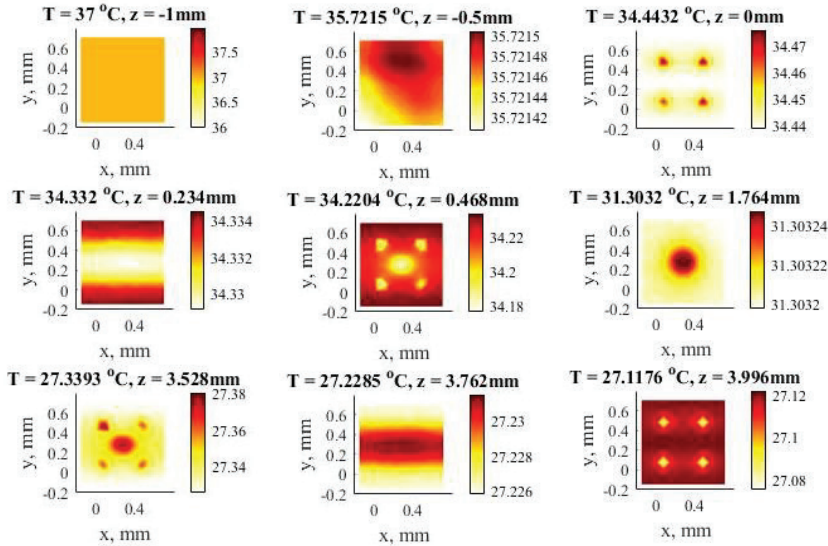


Fig. 4.4. Temperature distribution in case the ventilation rate is zero

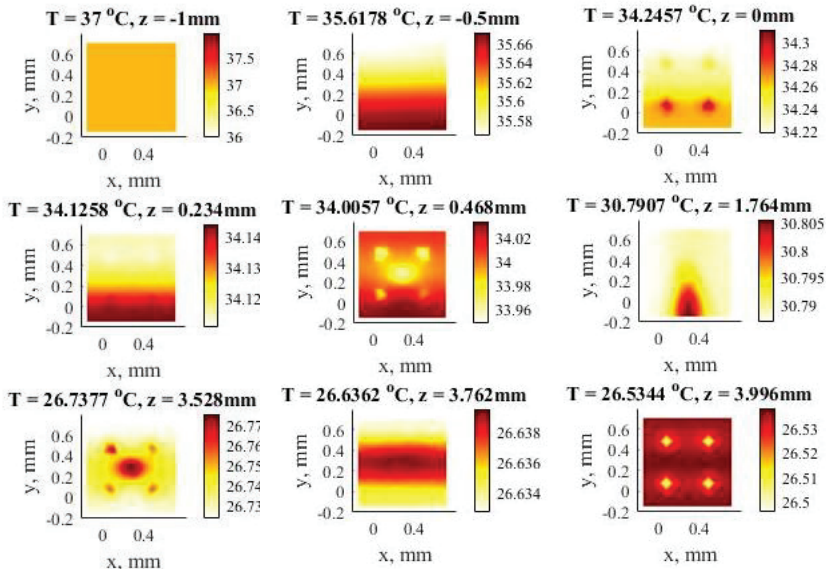


Fig. 4.5. Temperature distribution in case the mass flow rate is 0.2 dm³/min

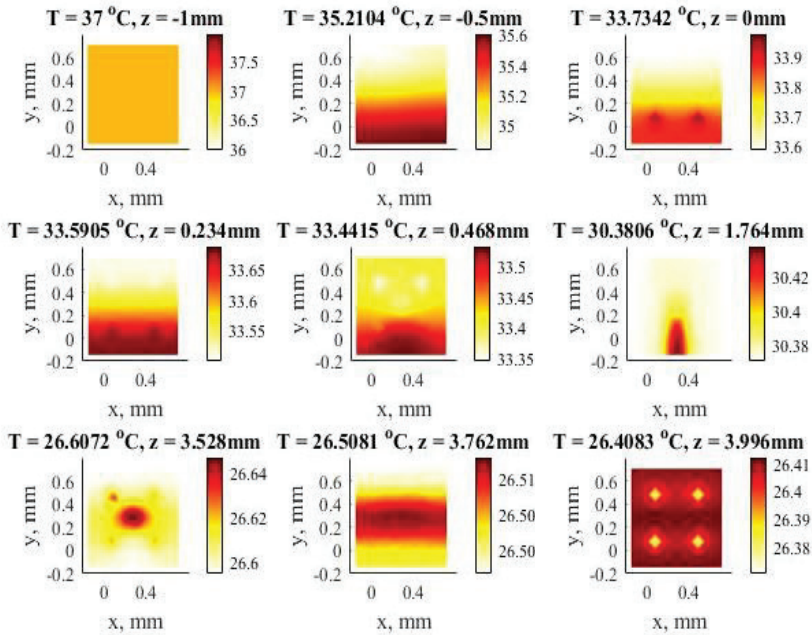


Fig. 4.6. Temperature distribution in case the mass flow rate is $0.8 \text{ dm}^3/\text{min}$

The temperature changes over the time that are depicted in Fig. 4.7. Fig. 4.7. demonstrate the average temperatures of ‘microclimate’ ($z = -0.5 \text{ mm}$ position) and outlet ($z = -3.996 \text{ mm}$ position). In ‘microclimate’, the temperature curves in case of no ventilation rate and $Q_{sv} = 0.2 \text{ dm}^3/\text{min}$ behave similarly. However, in the outlet, there are differences between no ventilation rate and $Q_{sv} = 0.2 \text{ dm}^3/\text{min}$.

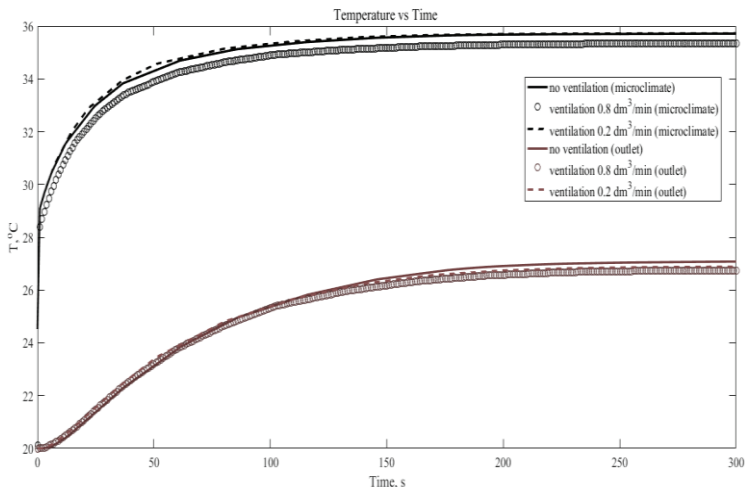


Fig. 4.7. Temperature and time relation, considering different ventilation rates

From this simulation, the heat transfer coefficient (and thermal resistance R_{ct}) can be predicted. In order to evaluate the heat transfer coefficient at different positions of the 3D textile, three average operators ($aveop1()$, $aveop2()$, and $aveop3()$) were used. The positions of operators are illustrated in Fig. 4.3. The summary of effective heat transfer coefficients is described in Table 4.2. The $h_{microlayer}$ indicates convective heat transfer from skin to the air gap (between the skin and the bottom of the textile). It can be evaluated, according to the expression: $aveop1(ht.ntflux)/(aveop1(T)-aveop5(T))$. The h_{inside} stands for the heat transfer coefficient, considering the ventilation layer, and it is obtained by $aveop5(ht.ntflux)/(aveop5(T)-aveop2(T))$. Finally, h_{total} represents the total heat transfer coefficient between skin and the outer layer, and it can be evaluated from the expression: $aveop1(ht.ntflux)/(aveop1(T)-aveop2(T))$. It should be noted that the thermal resistance R_{ct} can be obtained from the expression: $(aveop1(T)-aveop2(T))/aveop1(ht.ntflux)$. In Table 4.2., the *extended* case of simulation is included. Notation *extended* means that the ventilation layer consists of $\partial\Omega_{inlet}$ and boundary of ‘microclimate’. There is a mass flow rate through ‘microclimate’.

It has been found that an increase in the mass flow rate caused the rise of the heat transfer coefficient. However, it means the decrease of thermal resistance. There is a slight difference between the heat transfer coefficients, considering the mass flow rate of 0 dm³/min and 0.2 dm³/min. Taking into account the mass flow rate through ‘microclimate’, the heat transfer coefficient $h_{microlayer}$ decreases in both cases, i.e., (0.2 dm³/min (*extended*) and 0.8 dm³/min (*extended*)). However, the main changes can be seen from the mass flow rate with 0.8 dm³/min and 0.8 dm³/min (*extended*). The mass flow rate through ‘microclimate’ led to the decreased thermal resistance in the ventilation domain. The heat transfer h_{inside} increased from 9.68 to 11.47 W/(K·m²) and from 11.87 to 28.42 W/(K·m²), respectively to the mass flow rate of 0.2 dm³/min and 0.8 dm³/min. Although, there was a slight difference (up to 1 W/(K·m²)), considering h_{total} coefficient.

Table 4.2. Summary of predicted heat transfer coefficient

Mass flow rate	$h_{microlayer}$, W/(K·m ²)	h_{inside} , W/(K·m ²)	h_{total} , W/(K·m ²)
No ventilation (0 dm ³ /min)	25.63	9.51	6.64
0.2 dm ³ /min	25.75	9.68	6.78
0.8 dm ³ /min	29.08	11.87	8.98
0.2 dm ³ /min (<i>extended</i>)	25.59	11.47	7.49
0.8 dm ³ /min (<i>extended</i>)	23.48	28.42	8.65

4.4. Forced ventilation model in macro-scale

In this section, the heat and moisture exchange on a macro-scale with a ventilation layer is presented. The proposed macro-scale model requires an effective heat transfer coefficient, which was obtained from FEA on a micro-scale. This study includes the validation of the numerical results with the experimental data presented in literature [145]. The mathematical model of the heat and moisture exchange in macro-scale is based on literature [16], [145].

The FEM of the ventilation layer consists of three nodes on a macro-scale. The first node is located on the bottom of 3D textile layer, the center node in the middle of 3D textile layer, and the third node on the top of 3D textile layer. The FE equations are based on the balance of incoming and outgoing flow rates and heat fluxes. The first node describes Eq. 51, the center node Eq. 52, and the third node Eq. 53. The general equation in matrix form is presented by Eq. 54 [16]. There, m_{a1}, m_{a0}, m_{a2} denote the masses of air, m_{v1}, m_{v0}, m_{v2} denote the masses of water-vapor, $\tilde{w}_{v1}, \tilde{w}_{v2}, \tilde{w}_{a1}, \tilde{w}_{a2}$ – flow rates of water-vapor and air, w_{a0}^+, w_{v0}^+ – the flow rates of air and water-vapor supplied to the inlet of the 3D ventilation layer, w_{a0}^-, w_{v0}^- – the flow rates of air and water-vapor supplied to the outlet of the 3D ventilation layer, \hat{w}_{v1} stands for the water-vapor mass flow rate generated by the skin, \hat{Q}_1 – heat power produced by the skin, Q_{diff} – diffusive heat flux, $Q_{adv01}, Q_{adv10}, Q_{adv02}, Q_{adv20}$ – convective heat fluxes at both sides of the textile layer [16].

The numerical scheme of the measurement is depicted in Fig. 4.8. During FE simulation, $\tilde{\alpha} = h_{microlayer} = 23.48 \text{ W}/(\text{K}\cdot\text{m}^2)$, $\alpha_{3D} = h_{total} = 8.65 \text{ W}/(\text{K}\cdot\text{m}^2)$ were used (see Table 4.2.). The obtained results are illustrated in Fig. 4.9. The numerical results are compared with the experimental data from the literature [145].

$$\left\{ \begin{array}{l} \tilde{w}_{v1} + \tilde{w}_{v2} + w_{v0}^+ - w_{v0}^- - \dot{m}_{v0} = 0 \\ \tilde{w}_{a1} + \tilde{w}_{a2} - w_{a0}^- - \dot{m}_{a0} = 0 \\ Q_{diff10} + Q_{diff20} + Q_{adv10} + Q_{adv20} - (c_a m_{a0} + c_v m_{v0})\dot{T}_0 + Q_{in} - Q_{out} = 0, \end{array} \right. \quad (51)$$

$$\left\{ \begin{array}{l} w_{v1} - \tilde{w}_{v1} - \dot{m}_{v1} = 0 \\ w_{a1} - \tilde{w}_{a1} - \dot{m}_{a1} = 0 \\ \hat{Q}_1 + c_v \hat{w}_{v1} T_{human} - (c_a m_{a1} + c_v m_{v1})\dot{T}_1 - Q_{diff10} + Q_{diff12} + Q_{adv01} = 0, \end{array} \right. \quad (52)$$

$$\left\{ \begin{array}{l} w_{v2} - \tilde{w}_{v2} - \dot{m}_{v2} = 0 \\ w_{a2} - \tilde{w}_{a2} - \dot{m}_{a2} = 0 \\ Q_2 - (c_a m_{a2} + c_v m_{v2})\dot{T}_2 - Q_{diff20} + Q_{diff12} + Q_{adv20} = 0, \end{array} \right. \quad (53)$$

$$\begin{bmatrix}
m_{a0} & -m_{v0} & 0 & 0 & 0 & 0 & 0 & 0 \\
\frac{1}{\mu_v} & \frac{1}{\mu_a} & \frac{p \cdot h_0 A}{R(T_0)^2} & 0 & 0 & 0 & 0 & 0 \\
-c_v T_0 & -c_a T_0 & c_a m_{a0} + c_v m_{v0} + c_{3D} A & 0 & 0 & 0 & 0 & 0 \\
0 & 0 & 0 & 1 & 0 & 0 & 0 & 0 \\
0 & 0 & 0 & 0 & 1 & 0 & 0 & 0 \\
0 & 0 & 0 & 0 & 0 & c_a m_{a1} + c_v m_{v1} & 0 & 0 \\
0 & 0 & 0 & 0 & 0 & 0 & 1 & 0 \\
0 & 0 & 0 & 0 & 0 & 0 & 0 & 1 \\
0 & 0 & 0 & 0 & 0 & 0 & 0 & c_a m_{a2} + c_v m_{v2}
\end{bmatrix}
\begin{Bmatrix}
\dot{m}_{v0} \\
\dot{m}_{a0} \\
\dot{T}_0 \\
\dot{m}_{v1} \\
\dot{m}_{a1} \\
\dot{T}_1 \\
\dot{m}_{v2} \\
\dot{m}_{a2} \\
\dot{T}_2
\end{Bmatrix}
=
\left\{ \begin{array}{l}
m_{a0} w_{v0}^+ - m_{v0} w_{a0}^+ + m_{a0} \tilde{\delta}_p A (p_{v1} + p_{v2} - 2p_{v0}) - m_{v0} \tilde{k}_a A (p_{a1} + p_{a2} - 2p_{a0}) \\
0 \\
Q_{adv10} + Q_{adv20} - \tilde{\alpha} A (T_1 + T_2 - 2T_0) - (c_v w_{v0}^+ + c_v \tilde{w}_{v1} + c_v \tilde{w}_{v2} + c_a w_{a0}^+ + c_a \tilde{w}_{a1} + c_a \tilde{w}_{a2}) T_0 \\
-\tilde{w}_{v1} \\
-\tilde{w}_{a1} \\
Q_{adv01} - \tilde{\alpha} A (T_1 - T_0) - \alpha_{3D} A (T_1 - T_2) \\
-\tilde{w}_{v2} \\
-\tilde{w}_{a2} \\
Q_{adv02} - \tilde{\alpha} A (T_2 - T_0) + \alpha_{3D} A (T_1 - T_2) \\
0 \\
(c_v w_{v0}^+ + c_a w_{a0}^+) T_\infty \\
\tilde{w}_{v1} \\
0 \\
\hat{Q}_1 + c_v \hat{w}_{v1} T_{human} \\
w_{v2} \\
w_{a2} \\
Q_2
\end{array} \right\} + \quad (54)$$

It has been found that the mean absolute error between the FE model and the experimental values in the 3D textile layer is 1.35 °C. The absolute error over time is illustrated in Fig. 4.10. The main reason for different results might be due to the dispersal of the experimental data. However, there is a quantitative and qualitative similarity between the numerical results and the experiment. The mean absolute error might be acceptable.

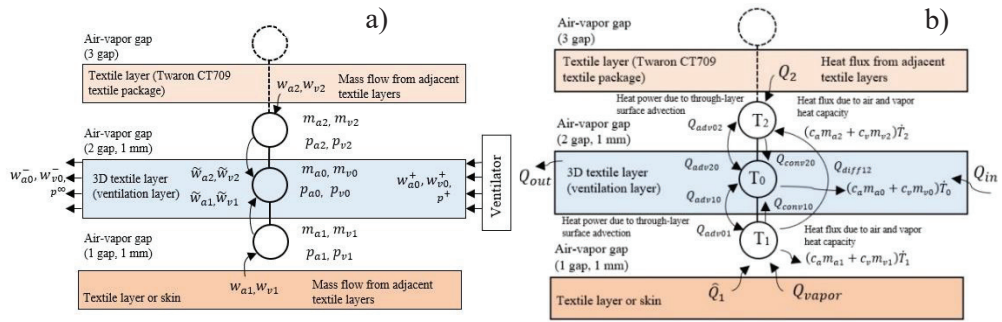


Fig. 4.8. Numerical scheme, the mass flow rates of fluid (a) and heat fluxes (b) [16]

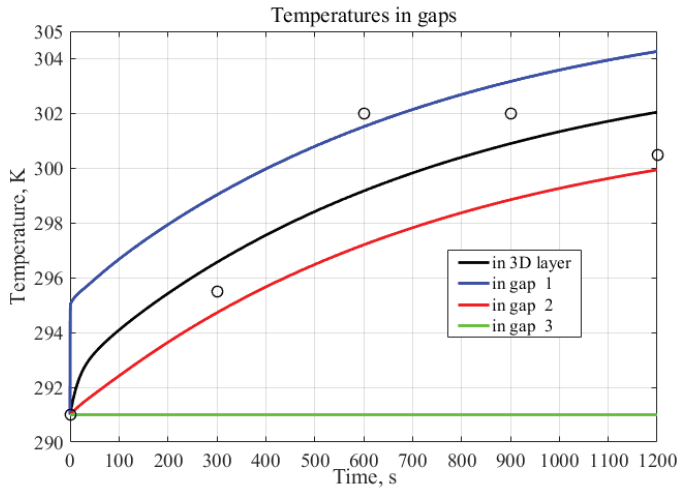


Fig. 4.9. Comparison of numerically predicted and experimental temperatures in 3D textile layer

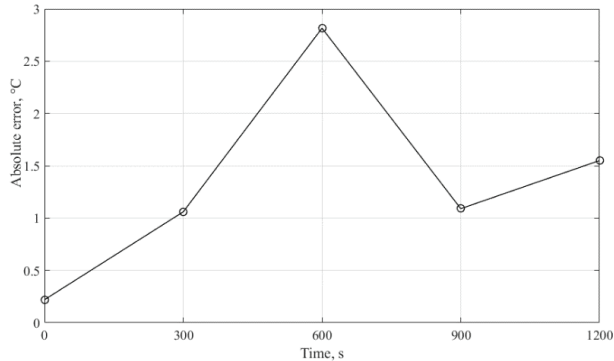


Fig. 4.10. The absolute error between the experimental and numerical solution at 3D textile layer

4.5. Concluding remarks

A numerical model, which imitates ventilation through the 3D textile in both stationary and time-dependent modes, has been developed.

It has been found that there is a slight difference between the average temperature, the effective heat transfer coefficients ($h_{micro\text{layer}}$, h_{inside} , and h_{total}), considering the mass flow rate of 0 and 0.2 dm³/min. However, the mass flow rate (ventilation layer) influence can be seen between 0 and 0.8 dm³/min. Increasing the mass flow rate from 0 to 0.8 dm³/min caused a decrease of thermal resistance and average temperature.

The model was expanded to include the mass flow rate through the ‘microclimate’. It was obtained that the effective heat transfer coefficient $h_{microlayer}$ decreases from 29.08 to 23.48 W/(K·m²), when the ventilation rate is 0.8 dm³/min. The mass flow rate through the ‘microclimate’ led to the increase of heat transfer coefficient h_{inside} in the ventilation domain.

The model is based on the assumption that flow is the laminar incompressible flow. For this reason, the model is valid in the range of small mass flow rates. However, 0.2 dm³/min and 0.8 dm³/min refer to the velocity of 1.47 m/s and 5.66 m/s, which can be reasonable wearing conditions.

Furthermore, the macro-scale model has been developed. The heat transfer coefficients of the ventilation layer were applied from the micro-scale model. The obtained results demonstrated quantitative and qualitative similarities with the experimental data.

CONCLUSIONS

In this thesis, the finite element models were created to simulate the physical processes, taking place during the air permeability, water-vapor resistance, and thermal resistance measurement tests that were performed on the textile fabrics of complex internal structures. The models were developed for a representative volume element (RVE) of the fabric cross-section. The outcomes of the numerical simulations are air permeability, water-vapor resistance, water-vapor transmission, thermal resistance, effective thermal conductivity, and effective heat transfer coefficients. In order to predict the air permeability, water-vapor resistance, and water-vapor transmission coefficients, the analysis covered 15 different geometry models that include one-layer, two-layer (close to real and simplified geometry), and 3D textile models. The RVE of one-layer, close to the real geometry, and 3D textile models were used in the thermal resistance simulation, assuming that textile is made from Nomex III, Cotton, Polyester (PES), and Polypropylene. The proposed models demonstrated a good agreement with the experimental measurements that were presented in literature. Furthermore, this research work was extended to predict the effective heat transfer coefficients of the smart textile structures with active ventilation. Following the theoretical and experimental investigation, the main conclusions were reached:

1. The numerical experiments of the air permeability demonstrated that there is no significant difference between the air permeability coefficient and the different number of pores (a void space between yarns). However, the proper selection of the mesh should be taken into account. The convergence analysis allowed reducing the simulation time by identifying the optimal mesh size, considering acceptable relative errors between the experimental data and numerical prediction of air permeability coefficient.

2. The relative errors of the predicted air permeability coefficients did not exceed 1 %, 5 %, and 8 %, respectively to one-layer structures with a structural density of 22/15, 22/20, and 29.3/15.

3. The relative errors of the predicted air permeability of two-layer textile vary from 3.57 % to 16.70 %. The reasons for the relative errors are the unknown distance between layers (air gap), the alignment of pores in each layer. Furthermore, the analytical model, which was used to compare the predicted air permeability values, is related to the experimental measurements, which have a limited number of experiments and include different geometry of the samples.

4. The numerical experiments of the water-vapor resistance demonstrated sensitivity to different RVE geometry. During simulations, the textile domain was changed from close to real geometry to simplified geometry. The main reason for sensitivity was different pressure drops. The selection and use of a simplified RVE geometry during the water-vapor resistance simulation require being very careful.

5. The numerical experiments of thermal resistance test were performed, considering the heat exchange due to conduction. The numerical experiments of one-layer structures were compared with the measurements that were found in literature and demonstrated quite a good agreement.

6. The numerical investigation was extended, including the ventilation layer. A ventilation model demonstrated that the increase of mass flow rate on the ventilation boundary ($\partial\Omega_{\text{inlet}}$) caused a thermal resistance decrease in the 3D textile. However, the developed ventilation model is valid for low mass flow rates.

7. The heat transfer coefficients $h_{\text{microlayer}} = 23.48 \text{ W}/(\text{K}\cdot\text{m}^2)$, $h_{\text{total}} = 8.65 \text{ W}/(\text{K}\cdot\text{m}^2)$ that were obtained from the ventilation model in the micro-scale were applied to the macro-scale model. The obtained mean absolute error is 1.35 °C. The findings indicated quantitative and qualitative similarities between the numerical experiments and measurements.

SANTRAUKA

ĮVADAS

Medžiagų ir konstrukcijų fizikinio elgesio kompiuterinis modeliavimas jau seniai yra neatsiejama inžinerijos, mechaninės ir mechatronikos inžinerijos, karo pramonės ir daugelio kitų technikos sričių naujų produktų kūrimo ir projektavimo dalis. Šiuolaikinės baigtinių elementų skaičiavimo technologijos leidžia realistiškai pavaizduoti fizikinius procesus. Dažnai kompiuterinių modeliavimų rezultatai yra adekvatūs ir patikimi, tad leidžia skaičiavimais pakeisti daugelį eksperimentų. Bendra kompiuterinio modeliavimo kaina ir laikas beveik visada yra žymiai mažesni nei eksperimentinio tyrimo atveju. Kompiuteriniai ištekčiai, reikalingi tam tikrai struktūrai modeliuoti, tampa mažesni, jei modelis sukonstruotas racionaliai.

Ne visada įmanoma vienareikšmiškai atsakyti, kokį skaitinį modelį naudoti konkrečiam tyrimui. Tiriamą sistemą paprastai galima kurti skirtingo sudėtingumo modeliais ir nevienoda mažesnės skalės fizikinių reiškinių skiriamąja geba (rezoliucija). Modelio skiriamoji geba apibendrina modelio vaizduojamų struktūrinių detalių arba jo vidinės struktūros elementų smulkumą. Sukurtam modeliui apskaičiuoti dažnai nereikia itin galingų kompiuterių, tačiau gautos informacijos pakanka praktiniams tikslams.

Tekstilės audinio struktūros yra tipiški pavyzdžiai, į kuriuos reikia atsižvelgti skirtingomis geometrinėmis skalėmis. Šiluminis dėvėjimo patogumas priklauso nuo audinio gebėjimo perduoti šilumą, orą ir vandens garus. Iš pirmo žvilgsnio tekstilės audinys yra membrana, kuriai būdingos tam tikros fizikinės šilumos ir masės perdavimo savybės. Taikydami tokį požiūrį, galime daugiau ar mažiau teisingai modeliuoti pagrindinius šilumos, oro ir vandens garus per audinius. Skaičiavimų tikslumas priklauso nuo to, kokias savybes suteiksime audinio struktūros membraniniams elementams. Norint nustatyti elemento savybes, reikia išspręsti kitą problemą – kaip nedidelis audinio gabalėlis, kurio struktūra yra žinoma, „elgiasi“ esant tam tikroms apkrovos sąlygoms. Šiuo tikslu yra sukurtas mažo audinio fragmento modelis mikromasteliu. Šis patobulintas modelis gali vaizduoti siūlų audimą, vidinę 3D tekstilės struktūrą ir daugelį kitų nuo aplinkybių priklausančių charakteristikų. Siūlai, gijos ir 3D tekstilės struktūros natūraliai vaizduojamos kaip tūriškai išdėstytos šilumai laidžių strypų struktūros, o tarpai tarp jų rodo dujų sritį. Skaitiškai eksperimentuojant su tokiu modeliu galima nustatyti bendrąsias audinio elemento savybes makromastelyje. Kai vidinė struktūra yra sudėtinga, taip nustatytos membranos elemento savybės bus daug artimesnės tikrovei, nei aprašant jas supaprastintais analitiniais modeliais. Modelis gali būti toliau tobulinamas. Komponentų, sudarytų iš 3D tekstilės sluoksnio, rinkinys taip pat gali turėti savo vidinę struktūrą. Paprastai jie susideda iš plonų gijų. Pereinant prie kito skiriamosios gebos etapo, galima pabandyti sumodeliuoti vieno siūlo fizikinį elgesį, vaizduojant jį kaip vientisą 3D kūną. Patikslintas elementas gali būti naudojamas 3D tekstilės audinio elementui modeliuoti, o iš pakoreguoto 3D audinio elemento galima sukurti visą struktūrinį tekstilės modelį. Tokia modelių seka, teikianti informaciją iš esmės apie tą patį fizikinį procesą, esant skirtingoms skiriamosioms geboms, vadinama

daugiaskaliu požūriū. Jis apima to paties objekto heterogeninių (t. y. struktūriškai skirtingų) modelių klasę.

Šiame darbe, pradėdant mažiausios struktūros mikromodeliais, kuriame vis labiau apibendrintus baigtinius elementus, kol galiausiai gauname priimtino matavimo realios konstrukcijos modelį, t. y. tokį, kuriam apskaičiuoti reikalingi kompiuterio ištekčiai yra praktiškai pritaikomi. Toks procesas vadinamas modelio redukcija arba supaprastinimu, kuris gali būti atliekamas tiek vienu, tiek keliais etapais.

Šioje disertacijoje nagrinėjama, kaip skirtingų skiriamųjų gebų modelius galima susieti naudojant matematinius metodus. Praktinį tokio skaičiavimo poreikį lemia būtinybė rasti efektyvius šiuolaikinių / funkcinės tekstilės medžiagų šilumos perdavimo, šiluminio atsparumo, vandens garų atsparumo, vandens garų laidumo ir oro laidumo koeficientus, kad būtų galima numatyti audinių funkcines savybes makroskalėje.

Tyrimo objektas

Tyrimo objektas yra fizikinis šilumos, oro ir vandens garų mainų procesas tarp žmogaus odos ir 3D tekstilės sluoksnio. 3D tekstilė yra tūrinė struktūra, sudaryta iš dviejų tekstilės sluoksnių (viršutinio ir apatinio), kuriuos jungia tarpinių siūlų sistema arba tarpinis sluoksnis.

Tyrimo tikslas

Darbo tikslas yra sukurti ir ištirti mikroskalės baigtinių elementų modelius, kurie imituoja šilumos ir masės mainų procesus 3D tekstilės struktūrose. Baigtinių elementų modeliai yra skirti oro laidumo, atsparumo vandens garams, šiluminio atsparumo koeficientams prognozuoti, remiantis rezultatais, gautais apskaičiuojant būdingų struktūrinių fragmentų fizikinį elgesį pagal didesnės skiriamosios gebos modelius.

Tyrimo uždaviniai

Norint pasiekti disertacijos tyrimo tikslą, buvo suformuluoti tyrimo uždaviniai:

1. Sukurti mikromastelio skaitinį šilumos ir drėgmės perdavimo per tekstilės struktūras modelį. Šio skaitinio modelio rezultatai yra fizikiniai parametrai, tokie kaip oro laidumo, atsparumo vandens garams ir šiluminio atsparumo koeficientai.
2. Įvertinti ir patikrinti skaitinių modelių konvergavimą.
3. Patikrinti sukurtus skaitinius modelius makromasteliu. Sukurti makromastelio baigtinių elementų modelį šilumai ir drėgmei perduoti. Šiame modelyje atitinkamos medžiagos savybės yra naudojamos iš mikromastelio modeliavimo.
4. Palyginti skaitinio modelio efektyvumą su eksperimentiniais matavimais. Atsparumo vandens garams ir šiluminės varžos matavimai buvo testuojami ir modeliuojami pagal standartą LST EN 31902 / ISO 11092: 2014 (en). Taip pat oro laidumo matavimas buvo modeliuojamas pagal ISO 9237: 1995 (E) standartą.
5. Išplėsti skaitinius modelius, kad būtų galima įvertinti 3D tekstilės struktūrų su priverstine ventilacija efektyvius šilumos perdavimo koeficientus.

Tyrimų metodika

Baigtinių elementų metodas yra taikomas siekiant įvertinti komforto savybes pagal 3D tekstilės audinio parametrus. Statinė ir dinaminė reprezentatyviojo modelio

analizė buvo atlikta naudojant šilumos ir masės mainų dalinių diferencialinių lygčių baigtinių elementų sprendimą. Taip pat taikant bendruosius skaitinius metodus algebrinėms ir paprastosioms diferencialinėms lygtims spręsti. Baigtinių elementų modelių sukūrimui ir rezultatų apdorojimui buvo naudojama COMSOL MULTIPHYSICS 5.6 ir MATLAB programinė įranga.

Darbo mokslinis naujumas ir praktinė reikšmė

Disertacijoje siūloma nauja supaprastintų šilumos ir masės mainų baigtinių elementų modelių sukūrimo metodika, pagrįsta didesnės skiriamosios gebos modelių skaitinės analizės rezultatais. Naujumo elementų galima rasti sujungus du skirtingos skiriamosios gebos modelius į vieną struktūrą. Kompiuterinė šiuolaikinių tekstilės medžiagų analizė leidžia geriau suprasti šilumos ir masės perdavimo procesus, vykstančius tarp žmogaus odos ir aplinkos. Šios darbo naujumas taip pat yra metodikos išplėtimas, siekiant gauti lygiaverčius parametrus, tokius kaip oro laidumo, atsparumo vandens garams, šilumos laidumo, šiluminio atsparumo, šilumos perdavimo koeficientas mikro- ir makroskalėse.

Darbo metu buvo sukurti specifiniai sumažintų baigtinių elementų modeliai, kuriuos galima pritaikyti modeliuojant aktualius ir sudėtingus šilumos ir masės perdavimo per 3D tekstilę procesus, taupant skaičiavimo laiką ir išlaikant praktiškai priimtina modelių atitiktį tikrovei. Sukurtus MATLAB ir COMSOL Multiphysics algoritmus ir skaičiavimo scenarijus supaprastintų modelių parametrams nustatyti galima pritaikyti kitų supaprastintų šilumos ir masės perdavimo modelių sintezei.

Ginamieji teiginiai

Siūlomas originalus požiūris pakeisti aukštos raiškos sudėtingą šilumos, oro ir vandens garų mainų perdavimo 3D tekstilės struktūroje modelį supaprastintu modeliu, kuris išlaiko savo savybes nustatydamas supaprastinto modelio parametrus.

Darbo rezultatų aprobavimas

Pagrindiniai disertacijos rezultatai paskelbti 4 mokslinės informacijos instituto (ISI) straipsniuose, iš jų 2 su citavimo indeksu bei 2 be citavimo indekso. Be to, rezultatai pristatyti 4 tarptautinėse konferencijose.

Disertacijos struktūra

Disertaciją sudaro įvadas, 4 pagrindiniai skyriai, išvados, santrauka, literatūros šaltinių sąrašas bei 1 priedas. Bendra disertacijos apimtis yra 123 puslapių įskaitant 41 paveikslą, 21 lentelę ir literatūros sąrašą sudarytą iš 145 cituojamų šaltinių.

1. LITERATŪROS APŽVALGA

Požangi tekstilė yra plačiai naudojama aviacijos, automobilių, kariuomenės, medicinos, žmogaus kūno ir inžinerinių konstrukcijų apsaugoje, sporto ir laisvalaikio drabužiuose ir kitose srityse [1]. Pavyzdžiui, techninė tekstilė aviacijos srityje yra naudojama specialioms drabužiams (neperšlampamos striukės, pritaikomos uniformos), automobilių pramonėje kaip automobilių pamušalas, oro pagalvės, ugniai atsparūs sėdinių užvalkalai, karinėse ir viešosiose tarnybose kaip neperšaunamos striukės, medicinos ir sveikatos priežiūros srityje kaip tvarsčiai [2].

Tekstilės ruošiniai gali būti klasifikuojami remiantis įvairiais kriterijais, įskaitant sutvirtinimo / armatūros laipsnį storio kryptimi (pvz., dviejų ir trijų

matmenų), pluošto orientacijos skaičių (pvz., vienašis, dviašis) ir gamybos būdą (pvz., austi, neausti, pinti, megzti) [6], [7]. Įvairios fizikinės savybės gali būti naudojamos norint įvertinti tekstilės medžiagų elgseną ar eksploatacines savybes. Pavyzdžiui, mechaninės savybės, tokios kaip tempimo savybės, suspaudimo ir kt. identifikuoja medžiagos atsparumą išorinėms jėgoms, sukeliančioms medžiagos deformacijas. Šilumos ir vandens perdavimo savybės, tokios kaip laidumas orui, atsparumas vandens garams, šiluminis atsparumas ir kt. Fizinės savybės, pavyzdžiui, verpalų skersmuo, storis, porėtumas, struktūrinis tankis ir kt. Vidiniai ir išoriniai veiksniai, taip pat audinio ir žmogaus tarpusavio sąveika gali turėti įtakos audinio/tekstilės elgsenai [2]. Svarbiausias drabužių kūrėjų ir inžinierių iššūkis yra užtikrinti termofiziologinį komfortą tarp žmogaus odos ir audinio. Tokie teoriniai ir skaitiniai pažangių tekstilės medžiagų fizikinio elgesio tyrimai yra palygintusudėtingi dėl sudėtingos vidinės struktūros, tuo pačiu metu vykstančių šilumos ir drėgmės perdavimo ir kitų fizikinių procesų, vykstančių skirtingose erdvės ir laiko skalėse [16].

1.1. Audinių šiluminio komforto savybių apžvalga

Svarbiausios tekstilės šiluminės komforto savybės yra atsparumas vandens garams, šiluminis atsparumas, laidumas orui, skysčio pašalinimo greitis, atsparumas vandeniui (esant hidrostatiniam slėgiui) [18]. Šiame darbe aptarsime laidumą orui, atsparumą vandens garams bei šiluminį atsparumą.

Laidumas orui pagal ISO 9237:1995 (E) standartą yra apibrėžiamas, kaip oro srauto, einančio statmenai per bandinį, greitis esant nustatytam bandinio plotui, slėgių skirtumui ir laiko sąlygomis. Oro laidumas gali būti apskaičiuojamas pagal formulę (1), kur \hat{q} – oro srauto debitas dm^3/min ; A – bandinio plotas, cm^2 ; 167 – perskaičiavimo iš dm^3/min į mm/s koeficientas [21].

$$R = \frac{\hat{q}}{A} \cdot 167. \quad (1)$$

Atsparumas vandens garams ir šiluminis atsparumas gali būti eksperimentiškai pamatuotas naudojant „Sweating Guarded Hot Plate M259B“ prietaisą. Pagal ISO 11092:2014 standartą tekstilės medžiagų ar kompozitų **atsparumas vandens garams** yra savitasis dydis, nusakantis slaptosios (angl. *latent*) garavimo šilumos srautą per tam tikrą plotą, priklausomai nuo naudojamo pastovaus vandens garų slėgio gradiento. Matavimai atliekami esant pastoviai matavimo bloko temperatūrai $T = 35^\circ\text{C}$, pastoviam oro santykiniam drėgnumui $\text{RH} = 40\%$, oro greitis 1 m/s . Atsparumo vandens garams koeficientas R_{et} randamas pagal formulę (2), kur p_v – vandens garų parcialinis / dalinis slėgis Pa, p_{sat} – prisotintų vandens garų slėgis Pa, H – šildymo galia W, kuri reikalinga palaikyti plokštelės temperatūrai $T = 35^\circ\text{C}$, ΔH_c – pataisos koeficientas, R_{et0} – prietaiso konstanta $\text{m}^2 \text{ Pa/W}$, skirta vandens garų atsparumui matuoti R_{et} be bandinio („Tuščios plokštės“ atsparumas vandens garams) [22].

$$R_{et} = \frac{(p_{sat} - p_v)A}{H - \Delta H_c} - R_{et0}. \quad (2)$$

Tekstilės medžiagų ar kompozitų **šiluminis atsparumas** yra temperatūros skirtumas tarp bandinio abiejų pusių, padalintas iš kintamo šilumos srauto,

pratekančio per ploto vieneta gradiento kryptimi ([18], ISO 11092:2014). Matavimai atliekami esant bloko temperatūrai $T_m = 35$ °C, oro temperatūrai $T_a = 20$ °C, santykinis drėgnumas RH = 65 %. Šiluminis atsparumas R_{ct} randamas pagal formulę (3), kur H – šildymo galia W, reikalinga palaikyti plokštelės temperatūrai $T = 35$ °C, ΔH_c – pataiso koeficientas, R_{ct0} – prietaiso konstanta $m^2 K/W$, skirta šilumos atsparumui matuoti R_{ct} be bandinio („Tuščios plokštės“ šiluminis atsparumas) [18].

$$R_{ct} = \frac{(T_m - T_a)A}{H - \Delta H_c} - R_{ct0} . \quad (3)$$

Atlikus šiluminio atsparumo matavimus, šiluminis laidumas λ W/(m·K) randamas padalinus bandinio storį L iš šiluminio atsparumo R_{ct} [18].

$$\lambda = \frac{L}{R_{ct}} . \quad (4)$$

Žinant šiluminį atsparumą, atsparumą vandens garams nesunkiai gali būti randamos kitos tekstilės savybės, kaip vandens garų pralaidumo indeksas, vandens garų pralaidumas, šiluminis sugeriamumas (angl. *thermal absorptivity*), šilumos perdavimo koeficientas.

2. METODOLOGIJA

2.1. 3D tekstilės reprezentatyvusis elementas tūrinis elementas mikroskalėje

3D tekstilės struktūros (tarpiniai audiniai) yra sudarytos iš dviejų atskirų išorinių audinio sluoksnių, sujungtų tarpiniais siūlais arba sluoksniu. Tarpiniai audiniai gali būti pagaminti naudojant metmenų mezgimo (angl. *warp knitting*), ataudų mezgimo (angl. *weft knitting*), audimo (angl. *weaving*), neaustines (angl. *non-woven*) ar pynimo (angl. *braiding*) technologijas [111], [112].

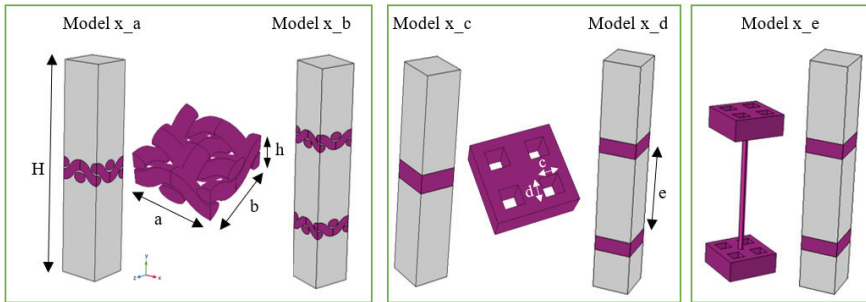
Šiame tyrime 3D tekstilės struktūros reprezentatyvusis tūrinis elementas (angl. *representative volume element, RVE*) mikroskalėje buvo sukurtas remiantis eksperimentiniais [8] tyrimais. Tyrėjai darbe [8] analizavo 36 vieno sluoksnio austų audinių konstrukcijos parametrus, oro laidumo (AP) koeficientą. Oro laidumo matavimai buvo atlikti naudojant prietaisą „FX 3300 Labotester III“ („Textest Instruments“). Trijų pasirinktų bandinių eksperimentinių nustatymų ir matavimų rezultatai pateikti 2.1 lentelėje.

Norėdami sukurti realistišką 3D tekstilės reprezentatyvųjį tūrinį elementą, pirmiausia remiantis [8] moksliniu tyrimu sukūrėme vieno sluoksnio drobinio pynimo (angl. *plain weave*) tris reprezentatyviuosius tūrinius elementus. Kitu žingsniu padarėme prielaidą, kad oro tarpus tarp siūlų (poras) galime supaprastinti kvadratais. Supaprastinti modeliai leido sutaupyti skaičiavimo resursų. Paveikslėlyje (1 pav.) pateikta *Model x_a* ir *Model x_c* geometrijos, kurios vaizduoja vieno sluoksnio realistišką tekstilės bandinį ir supaprastintos geometrijos tekstilės bandinį. Skaičiuojamojo modelio žymėjime *Model x_a* ir *Model x_c*, x yra bandinio numeris (žr. 2.1. lentelėje), a raidė atitinka vieno sluoksnio realistišką geometriją, c – supaprastintą vieno sluoksnio geometriją. Remiantis vieno sluoksnio modeliais buvo sukurti *Model x_b* ir *Model x_d*, kurie vaizduoja dviejų sluoksnių realistišką geometriją bei supaprastintos geometrijos reprezentatyviuosius tūrinius elementus.

Atstumas tarp sluoksnių fiksuotas 3,06 mm. Tyrime naudoti reprezentatyvieji tūrinio elemento modeliai pateikti 1 pav. Apibendrinti oro ir tekstilės sluoksnio srities parametrai pateikti lentelėje 2.2.

2.1 lentelė. Nustatyti ir išmatuoti konstrukcijos parametrai [8]

Nr.	Struktūrinis tankis, warp / weft	Pamatuotas warp tankis, (ends / cm)	Pamatuotas weft tankis, (picks / cm)	Storis, (mm)	Pamatuotas oro laidumo koef. (AP), (mm / s)	Standartinis nuokrypis (%)
1	22 / 15	21	15	0,439	2391,67	8,20
2	22 / 20	21	20	0,438	1571,67	1,58
3	29,3 / 15	28	15	0,468	1268,33	1,42



1 pav. Tyrime naudojami reprezentatyvieji tūriniai elementai, čia x bandinio numeris

2.2 lentelė. Oro ir tekstilės sluoksnio srities parametrai

Modelis	Ilgis ir plotis, $a \times b$ (mm)	Aukštis (oro srities), H (mm)	Tekstilės storis, h (mm)	Poros ilgis ir plotis, $c \times d$ (mm)	Atstumas tarp tekstilės sluoksnių, e (mm)
Model 1 a	1,1 x 1,1	10	0,439	-	-
Model 2 a	0,98 x 0,98	10	0,438	-	-
Model 3 a	0,85 x 0,85	10	0,468	-	-
Model 1 b	1,1 x 1,1	10	0,439	-	3,06
Model 2 b	0,98 x 0,98	10	0,438	-	3,06
Model 3 b	0,85 x 0,85	10	0,468	-	3,06
Model 1 c	1,1 x 1,1	10	0,439	0,263 x 0,263	-
Model 2 c	0,98 x 0,98	10	0,438	0,195 x 0,195	-
Model 3 c	0,85 x 0,85	10	0,468	0,155 x 0,155	-
Model 1 d	1,1 x 1,1	10	0,439	0,263 x 0,263	3,06
Model 2 d	0,98 x 0,98	10	0,438	0,195 x 0,195	3,06
Model 3 d	0,85 x 0,85	10	0,468	0,155 x 0,155	3,06
Model 1 e	1,1 x 1,1	10	0,439	0,263 x 0,263	3,06
Model 2 e	0,98 x 0,98	10	0,438	0,195 x 0,195	3,06
Model 3 e	0,85 x 0,85	10	0,468	0,155 x 0,155	3,06

Ekvivalentinė 3D tekstilės geometriją atitinka „Model 1_e“, „Model 2_e“ ir „Model 3_e“, modeliai yra sudaryti iš dviejų supaprastintos geometrijos tekstilės sluoksnių gautų iš „Model 1_d“, „Model 2_d“ ir „Model 3_d“ geometrijos bei jungiamojo siūlo su spinduliu 0,08 mm. „Model x_d“ pateikia supaprastintą vidinę tekstilės geometriją, pagrįstą modeliais „Model x_a“, „Model x_b“ ir „Model x_c“.

2.2. Skaitinis oro laidumo modeliavimas

Audinių oro laidumas (AP) yra labai svarbi komforto savybė, turinti įtakos skysčių ir garų laidumo savybėms bei aprangos šiluminiam atsparumui [9]. Šiame tyrime buvo sukurti AP modeliai, atsižvelgiant į vėpalų vidinį laidumą \mathbf{K} , m^2 . Vidinį laidumą \mathbf{K} , m^2 galima apskaičiuoti remiantis Darcy dėsnium:

$$\frac{Q}{A_s} = \mathbf{K} \frac{\Delta p}{\mu \cdot L}, \quad (5)$$

kur Q – debitas (m^3/s), \mathbf{K} – vidinis laidumo koeficientas (m^2), Δp – slėgių gradientas (Pa), μ – fluído dinaminė klampa ($\text{Pa}\cdot\text{s}$), A_s – skerspjūvio plotas (m^2), L – tekstilės bandinio storis (m) [88]. Debitas Q gali būti randamas pagal formulę (6), atlikus skaitinius skaičiavimus, kur integruojamas greičio laukas \mathbf{u}_{cfd} , per skerspjūvio plotą A_s , \mathbf{n} – normalės vektorius [88].

$$Q = \iint_{A_s} \mathbf{u}_{\text{cfd}} \cdot \mathbf{n} \, dA. \quad (6)$$

Pagal [124] gautą fluído dervos (angl. *resin*) masės srautą per išėjimo kraštinę galima naudoti vidiniam laidumui apskaičiuoti. Be to, vidinį laidumą galima apskaičiuoti skirtingomis kryptimis. Toks skaitinis fluído modeliavimas dažnai apima dervos (angl. *resin*) srautą, kuris yra naudojamas LCM (angl. *liquid composite molding*) procese. Skaitiniu modeliavimu sprendžiamos Stokes lygtys (esant nepralaidiems siūlams), Stokes-Darcy lygtys (esant laidiesiems siūlams) [92]. Be to, norint įvertinti vidinį laidumą gali būti naudojami analitiniai modeliai, tokie kaip Gebart, Kozeny–Carman ir kt.

Šiame darbe vidutinis oro laidumas (AP) per tekstilę buvo nustatomas, remiantis prielaidomis, kad srautas yra nesuspaustas Niutonis vienfazis srautas (angl. *incompressible Newtonian single-phase flow*). Be to, buvo atliktas nusistovėjusios (stacionarios) būsenos modeliavimas, atsižvelgiant į tai, kad Reinoldso Re skaičius yra mažas, o tai reiškia, kad oro tėkmė yra laminarinė. Skaičiuojamoji sritis Ω yra sudaryta iš Ω_1 (oro sritis) ir Ω_2 (tekstilė (porėta terpė)) sričių. Sprendžiamos Navje-Stokso lygtys (7) su tolydumo lygtimi (8) Ω_1 srityje bei Brinkmano lygtys (9) su tolydumo lygtimi (8) Ω_2 srityje.

$$\rho(\mathbf{u} \cdot \nabla)\mathbf{u} = \nabla \cdot [-p\mathbf{I} + \mu(\nabla\mathbf{u} + (\nabla\mathbf{u})^T)] + \mathbf{F}. \quad \Omega_1 (7)$$

$$\rho \nabla \cdot (\mathbf{u}) = 0. \quad \Omega_1, \Omega_2 (8)$$

$$\frac{\rho}{\varepsilon_p} \left((\mathbf{u} \cdot \nabla) \frac{\mathbf{u}}{\varepsilon_p} \right) = \nabla \cdot \left[-p\mathbf{I} + \frac{\mu}{\varepsilon_p} (\nabla\mathbf{u} + (\nabla\mathbf{u})^T) \right] - (\mu\mathbf{K}^{-1})\mathbf{u}. \quad \Omega_2 (9)$$

Pagal [126] lygtis (7) sudaryta iš inercijos (konvekcijos) nario $(\mathbf{u} \cdot \nabla)\mathbf{u}$, streso divergencijos $-\rho\mathbf{I} + \mu(\nabla\mathbf{u} + (\nabla\mathbf{u})^T)$ ir išorinių jėgų \mathbf{F} (pvz., gravitacija). Šiame tyrime darėme prielaidą, kad nėra išorinių jėgų. Slėgio jėgų skirtumą apibūdina narys

$-\nabla p \mathbf{I}$. Pastaba. Esant nespūdžiai tėkmei difuzijos narys $\nabla \cdot \mu(\nabla \mathbf{u} + (\nabla \mathbf{u})^T) = \mu \nabla^2 \mathbf{u}$. Čia \mathbf{u} – greičio vektorius (m/s), \mathbf{I} – vienetinė matrica, p – slėgis (Pa), μ – dinaminė klampa (Pa·s), ρ – tankis (kg/m³). Lygtyje (9) \mathbf{K} – vidinis laidumas (m²), ε_p – porėtumo koeficientas. Vidinis laidumas \mathbf{K} buvo suskaičiuotas naudojant Gebart [81] analitinį modelį, kuris atsižvelgia į pluošto išdėstymą. Eksperimentiniai oro laidumo duomenys, tekstilės struktūriniai parametrai buvo pateikti [8] tyrime. Mes darėme prielaidą, kad medžiagos porėtumas $\varepsilon_p = 0,58$ ir vidinis laidumas $\mathbf{K} = 1,64 \cdot 10^{-11}$ (m²), kai tekstilė yra izotropinė ir pluošto išdėstymas yra kvadratinis. Skaičiavimai vidinio laidumo ir porėtumo pateikti [9] tyrime.

2 pav. vaizduoja skaičiavimo sritis ir kraštines sąlygas $\partial\Omega$. Kraštinės sąlygos aprašytos 2.3 lentelėje, kur \mathbf{n} – normalės vektorius, \mathbf{t} – tangentinis vektorius. Kraštinės sąlygos buvo pasirinktos pagal [8] atliktus matavimus oro laidumo testeriu „FX 3300 Labotester III“ („Textest Instruments“), slėgio skirtumas buvo nustatytas 200 (Pa) esant 20 cm² bandinio plotui.

2.3 lentelė. Kraštinės sąlygos naudotos oro laidumo tyrime [125]

Paviršius	Kraštinės sąlygos	Nustatymai ir prielaidos
$\partial\Omega_t$	$\mathbf{u} = \mathbf{0}$	Wall condition: No slip. No-slip sąlyga yra taikoma ant tekstilės paviršiaus. Fluido (oro) greitis yra lygus nuliui.
$\partial\Omega_{\text{air}}$	$\mathbf{u} \cdot \mathbf{n} = 0$ $\mathbf{K}_n - (\mathbf{K}_n \cdot \mathbf{n})\mathbf{n} = 0,$ $\mathbf{K}_n = \mathbf{K}\mathbf{n}$ Esant oro sričiai: $\mathbf{K} = \mu(\nabla \mathbf{u} + (\nabla \mathbf{u})^T)$ Esant porėtai (tekstilės) sričiai: $\mathbf{K} = \frac{\mu}{\varepsilon_p}(\nabla \mathbf{u} + (\nabla \mathbf{u})^T)$	Wall condition: slip. Slip kraštinė sąlyga yra taikoma oro paviršiui, kur nėra kontakto su tekstile.
$\partial\Omega_{\text{inlet}}$	$\mathbf{n}^T[-p\mathbf{I} + \mathbf{K}]\mathbf{n} = -\hat{p}_0$ $\hat{p}_0 \geq p_0, \mathbf{u} \cdot \mathbf{t} = 0$ $p_0 = 200 \text{ Pa}$	Inlet (Suppress backflow). Pagal eksperimentą slėgių skirtumas yra 200 Pa. Slėgio sąlyga $p_0 = 200 \text{ Pa}$ yra ant $\partial\Omega_{\text{inlet}}$ paviršiaus.
$\partial\Omega_{\text{outlet}}$	$[-p\mathbf{I} + \mathbf{K}]\mathbf{n} = -\hat{p}_0\mathbf{n}$ $\hat{p}_0 \leq p_0$ $p_0 = 0 \text{ Pa}$	Outlet. Santykinis slėgis $p_0 = 0 \text{ Pa}$ ant $\partial\Omega_{\text{outlet}}$ paviršiaus. Fizikinė reikšmė, kad absoliutus slėgis lygus santykiniam slėgiui (1 [atm]). Slėgių sąryšis: $p_A = p_{\text{ref}} + p_0$.

Norėdami prognozuoti audinio vandens garų atsparumą R_{et} , skaitiniame modeliavime naudojame vandens garų tankį ir dinaminę klampą esant $T = 35 \text{ }^\circ\text{C}$ temperatūrai ir santykinėi drėgmei $RH = 40 \%$. Drėgno oro savybės buvo nustatytos remiantis idealių dujų dėsniumi. Eksperimentines R_{et} koeficientą galima nustatyti pagal formulę (2). Santykinės drėgmės RH ir dalinio / parcialinio garų slėgio p_v ryšys atitinka formules (10) ir (11) [134]. Gauname, kad parcialinis garų slėgis $p_v = 2248,5 \text{ Pa}$ ir prisotintų garų slėgis $p_{sat} = 5621,3 \text{ Pa}$.

$$RH = \frac{p_v}{p_{sat}(T)} \cdot 100\% = \varphi \cdot 100 \%. \quad (10)$$

$$p_{sat}(T) = 610.7[\text{Pa}] \cdot 10^{7.5 \frac{T-273.15[\text{K}]}{T-35.85[\text{K}]}}. \quad (11)$$

Skaitinis modeliavimas buvo atliktas naudojant Comsol Multiphysics programinę įrangą. Norint imituoti eksperimentą gali būti naudojamos *Laminar Flow (.spf)* ir *Moisture Transport in Air (.mt)* sąsajos. Buvo daromos prielaidos, kad fizikinis procesas yra izoterminis (nėra temperatūros ir RH pokyčių), fluidas yra nesuspaudžiamas (pastovus masės tankis), mažas Re skaičius ir kad vandens garai yra niutoninis fluidas (pastovi dinaminė klampa). Buvo sprendžiamos Navje-Stokso lygtys (7), (8) bei (12).

$$M_v \mathbf{u} \cdot \nabla c_v + \nabla \cdot \mathbf{g}_w = G. \quad (12)$$

Lygtis (12) skirta automatiškai apskaičiuoti drėgno oro savybes, čia $\mathbf{g}_w = -M_v D \nabla c_v$, $c_v = \varphi c_{sat}$. c_{sat} yra sočiųjų garų koncentracija $c_{sat} = \frac{p_{sat}}{RT}$, D – garų difuzijos koeficientas ore, M_v – vandens garų molinė masė [123]. Mūsų atveju difuzinis drėgmės srautas \mathbf{g}_w ir drėgmės šaltinio narys $G \text{ kg}/(\text{m}^3 \cdot \text{s})$ yra lygūs nuliui. Kraštinės sąlygos yra pateiktos 2.5 lentelėje ir pavaizduotos 2 pav.

2.5 lentelė. Kraštinės sąlygos skaitinio R_{et} modelio

Paviršius	Kraštinės sąlygos	Nustatymai ir prielaidos
$\partial\Omega_{inlet}$	$\mathbf{u} = -U_0 \mathbf{n}$ $U_0 = 1 \text{ m/s}$	Inlet (Suppress backflow). Pagal eksperimentą įeinantis drėgno oro greitis 1 m/s .
$\partial\Omega_{inflow}$	$c_{ustr} = \varphi_{w,ustr} c_{sat}(T_{ustr})$ $-\mathbf{n} \cdot \mathbf{g}_w = M_v d_z (c_v - c_{ustr}) \mathbf{u} \cdot \mathbf{n}$	Inflow. Remiantis eksperimentu $T_{ustr} = 35 \text{ }^\circ\text{C}$, $\varphi_{w,ustr} = 0,4$. c_{ustr} – vandens garų koncentracija.
$\partial\Omega_{outflow}$	$-\mathbf{n} \cdot \mathbf{g}_w = 0$	Outflow. Nulinis difuzinis srautas taikomas ant išėjimo paviršiaus.

Nustatant atsparumo vandens garams (R_{et}) koeficientą, buvo pakeista kraštinė sąlyga, imituojanti drėgno oro greitį *Laminar Flow (.spf)* sąsajoje. $\partial\Omega_{inlet}$ buvo pakeista iš slėgio į greičio kraštinę sąlygą. Kitos kraštinės sąlygos buvo naudojamos tokios pat, kaip laidumo orui tyrime. Be to, įtraukiant *Moisture Transport in Air (.mt)* sąsają, buvo naudojamos dvi kraštinės sąlygos $\partial\Omega_{inflow}$ ir $\partial\Omega_{outflow}$, kurios atspindi drėgno oro srautą. Atlikus skaitinį modeliavimą rezultatams gauti buvo atlikti perskaičiavimai, dėl to, kad formulėje (2) nėra žinoma šildymo galia H , reikalinga

palaikyti temperatūrą $T = 35 \text{ }^\circ\text{C}$. Remiantis [16] buvo daroma prielaida, kad šildymo galia H gali būti interpretuojama kaip vandens garų, prisiskverbiančių į tekstilės sluoksni, galia. Tada vandens garų atsparumas randamas $R_{et} = \frac{\rho_v}{\delta_p(p_{sat}-p_v)}$ s/m. Čia vandens garų perdavimo koeficientas $\delta_p = \frac{w_v}{A\Delta p}$ s/m, ρ_v – drėgno oro tankis kg/m^3 , w_v – vandens garų masės srautas kg/s , Δp – slėgių skirtumas tarp paviršių $\partial\Omega_{inlet}$ ir $\partial\Omega_{outlet}$. Prieš atliekant skaičiavimus buvo sukurti integravimo *intop1* ir vidutinės reikšmės *aveop1*, *aveop2* operatoriai. Operatorių pozicijos pavaizduotos 2 pav. Naudojant globalias išraiškas, δ_p gali būti randama pagal išraišką: $intop1(sp.f.U) \cdot aveop1(mt.wc_v) / (intop1(1) \cdot (aveop1(p) - aveop2(p)))$. Atsparumas vandens garams R_{et} gali būti įvertinamas pagal išraišką $aveop1(mt.rho_moist) / (intop1(sp.f.U) \cdot aveop1(mt.wc_v) / (intop1(1) \cdot (aveop1(p) - aveop2(p))) \cdot (aveop2(mt.psat) - aveop1(mt.pv)))$. Pastaba. Matavimo vienetai R_{et} ir δ_p yra vienodi $\frac{m^2 Pa}{W} = \frac{kg/s}{m^2 Pa} = \frac{s}{m}$.

2.4. Šiluminio atsparumo skaitinis modeliavimas

Šiluminio atsparumo koeficientas eksperimentiškai gali būti apskaičiuotas pagal formulę (3). Naudojant prietaisą „Sweating guarded-hotplate“ audinys yra dedamas tarp karštos ir šaltos plokštelės. Remiantis [137] šilumos konvekcijos galima nevertinti, kai audinys dedamas tarp dviejų plokštelių su temperatūros gradientu. Radiacijos galima nevertinti esant mažam temperatūros gradientui. Žinant šiluminio atsparumo koeficientą, šiluminio laidumo koeficientas gali būti randamas pagal formulę (4). Atvirkštinis dydis šiluminio atsparumo koeficientui yra šilumos perdavimo koeficientas [138].

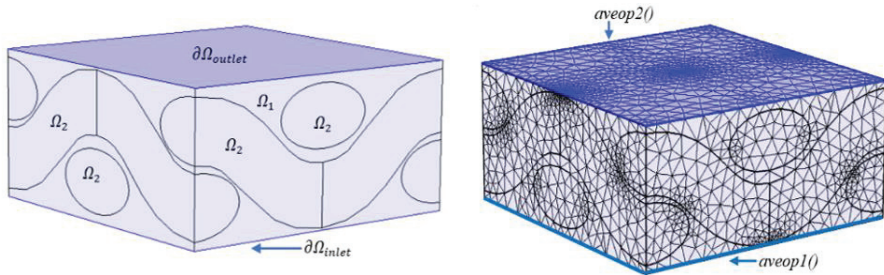
Skaitiniu modeliavimu šiluminio atsparumo koeficiento R_{ct} apskaičiavimas gali būti atliekamas naudojant *Heat transfer in solids and fluids(.ht)* sąsają. Šilumos lygtis yra pateikta (13) formulėje, kur C_p – savitoji (specifinė) šiluminė talpa (J/kg K), Q – bendra šilumos energija (W), $\mathbf{q} = -k\nabla T$, k – šiluminis laidumas ($W/m \cdot K$) [123].

$$\rho C_p \mathbf{u} \cdot \nabla T + \nabla \cdot \mathbf{q} = Q. \quad \text{in } \Omega_1, \Omega_2 \quad (13)$$

Skaitinio modelio prielaidos, leidžiančios įvertinti audinio šiluminio atsparumo (R_{ct}) koeficientą pateiktos žemiau:

- Analizuojamas stacionarus ne izoterminis šilumos srautas (tai reiškia, kad yra temperatūros pokyčių).
- Šilumos mainai vyksta tik dėl šiluminio laidumo (šilumos mainus dėl konvekcijos ir radiacijos atmetame).
- Fluido matrica yra sausas oras / drėgnas oras.

Tyrimė naudotos kraštinės sąlygos yra apibendrintos 2.6 lentelėje. Skaitinio modelio geometrija buvo pakeista atsižvelgiant į tekstilės storį. 3 pav. vaizduoja modelio geometrija su kraštinėmis sąlygomis.



3 pav. Vieno sluoksnio tekstilės kraštinės sąlygos, tinkelis ir operatorių pozicijos.

2.6 lentelė. Kraštinės sąlygos R_{ct} skaitinio modelio

Paviršius	Kraštinės sąlygos	Nustatymai ir prielaidos
$\partial\Omega_{inlet}$	$T = 35\text{ }^{\circ}\text{C}$	Temperature. Pastovi temperatūra $T = 35\text{ }^{\circ}\text{C}$ buvo taikyta ant $\partial\Omega_{inlet}$ paviršiaus, kuris imituoja odą.
$\partial\Omega_{outlet}$	$T = 20\text{ }^{\circ}\text{C}$	Temperature. Pastovi temperatūra $T = 20\text{ }^{\circ}\text{C}$ buvo taikyta ant $\partial\Omega_{outlet}$ išėjimo paviršiaus.

Skaitinio šiluminio atsparumo koeficiento modeliavimo tyrimas buvo atliktas naudojant skirtingas audinių savybes. Kietosios matricos (tekstilės) savybės pateiktos 2.7 lentelėje. Šilumos laidumą galima pavaizduoti kaip diagonalią matricą (tenzorių). Šilumos laidumas išilgai pluošto ašies yra K_{11} . Šilumos laidumą, statmeną pluošto ašiai, atitinka K_{22} ir K_{33} [137]. Buvo tirti du fluideo matricos atvejai. Pirmieji skaitiniai modeliavimai buvo atlikti naudojant sausą orą kaip fluidą. Tačiau remiantis eksperimentu santykinė oro drėgmė yra $RH = 65\%$. Taigi antrasis atvejis buvo, kai fluidas yra drėgnas oras. Panašų eksperimentinį ir skaitinį šiluminio atsparumo tyrimą atliko [137].

2.7 lentelė. Kietosios matricos šiluminės savybės [137]

Medžiagos savybės	Nomex III	Medvilnė	Polisteris	Polipropilenas
ρ , (kg/m^3)	1380	1520	1390	910
K_{11} , ($\text{W}/\text{m}\cdot\text{K}$)	1,3	2,88	1,26	1,241
$K_{22}=K_{33}$, ($\text{W}/\text{m}\cdot\text{K}$)	0,13	0,243	0,157	0,111
C_p , ($\text{J}/\text{kg}\cdot\text{K}$)	1200	1350	1030	1680

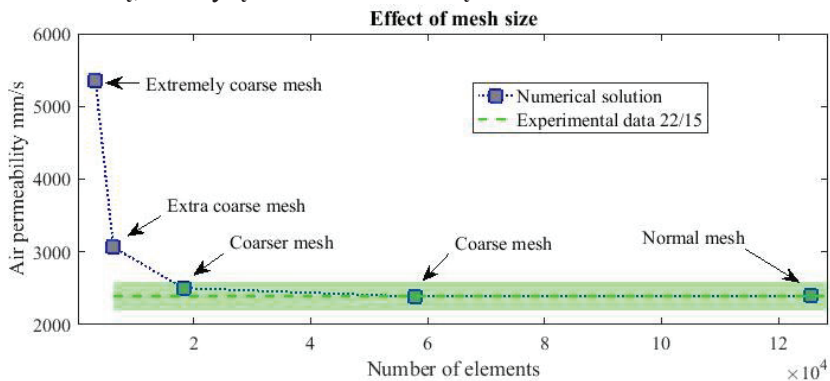
3. SKAITINIAI EKSPERIMENTAI

3.1. Oro laidumo verifikavimo ir validavimo tyrimas

Atliekant skaitinius modeliavimo tyrimus svarbu įvertinti modelio konvergavimą, rasti optimalų tinkelio dydį atsižvelgiant į skaičiavimo laiką ir tikslumą. Skaitinio modelio santykinė paklaida buvo skaičiuojama tarp

eksperimentinės oro laidumo koeficiento reikšmės ir gautos baigtinių elementų metodu.

Konvergavimo tyrime buvo analizuojamas modelis *Model 1_c*, kuris atitinka vieno sluoksnio 22 / 15 bandinio supaprastintą geometriją. Tyrimo metu reprezentatyvusis tūrinis elementas buvo nekintamas, o keičiamas tinklelio elementų skaičius, kuris buvo padidintas nuo 3194 iki 125512 elementų (žr. 3.1 lentelę). 4 pav. pateikta oro laidumo (AP) koeficiento priklausomybė nuo tinklelio dydžio. Žalia punktyrinė linija ir žalias plotas žymi eksperimentines vidutinio oro laidumo AP koeficiento ir jo standartinio nuokrypio vertes (šiuo atveju 8,2 %). Vidutinės oro laidumo (AP) koeficiento reikšmės, gautos atliekant skaitinius eksperimentus, pažymėtos pilkais kvadratėliais. Santykinė paklaida, atsižvelgiant į eksperimentinius duomenis, yra mažesnė nei 5 %, naudojant 18270 elementų tinklelį (žr. 3.1 lentelę). Santykinė paklaida sumažėja iki 0,25 % ir 0,16 %, naudojant atitinkamai tinklelį sudarytą iš 57795 ir 125512 elementų, tačiau skaičiavimo laikas ilgesnis. Optimalus tinklelio dydis atsižvelgiant į skaičiavimo laiką ir santykinę paklaidą yra tarp 18270 ir 57795 elementų. Tolėsniame tyrime supaprastintos geometrijos modeliams naudosime tinklelį, sudarytą iš 57795 elementų.



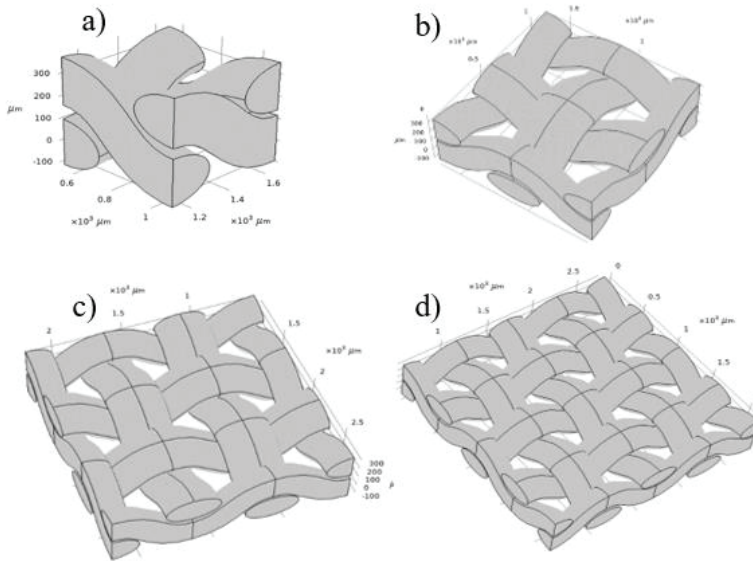
4 pav. Tinklelio elementų ir oro laidumo (AP) koeficiento priklausomybė

3.1 lentelė. *Model 1_c* konvergavimo tyrimo rezultatai

Tinklelio pavadinimas	Elementų skaičius /DOF	Laikas, s	AP, mm/s	Santykinė paklaida, %
Labai grubus (angl. <i>extremely coarse</i>)	3194/3304	4	5358,4	124,05
Ypač grubus (angl. <i>extra coarse</i>)	6249/5980	4	3061,9	28,02
Grubesnis (angl. <i>coarser</i>)	18270/15744	9	2503,1	4,66
Grubus (angl. <i>coarse</i>)	57795/46596	24	2385,6	0,25
Normalus (angl. <i>normal</i>)	125512/96432	111	2395,6	0,16

Pastaba. Tinklelio pavadinimas tai automatiškai naudoto tinklelio pavadinimas „Comsol“ programinės įrangos aplinkoje. DOF (angl. *degree of freedom*) – laisvės laipsnių skaičius, laikas – realus kompiuterio skaičiavimo laikas. Grafinis atvaizdavimas pateiktas 4 pav.

Toliau pateikiame *Model 1_a* reprezentatyviojo tūrinio elemento dydžio tyrimą. Tiriamas skirtingas tekstilės bandinio plotas, kai reprezentatyvusis tūrinis elementas sudarytas iš 1 poros (0,55 x 0,55 mm), 4 porų (1,1 x 1,1 mm), 9 porų (1,65 x 1,65 mm) ir 16 porų (2,2 x 2,2 mm) (žr. 5 pav.). Čia pora laikome oro tarpą tarp siūlų.



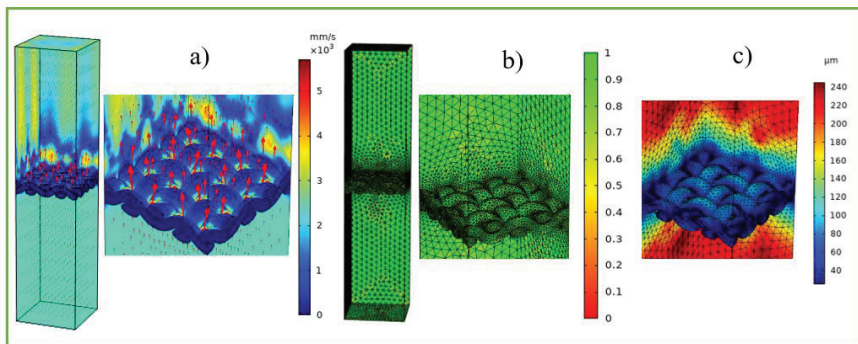
5 pav. Skirtinga *Model 1_a* tekstilės geometrija a) 1 pora, b) 4 poros, c) 9 poros, d) 16 porų

Gauti rezultatai apibendrinti 3.2 lentelėje. Visais atvejais oro laidumo koeficiento santykinė paklaida neviršijo 7 %. Analizuojant skirtingą audinio plotą, svarbu atsižvelgti į tinklelio dydį. Esant geometrijai, artimai realybei, buvo atsižvelgta į minimalią elemento kokybę, siekiant išvengti elementų, kurių minimali elemento kokybė mažesnės nei 0,01. Nustatyta, kad nėra reikšmingumo skirtumo tarp porų skaičiaus (tekstilės reprezentatyviojo tūrinio elemento dydžio). Šiame tyrime pasirinktas tekstilės reprezentatyvusis tūrinis elementas, kurį sudaro 4 poros (žr. 2.2 lentelėje). Tai buvo padaryta norint sukurti supaprastintą 3D tekstilės geometriją, įterpian tarpinius siūlus. Esant didesniam (1,5 ir 2 kartų) reprezentatyviojo tūrinio elemento dydžiui (atitinkamai 9 ir 16 porų) padidėja skaičiavimo laikas nuo 23 s iki 49 s ir 213 s atsižvelgiant į santykinę paklaidą, kuri neviršija 1 %.

3.2 lentelė. Gauti *Model 1_a* oro laidumo (AP) koeficientai esant skirtingam porų skaičiui

Pora	Tinklelis	Elementų skaičius / DOF	Minimali elementų kokybė	Vidutinė elementų kokybė	Lai- kas, s	AP, mm/s	Santykinė paklaida, %
1	Ypač grubus (angl. <i>extra coarse</i>)	8605 / 8508	0,1269	0,6221	6	2332,0	2,495
1	Grubesnis (angl. <i>coarser</i>)	19707 / 17612	0,1078	0,6437	10	2392,5	0,035
4	Grubesnis (angl. <i>coarser</i>)	39397 / 31984	0,1006	0,6484	23	2399,3	0,319
9	Grubesnis (angl. <i>coarser</i>)	52582 / 42184	0,1033	0,6434	26	2479,4	3,668
9	Grubus (angl. <i>coarse</i>)	110294 / 86000	0,1165	0,6545	49	2393,0	0,056
16	Grubus (angl. <i>coarse</i>)	124889 / 95468	0,0944	0,6523	50	2546,5	6,474
16	Normalus (angl. <i>normal</i>)	231887 / 175900	0,0951	0,6605	213	2407,2	0,649

6 pav. yra pateiktas modelio *Model 1_a* skaičiavimų pavyzdys esant 16 porų (skaičiavimo sritis 2,2 x 2,2 mm). Be to, pateiktas elementų kokybės pasiskirstymas ir tinklo elementų dydžio pasiskirstymas (ilgiausio elemento krašto ilgis) pavaizduoti b) ir c) dalyse. Oro srities tinklelį sudaro 158951 elementai, kurių minimali elementų kokybė yra 0,171, o vidutinė elementų kokybė yra 0,670, tekstilės sritis sudaryta iš 72936 elementų, kurių minimali elementų kokybė yra 0,0951, o vidutinė elementų kokybė yra 0,6399. Asimetrijos (angl. *Skewness*) kokybės matas buvo naudojamas elementų kokybei nustatyti. Ant išėjimo paviršiaus ($\partial\Omega_{outlet}$) vidutinis oro laidumo AP koeficientas yra 2407,2 mm/s.



6 pav. Modelio *Model 1_a* reprezentatyvusis tūrinis elementas esant 2,2 x 2,2 mm bandinio plotui. Oro tėkmės pasiskirstymas pateiktas a) dalyje, tinklelio kokybės pasiskirstymas b) dalyje, elementų dydžio pasiskirstymas – c) dalyje.

3.3 lentelė. Skaitinės oro laidumo (AP) koeficiento reikšmės

Modelis	Tekstilės apibūdinimas	AP, mm/s	Santykinė paklaida, %
<i>Model 1_a</i>	1 sluoksnis / struktūrinis tankis 22 / 15	2399,3	0,319
<i>Model 2_a</i>	1 sluoksnis / struktūrinis tankis 22 / 20	1645,6	4,7039
<i>Model 3_a</i>	1 sluoksnis / struktūrinis tankis 29,3 / 15	1363,8	7,5272
<i>Model 1_b</i>	2 sluoksniai / struktūrinis tankis 22 / 15	1484,5	-
<i>Model 2_b</i>	2 sluoksniai / struktūrinis tankis 22 / 20	972,34	-
<i>Model 3_b</i>	2 sluoksniai / struktūrinis tankis 29,3 / 15	778,21	-
<i>Model 1_c</i>	Supaprastintas 1sluoksnis / struktūrinis tankis 22 / 15	2385,6	0,2538
<i>Model 2_c</i>	Supaprastintas 1 sluoksnis / struktūrinis tankis 22 / 20	1613,6	2,6679
<i>Model 3_c</i>	Supaprastintas 1 sluoksnis / struktūrinis tankis 29,3 / 15	1220,3	3,7869
<i>Model 1_d</i>	Supaprastinti 2 sluoksniai / struktūrinis tankis 22 / 15	1533,8	-
<i>Model 2_d</i>	Supaprastinti 2 sluoksniai / struktūrinis tankis 22 / 20	974,14	-
<i>Model 3_d</i>	Supaprastinti 2 sluoksniai / struktūrinis tankis 29,3 / 15	706,71	-
<i>Model 1_e</i>	3D tekstilės modelis gautas iš <i>Model 1 d</i>	1522,4	-
<i>Model 2_e</i>	3D tekstilės modelis gautas iš <i>Model 2 d</i>	948,83	-
<i>Model 3_e</i>	3D tekstilės modelis gautas iš <i>Model 3 d</i>	701,49	-

3.3 lentelėje yra pateikti gauti oro laidumo (AP) koeficiento rezultatai. Atliekant skaitinius eksperimentus tekstilės struktūrų pavaizduotų 1 pav. ir aprašytų 2.2 lentelėje, realistiškos vieno sluoksnio tekstilės modelio santykinės paklaidos buvo mažesnės nei 7,53 % (žr. *Model 1_a*, *Model 2_a*, *Model 3_a*). Supaprastintos geometrijos vieno sluoksnio modelių (*Model 1_c*, *Model 2_c* ir *Model 3_c*) santykinės paklaidos buvo mažesnės nei 3,79 %. Šie rezultatai rodo gerą tikslumą palyginus su eksperimentiniais duomenimis (žr. 3.3 lentelė). Skaitiniais eksperimentais įvertintas dviejų sluoksnių oro laidumo (AP) koeficientas. Buvo gauta, kad oro laidumo (AP) koeficientas yra mažesnis nei vieno sluoksnio. Atsižvelgiant į tą patį slėgio skirtumą, oro laidumo (AP) koeficientas mažėja, kai sluoksnių skaičius didėja dėl didėjančio oro srauto pasipriešinimo per poras (oro tarpus tarp siūlų) tekstilės sluoksniuose.

Remiantis [140], oro laidumo (AP) koeficientas N-sluoksnių tekstilės sistemos gali būti randamas:

$$AP_N = \frac{AP_1}{N^{0.86}}, \quad (14)$$

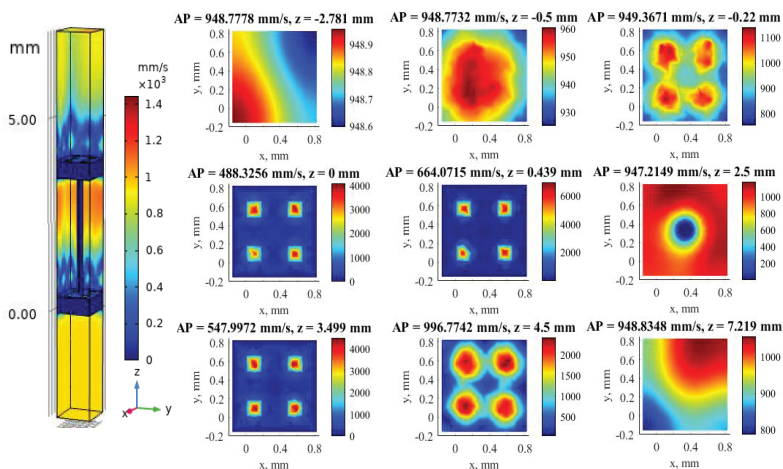
čia N – tekstilės sluoksnių skaičius, AP_1 – vieno tekstilės sluoksnio oro laidumo koeficientas. 3.4 lentelėje pateikti dviejų tekstilės sluoksnių modeliavimo oro laidumo (AP) koeficientai, AP_2 – oro laidumo koeficiento reikšmės gautos naudojant formulę (14), AP_1 reikšmė paimta iš 3.3 lentelės. *Error1* yra santykinė paklaida tarp AP_2 ir AP oro laidumo koeficientų. Be to, AP_2 oro laidumo koeficientą galime prognozuoti iš eksperimentinių duomenų, pateiktų 2.1 lentelėje. Buvo gautos tokios AP_2 oro laidumo koeficiento reikšmės 1317,70 mm/s, 865,92 mm/s ir 698,79 mm/s atitinkamai bandiniams su struktūriniu tankiu 22 / 15, 22 / 20, ir 29,3 / 15. *Error2* yra santykinė paklaida tarp AP_2 oro laidumo koeficiento, gauto iš eksperimentinių duomenų, ir mūsų gautų skaitinių oro laidumo (AP) koeficientų.

3.4 lentelė. Oro laidumo (AP) koeficiento santykinės paklaidos

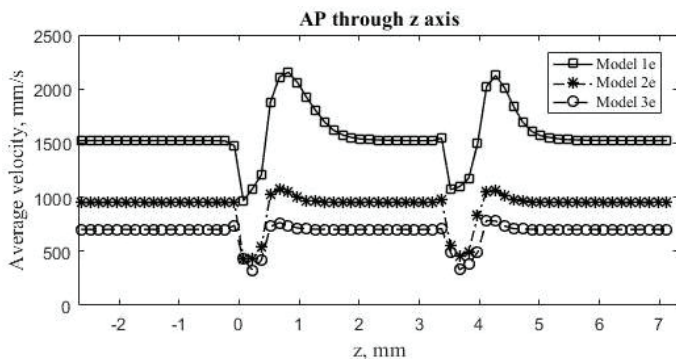
Modelis	AP, mm/s	AP ₂ , mm/s	Error1, %	Error2, %
Model 1 b	1484,50	1321,90	12,3	12,66
Model 2 b	972,34	906,65	7,25	12,29
Model 3 b	778,21	751,39	3,57	11,37
Model 1 d	1533,80	1314,35	16,70	16,40
Model 2 d	974,14	889,02	9,57	12,50
Model 3 d	706,71	672,33	5,11	1,13

Visais atvejais santykinė paklaida *Error1* yra nuo 3,57 % iki 16,70 %, o santykinė paklaida *Error2* yra nuo 1,13 % iki 16,40 %. Pagrindinė santykinė paklaidų priežastis – skirtingi geometriniai parametrai. Yra nežinoma, koks atstumas tarp tekstilės sluoksnių, porų (oro tarpai tarp siūlų) išsidėstymas kiekviename sluoksnyje. Be to, formulė (14) yra pagrįsta regresine analize, kai regresijos koeficientai randami iš riboto bandinių ir sluoksnių skaičiaus tyrimo [140]. Šios santykinės paklaidos (*Error1* ir *Error2*) yra priimtinos, jos rodo gerą skaitinių modelių tikslumą, svyruojantį nuo 83,30 % iki 98,87 %.

Tarpinio siūlo įtaką atspindi skaitiniai modeliai *Model 1_e*, *Model 2_e* ir *Model 3_e* (žr. 2.2 lentelę). Pridedant tarpinį siūlą, oro laidumo (AP) koeficientas sumažėja nuo 1533,80 mm/s iki 1522,40 mm/s, nuo 974,14 mm/s iki 948,83 mm/s ir nuo 706,71 iki 701,49 mm/s. Tai reiškia, kad atsparumas oro srautui padidėja pridėjus tarpinių siūlų. Greičio lauko pasiskirstymas per modelio *Model 2_e* aukštį pateiktas 7 pav. Vidutinis greičio srautas per 3D tekstilę yra pavaizduotas 8 pav.



7 pav. Modelio *Model 2_e* oro greičio pasiskirstymas



8 pav. 3D tekstilės vidutinės oro laidumo (AP) koeficientų reikšmės per storį

Oro laidumo (AP) koeficientų ir šiluminės elgsenos eksperimentiniai tyrimai megztų 3D tekstilės struktūrų, pagamintų iš polisterio su skirtingais biokeramikos priedais, buvo atlikti [138]. Eksperimento metu slėgio skirtumas buvo nustatytas 100 Pa. Eksperimentinės oro laidumo (AP) koeficiento reikšmės svyruoja nuo 414–641 mm/s. Bandinių storis svyravo nuo 2,6–2,7 mm. Atlikome skaitinius tyrimus, skaitiniuose modeliuose pakeitėme $\partial\Omega_{inlet}$ kraštinę sąlyga: iš 200 Pa slėgio skirtumą į 100 Pa slėgių skirtumą. Oro laidumo (AP) koeficientas sumažėjo iki 982,47 mm/s, 562,67 mm/s ir 403,71 mm/s atitinkamai modelių *Model 1_e*, *Model 2_e* ir *Model 3_e*. Tai rodo, kad modeliai *Model 2_e* ir *Model 3_e* gali būti ekvivalentūs 3D tekstilės modeliai.

3.2. Atsparumo vandens garams modelio verifikavimas ir validavimas

Skaitiniai atsparumo vandens garams (R_{et}) ir vandens garų laidumo (δ_p) koeficientų rezultatai yra pateikti 3.5 lentelėje. Buvo nustatyta, kad vandens garų atsparumo (R_{et}) koeficiento reikšmė padidėja padidinus tekstilės sluoksnių skaičių. Naudojant supaprastintą reprezentatyvųjį tūrinį elementą atsparumo vandens garams

(R_{et}) koeficiento reikšmės buvo gautos mažesnės nei realistiškos geometrijos. Visi skaitiniai modeliai parodė, kad vandens garų atsparumo koeficientas (R_{et}) yra priklausomas nuo vidinės geometrijos. Žemiausios atsparumo vandens garams koeficiento (R_{et}) reikšmės buvo gautos modeliuose, kur oro laidumo (AP) koeficientas buvo aukštesnis. Mažiausia R_{et} koeficiento reikšmė gauta pirmo bandinio su struktūriniu tankiu 22 / 15.

Atsparumo vandens garams (R_{et}) koeficiento reikšmės tiriant vieno sluoksnio tekstilės struktūras yra 1,3105–3,5904 s/m ir 0,80729–3,4658 s/m atitinkamai realistiškai ir supaprastintai geometrijai. Literatūroje [141] eksperimentiškai pamatavo austų vieno sluoksnio tekstilės bandinių atsparumo vandens garams (R_{et}) koeficientą. Buvo gauta, kad R_{et} koeficientas yra nuo 1,6067 iki 3,1477 s/m.

Analizuojant dviejų sluoksnių skaitinius modelius *Model 1_b* ir *Model 1_d* R_{et} koeficientas yra 2,6309 s/m ir 1,6443 s/m. Atsižvelgiant į Hohenšteino instituto siūlomą komforto įvertinimo sistemą (žr. 2.4 lentelę), tokia tekstilės struktūra gali būti vertinama kaip labai gera (ypač kvėpuojanti ir patogi). Modeliai *Model 2_b* ir *Model 2_d* R_{et} koeficientas yra 6,4468 s/m ir 4,0220 s/m. Tokia tekstilės struktūra gali būti priskiriama kaip labai gera (ypač kvėpuojanti ir patogi) ir gerai kvėpuojančioms klasėms. Modeliai *Model 3_b* ir *Model 3_d* R_{et} koeficientas yra atitinkamai 7,1580 s/m ir 6,9473 s/m. Šie modeliai gali būti laikomi gerai kvėpuojančiais. 3D tekstilės vandens atsparumo (R_{et}) koeficiento reikšmės yra 1,6368–6,9149 s/m. Mūsų darbe pristatyti 3D tekstilės modeliai yra sukurti iš supaprastintos geometrijos modelių (*Model 1_c*, *Model 2_c*, *Model 3_c*). Tai turėjo įtakos rezultatų skirtumams. 3D tekstilės eksperimentinė reikšmė buvo pateikta literatūroje [16], kur $R_{et}=6,36$ s/m. Modelis *Model 3_e* gerai atitinkasu eksperimentiniu vandens garų atsparumo koeficientu $R_{et}=6,36$ s/m. Be to, dviejų sluoksnių modeliai, tokie kaip *Model 2_b*, *Model 3_b* ir *Model 3_d*, gali būti laikomi priimtinais tolesniam tyrimui.

Atsparumo vandens garams skaitiniame tyrime buvo pastebėta, kad R_{et} koeficientas yra jautrus realistiškos ir supaprastintos geometrijos pakeitimams. Priežastis ta, kad šalia realistiško paviršiaus tam tikri fluido kiekiai yra įstrigę ir laikinai nejudantys. Gauti slėgio reikšmių skirtumai (realistiškos ir supaprastintos geometrijos modelių) parodo būtinybę būti labai atsargiems naudojant ir renkant supaprastintos geometrijos modelius vandens garų atsparumui tirti.

3.5 lentelė. Prognozuojamas atsparumo vandens garams (R_{et}) koeficiento reikšmės

Modelis	Sluoksnis / struktūrinis tankis	Slėgis, Pa	Vandens garų pralaidumo koef. δ_p , s/m	Vandens garų atsparumo koef. R_{et} , s/m
Model 1_a	1 / 22 / 15	61,423	2,5723E-4	1,3105
Model 2_a	1 / 22 / 20	151,48	1,0429E-4	3,2324
Model 3_a	1 / 29,3 / 15	168,34	9,3893E-5	3,5904
Model 1_b	2 / 22 / 15	120,26	1,2814E-4	2,6309
Model 2_b	2 / 22 / 20	302,21	5,2291E-5	6,4468
Model 3_b	2 / 29,3 / 15	336,24	4,7096E-5	7,1580
Model 1_c	Supaprastintas 1 / 22 / 15	37,829	4,1759E-4	0,80729
Model 2_c	Supaprastintas 1 / 22 / 20	94,366	1,6740E-4	2,0138
Model 3_c	Supaprastintas 1 / 29,3 / 15	162,41	9,7268E-4	3,4658
Model 1_d	Supaprastintas 2 / 22 / 15	77,053	2,0501E-4	1,6443
Model 2_d	Supaprastintas 2 / 22 / 20	188,47	8,3817E-5	4,0220
Model 3_d	Supaprastintas 2 / 29,3 / 15	325,56	4,8524E-5	6,9473
Model 1_e	3D tekstilė	76,761	2,0595E-4	1,6368
Model 2_e	3D tekstilė	187,43	8,4318E-5	3,9981
Model 3_e	3D tekstilė	324,03	4,8752E-5	6,9149

3.3. Šiluminio atsparumo modelio verifikavimas ir validavimas

Ekspirimentinės šiluminio atsparumo (R_{ct}) koeficiento reikšmės ir efektyviojo šiluminio laidumo (K_{eff}) koeficiento reikšmės gali būti įvertinamos pagal formules (3) ir (4). Siddiqui [137] atliko skaitinius ir eksperimentinius šiluminio atsparumo tyrimus vieno sluoksnio audinių struktūroms. Gauti rezultatai pateikti 3.6 lentelėje.

3.6 lentelė. Prognozuojami ir eksperimentiškai pamatuoti R_{ct} ir K_{eff} koeficientai [137]

Audinys	Pamatuotas R_{ct} , K·m ² /W	Pamatuotas K_{eff} , W/(m·K)	Prognozuojamas R_{ct} , K·m ² /W	Prognozuojamas K_{eff} , W/(m·K)
Nomex III	0,010000	0,05000	0,009058	0,0552
Cotton	0,008643	0,056	0,007446	0,065
Poly-viscose	0,007045	0,04840	0,006702	0,05088
F3-polyester	0,012159	0,04030	-	-
Bandinys-1 polypropylene	0,014464	0,037335	-	-
Bandinys-2 polypropylene	0,009683	0,036146	-	-

Mes pateikiame prognozuojamus bandinių 21 / 15 (*Model 1_a*) ir 29,3 / 15 (*Model 3_a*) šiluminio atsparumo (R_{ct}) ir efektyviojo šiluminio laidumo (K_{eff}) koeficientus. Skaitiniame tyrime šiluminio atsparumo (R_{ct} , K·m²/W) koeficientas,

efektyviojo šiluminio laidumo (K_{eff} , W/(m·K)) ir efektyvusis šilumos perdavimo (h_{eff} , W/(K·m²)) koeficientai randami pagal formules (15), (16), (17), čia A – skerspjūvio plotas (m²), Q – šilumos rautas (W), ΔT – temperatūros gradientas (K), h – bandinio storis (m) [97], [138].

$$R_{ct} = \frac{\Delta T}{Q/A}, \quad (15)$$

$$K_{eff} = \frac{Q \cdot h}{A \Delta T} = \frac{h}{R_{ct}}, \quad (16)$$

$$h_{eff} = \frac{1}{R_{ct}}. \quad (17)$$

„Comsol“ programinės įrangos aplinkoje formulę (15) atitinka išraiška ($aveop1(T)-aveop2(T))/aveop1(ht.nflux)$, čia $aveop1()$ ir $aveop2()$ yra vidutinės reikšmės operatoriai ant $\partial\Omega_{inlet}$ ir $\partial\Omega_{outlet}$ paviršių (žr. 3 pav.). Gauti rezultatai pateikti 3.7 ir 3.8 lentelėse. Skaitiniame tyrime analizuojamas fluidas yra oras arba drėgnas oras. Naudotos tekstilės medžiagos pateiktos 2.7 lentelėje. Temperatūrų pasiskirstymas ir tinklelio elementų dydžio pasiskirstymas pateiktas 9 pav. Buvo gauta, kad esant drėgnam orui šiluminio atsparumo (R_{ct}) koeficientas yra didesnis nei oro. Be to, efektyviojo šiluminio laidumo koeficiento (K_{eff}) reikšmės didesnės sauso oro. Mūsų gauti šiluminio atsparumo (R_{ct}) koeficiento rezultatai (3.7 lentelė ir 3.8 lentelė) gali būti palyginami su pateiktais literatūroje (3.6 lentelė). Šiluminio atsparumo (R_{ct}) koeficiento rezultatų skirtumai gali būti dėl audinio storio. Žiūrint į 3.7 ir 3.8 lenteles, esant storesniam tekstilės sluoksniui, šiluminio atsparumo (R_{ct}) koeficiento reikšmės didesnės (bandinio *Model 1_a* storis 0,439 mm, o bandinio *Model 3_a* storis 0,468 mm).

3D tekstilės skaitiniai šiluminio atsparumo tyrimai pateikti 3.9 lentelėje. Tyrimui pasirinktos polisterio (PES) ir polipropileno medžiagų savybės. 10 pav. pateiktas modelio *Model 1_e* šilumos pasiskirstymas (°C). Buvo gauta, kad didesnis šilumos atsparumas yra polipropileno negu polisterio. Efektyvusis šilumos perdavimo (h_{eff}) polipropileno buvo gautas nuo 8,36 iki 8,63 W/(K·m²) ir polisterio yra nuo 8,76 iki 9,18 W/(K·m²). Literatūroje [16] pateiktas eksperimentinis 3D tekstilės šiluminio atsparumo (R_{ct}) koeficientas 0,118 (K·m²)/W ir šilumos perdavimo h_{eff} koeficientas 8,4746 W/(K·m²). Literatūroje pateikto bandinio storis yra 7,5 mm, o mūsų skaitinio modelio apie 4 mm. Skirtingi bandinio aukščiai (t. y. atstumas tarp viršutinio ir apatinio sluoksnių), jungiamojo siūlo (siūlų) konfigūracijos, pasirinktos 3D tekstilės medžiagos savybės (3D tekstilė gali būti pagaminta iš įvairių rūšių verpalų su biokeraminiais priedais) yra pagrindinės skirtingų rezultatų priežastys.

3.7 lentelė. Skaitiškai prognozuojami bandinio 21 / 15 R_{ct} ir K_{eff} koeficientai (*Model 1a*)

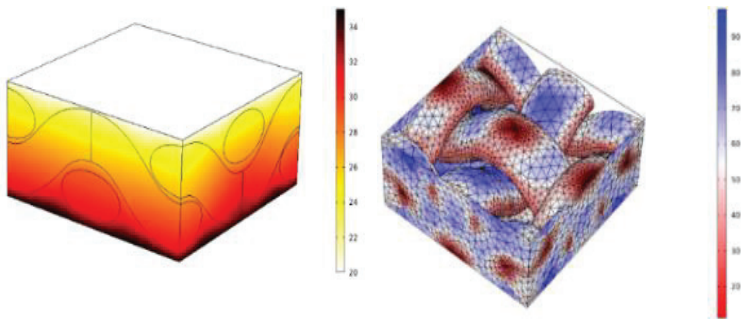
Modelis <i>Model 1a</i>	R_{ct} , K·m ² /W (oras)	K_{eff} , W/(m·K) (oras)	R_{ct} , K·m ² /W (drėgnas oras)	K_{eff} , W/(m·K) (drėgnas oras)
Nomex III	0,0089328	0,049145	0,0089585	0,049004
Medvilnė	0,0070739	0,062059	0,0070969	0,061858
Polisteris (PES)	0,0082983	0,052902	0,0083232	0,052744
Polipropilenas	0,0095373	0,046030	0,0095639	0,045902

3.8 lentelė. Skaitiškai prognozuojami R_{ct} ir K_{eff} koeficientai bandinio (*Model 3_a*)

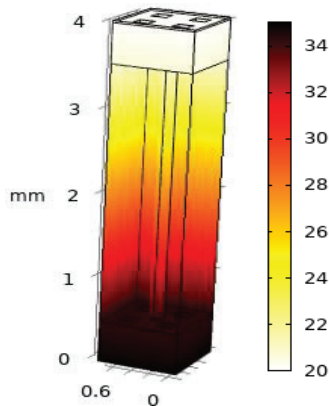
Modelis <i>Model 3a</i>	R_{ct} , K·m ² /W (oras)	K_{eff} , W/(m·K) (oras)	R_{ct} , K·m ² /W (drėgnas oras)	K_{eff} , W/(m·K) (drėgnas oras)
Nomex III	0,0092219	0,050749	0,0092472	0,050610
Medvilnė	0,0071805	0,065176	0,0072030	0,064973
Polisteris (PES)	0,0085249	0,054898	0,0085493	0,054741
Polipropilenas	0,009884	0,047328	0,0099147	0,047203

3.9 lentelė. Prognozuojamos 3D tekstilės R_{ct} ir h_{eff} koeficientų reikšmės

Modelis	R_{ct} , K·m ² /W (PES)	h_{eff} , W/(K·m ²) (PES)	R_{ct} , K·m ² /W Polipropilenas	h_{eff} , W/(K·m ²) polipropilenas
<i>Model 1e</i>	0,11419	8,7577	0,11962	8,36
<i>Model 2e</i>	0,11163	8,9582	0,11758	8,5046
<i>Model 3e</i>	0,10891	9,1815	0,11592	8,6265



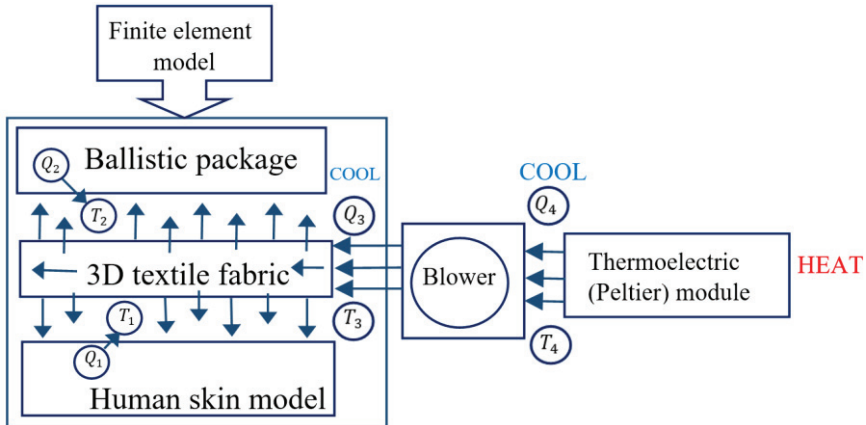
9 pav. Modelio *Model 1_a* šilumos pasiskirstymas, kai tekstilė pagaminta iš polipropileno



10 pav. Modelio *Model 1_e* šilumos pasiskirstymas, kai tekstilė pagaminta iš polipropileno

4. MODELIŲ TAIKYMAS AUDINIŲ TYRIMUI SU PAPILDOMU FUNKCIONALUMU UŽTIKRINANT DĖVĖJIMO PATOGUMĄ

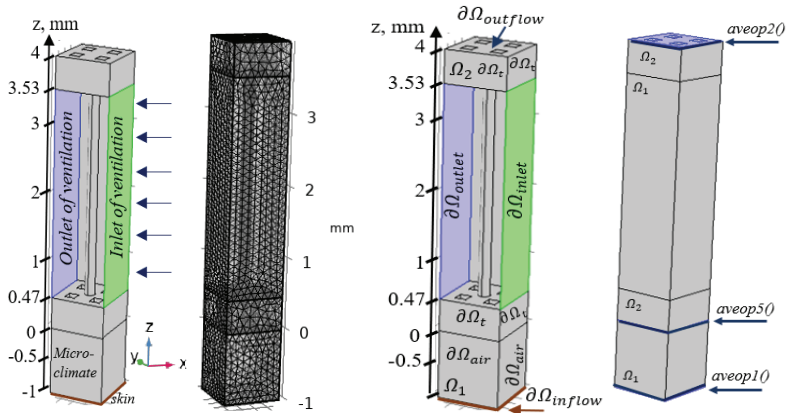
Šiame skyriuje pateiksime skaitinį modelį, kuris skirtas įvertinti priverstinės ventiliacijos (aktyvios vėsinimo sistemos) per 3D tekstilę įtaką. Tokių modeliavimų metu galima tyrinėti skirtingus efektus, tokius kaip daugiasluoksnių paketų iš tekstilės izoliacines savybes, „mikroklimato“ storio įtaką ar net šilumos ir drėgmės mainus tarp žmogaus kūno ir tekstilės struktūrų esant ekstremalioms aplinkos sąlygoms. Principinė aktyvaus vėsinimo sistemos šilumos ir drėgmės mainų schema pateikta 11 pav. [145].



11 pav. Principinė aktyvaus vėsinimo sistemos schema [145]

4.1. Priverstinės ventiliacijos per 3D tekstilę skaitinis modelis

Šiame tyrime modelio *Model 3_e* geometrija yra laikoma ekvivalenti geometrija 3D tekstilei. Atstumas tarp žmogaus kūno ir apatinio 3D tekstilės sluoksnio (mikroklimatas) – 1 mm. Reprezentatyviojo tūrinio elemento tinklelis sudarytas iš 56513 elementų, minimali elementų kokybė yra 0,22, vidutinė elementų kokybė yra 0,66. Tyrime polisterio (PES) medžiagos savybes taikome 3D tekstilės sričiai, o drėgno oro savybes (RH = 65 %, T = 20 °C) fluideo sričiai. Standartinė 10 °C temperatūra naudojama ant ventiliacijos paviršiaus. Žemiau yra pateikta reprezentatyviojo tūrinio elemento geometrija, tinklelio pavyzdys, kraštinės sąlygos ir sukurtų operatorių (*aveop1()*, *aveop2()*, *aveop(5)*) pozicijos (žr. 12 pav.).



12 pav. Priverstinės ventilacijos per 3D tekstilę skaitinis modelis

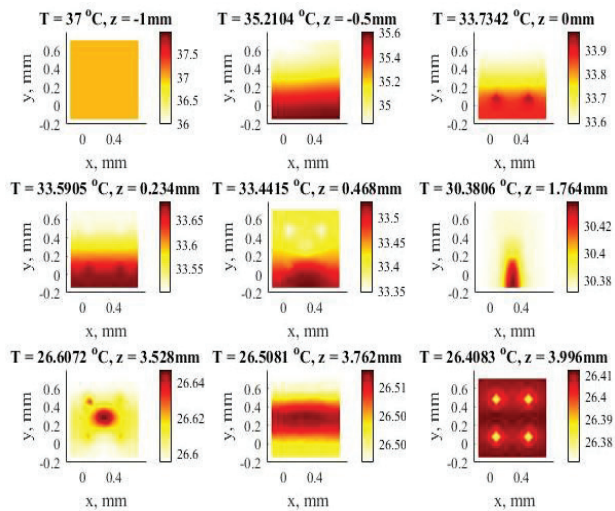
Šiame tyrime sprendžiamos Navje-Stokso (7), (8) ir šilumos (13) lygtys. Buvo daroma prielaida, kad fluido tėkmė yra laminarinė nespūdi. Skaitiniame modelyje naudotos kraštinės sąlygos pateiktos 4.1 lentelėje ir pavaizduotos 12 pav. Įeinantis masės srautas ant ventilacijos paviršiaus yra 0 dm³/min (nėra ventilacijos), 0,2 dm³/min ir 0,8 dm³/min.

4.1 lentelė. Priverstinės ventilacijos modelio kraštinės sąlygos

Kraštinė	Fluid flow (.spf) sąsaja	Apibūdinimas [123]
$\partial\Omega_{inlet}$	$-\int_{\partial\Omega} \frac{\rho}{\rho_{st}} (\mathbf{u} \cdot \mathbf{n}) d_{bc} dS = Q_{sv}$ Q_{sv} – standartinis masės srautas 0, 0,2 ir 0,8 dm ³ /min.	Inlet (mass flow rate). Fluido sričiai d_{bc} yra kraštinės storis, standartinis tankis $\rho_{st} = \frac{p_{st} \cdot M_n}{R \cdot T_{st}}$. Tyrime $T_{st} = 10$ °C, M_n – fluido molinė masė (0,032 kg/mol), R – universalioji molinė dujų konstanta, p_s – standartinis slėgis 1[atm].
$\partial\Omega_{outlet}$	$[-p\mathbf{I} + \mathbf{K}]\mathbf{n} = -\hat{p}_0\mathbf{n}$ $\hat{p}_0 \leq p_0$, $\mathbf{K} = \mu(\nabla\mathbf{u} + (\nabla\mathbf{u})^T)$ $p_0 = 0\text{Pa}$	Outlet. Ant fluido srauto išėjimo kraštinės $\partial\Omega_{outlet}$ nustatytas slėgis $p_0 = 0\text{Pa}$. Fizikinė reikšmė, kad absoliutus slėgis lygus santykiniam slėgiui (1[atm]).
$\partial\Omega_{air}$	$\mathbf{u} \cdot \mathbf{n} = 0$ $\mathbf{K}_n - (\mathbf{K}_n \cdot \mathbf{n})\mathbf{n} = 0$, $\mathbf{K}_n = \mathbf{K}\mathbf{n}$	Wall. Sienos sąlyga slip naudojama ant kraštinių $\partial\Omega_{air}$.
Kraštinė	Heat flow (.ht) sąsaja	
$\partial\Omega_{inflow}$	$T = 37$ °C	Temperature. Įeinanti temperatūra yra pastovi ($T = 37$ °C) ir yra nustatyta ant imituojamo odos paviršiaus.
$\partial\Omega_{outflow}$	$-\mathbf{n} \cdot \mathbf{q} = q_0$ $q_0 = h(T_{ext} - T)$	Heat flux. Šilumos perdavimo koeficientas $h=9,1815$ W/(K·m ²) parinktas iš 3.9 lentelės. Aplinkos temperatūra $T_{ext} = 20$ °C.
$\partial\Omega_t, \partial\Omega_{air}$	$-\mathbf{n} \cdot \mathbf{q} = 0$	Thermal insulation. Ant išorinių kraštinių nėra šiluminio srauto.

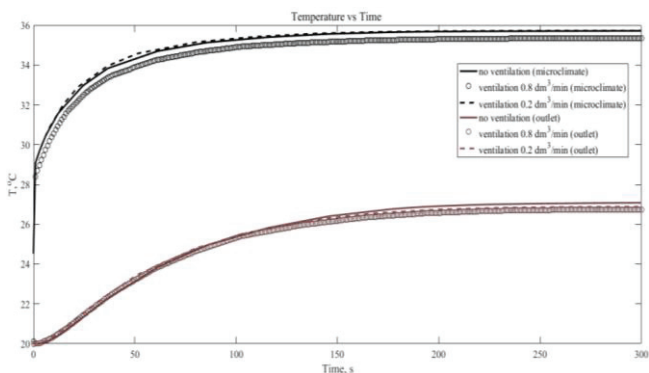
4.2. Šilumos ir masės mainų skaitinis tyrimas esant priverstinei ventiliacijai per 3D tekstilę

Šiuose skaitiniuose eksperimentuose analizuojami skirtingi įeinantys masės srautai 0, 0,2 ir 0,8 dm³/min, kurie yra nustatyti ant ventiliacijos paviršiaus $\partial\Omega_{\text{inlet}}$ (žr. 12 pav.). Temperatūros pasiskirstymas per 3D tekstilę atsižvelgiant į masės srautą 0,8 dm³/min pavaizduotas 13 pav. Vidutinė paviršiaus temperatūra T °C ir pozicija ant z ašies (x ir y pozicijos yra fiksuotos) yra pateiktos prie temperatūros pasiskirstymo. Skaitiniuose eksperimentuose ‘mikroklimatą’ atitinka z = -0,5 mm pozicija (žr. 12 pav.). Esant ventiliacijos masės srautui 0 dm³/min (nėra ventiliacijos) temperatūra yra T = 35,72 °C, o esant ventiliacijos masės srautui 0,8 dm³/min temperatūra yra T = 35,21 °C. Nustatyta, kad padidinus įeinantį masės srautą temperatūra sumažėja.



13 pav. Temperatūros pasiskirstymas esant masės srautui 0,8 dm³/min

Temperatūros pokyčiai kintant laikui pavaizduoti 14 pav. Pavaizduota vidutinė „mikroklimato“ (z = -0,5 mm padėtis) ir išėjimo paviršiaus (z = -3,996 mm padėtis) temperatūra. „Mikroklimato“ paviršiuje temperatūros skirtumai labai maži (beveik jų nėra), kai nėra ventiliacijos ir kai ventiliacijos masės srautas yra labai mažas $Q_{sv} = 0,2$ dm³/min.



14 pav. Temperatūros ir laiko sąsaja esant skirtingam ventiliacijos srautui

Skaitiniu modeliu galime nustatyti efektyvųjį šilumos perdavimo koeficientą. Norint įvertinti šiluminio perdavimo koeficientą skirtingose bandinio vietose, buvo sukurti paviršiaus vidutinės reikšmės operatoriai $aveop1()$, $aveop2()$, ir $aveop3()$ (žr. 12 pav.). Nustatytos efektyviojo šilumos perdavimo koeficiento reikšmės pateiktos 4.2 lentelėje. Čia $h_{microlayer}$ yra efektyvusis šilumos perdavimo koeficientas tarp odos ir apatinio tekstilės sluoksnio. Jis gali būti randamas pagal išraišką $aveop1(ht.ntflux)/(aveop1(T)-aveop5(T))$. Efektyvusis šilumos perdavimo h_{inside} koeficientas skaičiuojamas tarp apatinio ir viršutinio tekstilės sluoksnio $aveop5(ht.ntflux)/(aveop5(T)-aveop2(T))$. Efektyvusis šilumos perdavimo h_{total} koeficientas tarp odos ir viršutinio 3D tekstilės sluoksnio randamas pagal $aveop1(ht.ntflux)/(aveop1(T)-aveop2(T))$.

Buvo nustatyta, kad padidinus masės srautą padidėja šilumos perdavimo koeficientai (t.y. šiluminis atsparumas su mažėja).

4.2 lentelė. Prognozuojamo efektyviojo šiluminio koeficiento reikšmės

Masės srautas Q_{sv}	$h_{microlayer}$, W/(K·m ²)	h_{inside} , W/(K·m ²)	h_{total} , W/(K·m ²)
Nėra ventiliacijos (0 dm ³ /min)	25,63	9,51	6,64
0,2 dm ³ /min	25,75	9,68	6,78
0,8 dm ³ /min	29,08	11,87	8,98

IŠVADOS

Šiame darbe buvo sukurti baigtinių elementų modeliai, imituojuantys eksperimentinius oro laidumo, atsparumo vandens garams ir šiluminio atsparumo matavimus. Buvo prognozuojami oro laidumo, atsparumo vandens garams, vandens garų perdavimo, šiluminio atsparumo, šilumos laidumo ir šilumos perdavimo koeficientai. Norint įvertinti oro laidumo, vandens garų atsparumo ir vandens garų perdavimo koeficientus buvo sukurta 15 skirtingų geometrijos modelių, apimančių vieno sluoksnio, dviejų sluoksnių ir 3D tekstilės modelius. Atliekant šiluminio atsparumo modeliavimą, buvo naudojami reprezentatyvieji tūriniai elementai vieno

sluoksnio, artimo realiai geometrijai, ir 3D tekstilės modeliai darant prielaidą, kad tekstilė yra pagaminta iš „Nomex III“, medvilnės, poliesterio (PES) ir polipropileno. Siūlomi modeliai buvo gan tikslūs lyginant su eksperimentiniais matavimais, aprašytais literatūroje. Be to, tyrimas buvo pratęstas siekiant prognozuoti vėdinimo temperatūrą ir šilumos perdavimo koeficientus. Po teorinio tyrimo padarytos pagrindinės išvados:

1. Skaitiniai oro laidumo modeliai parodė, kad nėra reikšmingo skirtumo tarp oro laidumo koeficiento ir skirtingo reprezentatyviojo tūrinio elemento dydžio. Tačiau reikėtų atsižvelgti į tinkamą tinklelio parinkimą. Konvergavimo analizė leido sumažinti modeliavimo laiką nustatant optimalų porų dydį, atsižvelgiant į priimtinas santykinės paklaidas tarp eksperimentinių duomenų ir prognozuojamų oro laidumo koeficientų.

2. Oro laidumo koeficientų santykinės paklaidos neviršijo 1 %, 5 % ir 8 % atitinkamai vieno sluoksnio konstrukcijoms, kurių struktūrinis tankis yra 22 / 15, 22 / 20 ir 29,3 / 15.

3. Santykinės dviejų sluoksnių tekstilės oro laidumo paklaidos svyruoja nuo 3,57 % iki 16,70 %. Santykinių paklaidų priežastys: nežinomas atstumas tarp sluoksnių (oro tarpas), porų (oro tarpai tarp siūlų) išsidėstymas kiekviename sluoksnyje. Be to, analitinis modelis, kuris buvo naudojamas palyginti oro laidumo vertėms, yra susijęs su eksperimentiniais matavimais, kur eksperimentų skaičius yra ribotas ir kurie apima skirtingą bandinių geometriją.

4. Skaitiniai atsparumo vandens garams eksperimentai parodė jautrumą skirtingai reprezentatyviojo tūrinio elemento geometrijai. Modeliuojant tekstilę buvo pakeista geometrija iš realistiškos į supaprastintą. Pagrindinė jautrumo priežastis buvo gauti skirtingi slėgiai. Modeliuojant atsparumą vandens garams, renkantis (ir naudojant) supaprastintą reprezentatyviojo tūrinio elemento geometriją reikia atkreipti dėmesį į jautrumą pasikeitusiai geometrijai.

5. Atlikti skaitiniai šiluminio atsparumo eksperimentai, esant prielaidai, kad šilumos mainai vyksta dėl laidumo. Vieno sluoksnio struktūrų skaitiniai eksperimentai buvo palyginti su literatūroje rasta matavimais ir ir palyginti tiksliai atitiko.

6. Skaitinis tyrimas buvo pratęstas, sukuriant vėdinimo modelį. Vėdinimo modelis parodė, kad padidinus masės srautą ant ventiliacijos kraštinės sąlygos ($\partial\Omega_{\text{inlet}}$), 3D tekstilės šiluminis atsparumas sumažėjo. Sukurtas vėdinimo modelis yra validus esant mažiems masės srautams.

REFERENCES

- [1] J. W. S. Hearle, "Introduction," in *Advances in 3D Textiles*, TexEng Software Ltd, Manchester, UK, 2015, pp. 1–18.
- [2] A. Gugliuzza and E. Drioli, "A review on membrane engineering for innovation in wearable fabrics and protective textiles," *Journal of Membrane Science*, vol. 446, pp. 350–375, 2013.
- [3] A. Yu, K. L. Yick, S. P. Ng, and J. Yip, "Orthopaedic textile inserts for pressure treatment of hypertrophic scars," *Textile Research Journal*, vol. 86, no. 14, pp. 1549–1562, 2016.
- [4] A. Dixit and H. S. Mali, "Modeling techniques for predicting the mechanical properties of woven-fabric textile composites: A Review," *Mechanics of Composite Materials*, vol. 49, no. 1, pp. 1–20, 2013.
- [5] N. D. Ngo and K. K. Tamma, "Microscale permeability predictions of porous fibrous media," *International Journal of Heat and Mass Transfer*, vol. 44, no. 16, pp. 3135–3145, 2001.
- [6] P. Wang, X. Legrand, and D. Soulat, *Three-Dimensional Textile Preform Using Advanced Textile Technologies for Composite Manufacturing*. 2017.
- [7] R. Kamiya, B. A. Cheeseman, P. Popper, and T. W. Chou, "Some recent advances in the fabrication and design of three-dimensional textile preforms: A review," *Composites Science and Technology*, vol. 60, no. 1, pp. 33–47, 2000.
- [8] Ž. Zupin, A. Hladnik, and K. Dimitrovski, "Prediction of one-layer woven fabrics air permeability using porosity parameters," *Textile Research Journal*, vol. 82, no. 2, pp. 117–128, 2011.
- [9] A. Pezzin, "Thermo-physiological comfort modelling of fabrics and garments. PhD thesis,," 2015.
- [10] E. Kumpikaitė and V. Milašius, "Analysis of Interrelation between Fabric Structure Factors and Beat-up Parameters," *Materials Science (MEDZIAGOTYRA)*, vol. 9, no. 2, pp. 228–232, 2003.
- [11] S. K. Mazumdar, *Composites manufacturing. Materials, Product, and Process Engineering*. CRC Press LLC, 2002.
- [12] A. J. Thompson, B. El Said, D. Ivanov, J. P. H. Belnoue, and S. R. Hallett, "High fidelity modelling of the compression behaviour of 2D woven fabrics," *International Journal of Solids and Structures*, vol. 154, no. July, pp. 104–113, 2018.
- [13] F. Çeken, Ö. Kayacan, A. Özkurt, and Ş. S. Uğurlu, "The electromagnetic shielding properties of some conductive knitted fabrics produced on single or double needle bed of a flat knitting machine," *Journal of the Textile Institute*, vol. 103, no. 9, pp. 968–979, 2012.
- [14] S. Martin, "Geometric and Mechanical Modelling of Textiles. PhD thesis,," University of Nottingham, 2007.
- [15] M. S. Santos, D. Oliveira, J. B. L. M. Campos, and T. S. Mayor, "Numerical analysis of the flow and heat transfer in cylindrical clothing microclimates – Influence of the microclimate thickness ratio," *International Journal of Heat and Mass Transfer*, vol. 117, pp. 71–79, 2018.
- [16] R. Barauskas and A. Abraitienė, "A model for numerical simulation of heat and water

- vapor exchange in multilayer textile packages with three-dimensional spacer fabric ventilation layer,” *Textile Research Journal*, vol. 81, no. 12, pp. 1195–1215, 2011.
- [17] Y. Li, “The science of clothing comfort,” *Textile Progress*, vol. 31, no. 1–2, pp. 1–135, 2001.
- [18] D. Tessier, *Testing thermal properties of textiles*. Elsevier Ltd., 2017.
- [19] E. Saldaeva, “Through thickness air permeability and thermal conductivity analysis for textile materials. PhD thesis,.” The University of Nottingham, 2010.
- [20] M. Umair, T. Hussain, K. Shaker, Y. Nawab, M. Maqsood, and M. Jabbar, “Effect of woven fabric structure on the air permeability and moisture management properties,” *Journal of the Textile Institute*, vol. 107, no. 5, pp. 596–605, 2016.
- [21] “Textiles - Determination of permeability of fabrics to air (EN ISO 9237:1995),” 1995.
- [22] “ISO 11092:2014(en) Textiles — Physiological effects — Measurement of thermal and water-vapour resistance under steady-state conditions (sweating guarded-hotplate test).” [Online]. Available: <https://www.iso.org/obp/ui/#iso:std:iso:11092:ed-2:v1:en>.
- [23] A. E. Mangat, L. Hes, V. Bajzik, and A. Mazari, “Thermal Absorptivity Model of Knitted Rib Fabric and its Experimental Verification,” *Autex Research Journal*, vol. 18, no. 1, pp. 20–27, 2017.
- [24] L. Hes, M. de Araujo, and V. V. Djulay, “Effect of Mutual Bonding of Textile Layers on Thermal Insulation and Thermal Contact Properties of Fabric Assemblies,” *Textile Research Journal*, vol. 66, no. 4, pp. 245–250, 1996.
- [25] G. D. Ingram, I. T. Cameron, and K. M. Hangos, “Classification and analysis of integrating frameworks in multiscale modelling,” *Chemical Engineering Science*, vol. 59, no. 11, pp. 2171–2187, 2004.
- [26] E. Weinan, *Principles of Multiscale Modeling*. 2011.
- [27] X. Liu, D. Furrer, J. Koster, and J. Holmes, *Vision 2040 : A Roadmap for Integrated , Multiscale Modeling and Simulation of Materials and Systems*. 2018.
- [28] F. V. Souza, D. H. Allen, and Y. R. Kim, “Multiscale model for predicting damage evolution in composites due to impact loading,” *Composites Science and Technology*, vol. 68, no. 13, pp. 2624–2634, 2008.
- [29] J. K. Marzinek, R. G. Huber, and P. J. Bond, “Multiscale modelling and simulation of viruses,” *Current Opinion in Structural Biology*, vol. 61, pp. 146–152, 2020.
- [30] M. Auf der Maur, “Multiscale approaches for the simulation of optoelectronic devices,” *Journal of Green Engineering*, vol. 5, no. 3–4, pp. 133–155, 2016.
- [31] D. Calneryte and R. Barauskas, “Multi-scale evaluation of the linear elastic and failure parameters of the unidirectional laminated textiles with application to transverse impact simulation,” *Composite Structures*, vol. 142, pp. 325–334, 2016.
- [32] M. Aihua, L. Jie, L. Guiqing, and L. Yi, “Numerical simulation of multiscale heat and moisture transfer in the thermal smart clothing system,” *Applied Mathematical Modelling*, vol. 40, no. 4, pp. 3342–3364, 2015.
- [33] C. Geerling, M. Azimian, A. Wiegmann, H. Briesen, and M. Kuhn, “Designing optimally-graded depth filter media using a novel multiscale method,” *AIChE Journal*, vol. 66, no. 2, pp. 1–12, 2019.
- [34] B. Stier, J. W. Simon, and S. Reese, “Numerical and experimental investigation of the structural behavior of a carbon fiber reinforced ankle-foot orthosis,” *Medical*

- Engineering and Physics*, vol. 37, no. 5, pp. 505–511, 2015.
- [35] T. Y. Chao and W. K. Chow, “a Review on the Applications of Finite Element Method To Heat Transfer and Fluid Flow,” *International Journal on Architectural Science*, vol. 3, no. 1, pp. 1–19, 2002.
- [36] A. Hrennikoff, “Solution of problems of elasticity by the framework method,” *Journal of Applied Mechanics*, vol. 8, no. 4, pp. 169–175, 1941.
- [37] D. McHenry, “A lattice analogy for the solution of plane stress problems,” *Journal of the Institute of Civil Engineers*, vol. 21, no. 2, pp. 59–82, 1943.
- [38] R. Courant, “Variational methods for the solution of problems of equilibrium and vibrations,” *Bulletin of the American Mathematical Society*, vol. 49, no. 1, pp. 1–23, 1943.
- [39] A. J. Davies, *The Finite Element Method An Introduction with Partial Differential Equations*, Second Edi. Oxford University Press Inc., New York, 2011.
- [40] M. Turner, R. Clough, H. Martin, and J. Topp, “Stiffness and deflection analysis of complex structures,” *Journal of The Aeronautical sciences*, vol. 53, no. 9, pp. 805–823, 1956.
- [41] R. W. Clough, “The finite element in plane stress analysis,” *Proc. 2nd A.S.C.E. Conf. on Electronic Computation, Pittsburgh, Pennsylvania*, pp. 345–378, 1960.
- [42] H. C. Martin, *Introduction to Matrix Methods of Structural Analysis*. Published by McGraw-Hill Inc, New York, 1966.
- [43] L. Sabat and C. K. Kundu, “History of Finite Element Method: A Review,” in *Recent Developments in Sustainable Infrastructure. Lecture Notes in Civil Engineering.*, S. P. Das B., Barbhuiya S., Gupta R., Ed. Springer, Singapore, 2021, pp. 395–404.
- [44] J. H. Argyris, S. Kelsey, and H. Kamel, “Matrix Methods of Structural Analysis-A Precip of Recent Development,” in *AGARDograph 72. Matrix Methods of Structural Analysis*, B. Fraeijs de Veubeke, Ed. Pergamon Press, London, 1964, pp. 3–164.
- [45] J. Argyris and R. Kačianauskas, “Semi-analytical finite elements in the higher-order theory of beams,” *Computer Methods in Applied Mechanics and Engineering*, vol. 138, no. 1–4, pp. 19–72, 1996.
- [46] Zienkiewicz, O.C. and Cheung, Y.K., *The Finite Element Method In Structural and Continuum Mechanics*. McGraw-Hill, London, 1967.
- [47] O. C. Zienkiewicz, R. L. Taylor, and J. Z. Zhu, *The Finite Element Method: Its Basis & Fundamentals*, 7th ed. Butterworth-Heinemann is an imprint of Elsevier, 2013.
- [48] O. C. Zienkiewicz, R. L. Taylor, and P. Nithiarasu, *The Finite Element Method for Fluid Dynamics*, 6th ed. Amsterdam: Elsevier, 2005.
- [49] P. Nithiarasu and O. C. Zienkiewicz, “The Finite Element Method for Heat and Fluid Flow,” *International Heat Transfer Conference 13, 13-18 August, Sydney, Australia*, p. 17, 2006.
- [50] Udayraj, P. Talukdar, A. Das, and R. Alagirusamy, “Heat and mass transfer through thermal protective clothing - A review,” *International Journal of Thermal Sciences*, vol. 106, pp. 32–56, 2016.
- [51] R. W. Lewis, P. Nithiarasu, and K. N. Seetharamu, *Fundamentals of the Finite Element Method for Heat and Fluid Flow*. The Atrium, Southern Gate, Chichester, West Sussex PO19 8SQ, England: John Wiley & Sons Ltd, 2004.

- [52] S. Cimilli, F. B. U. Nergis, and C. Candan, "Modeling of Heat Transfer Measurement Unit for Cotton Plain Knitted Fabric using a Finite Element Method," *Textile Research Journal*, vol. 78, no. 1, pp. 53–59, 2008.
- [53] R. A. Angelova, M. Kyosov, and P. Stankov, "Numerical investigation of the heat transfer through woven textiles by the jet system theory," *Journal of the Textile Institute*, vol. 110, no. 3, pp. 386–395, 2019.
- [54] A. K. Puszkarz, R. Korycki, and I. Krucinska, "Simulations of heat transport phenomena in a three-dimensional model of knitted fabric," *Autex Research Journal*, vol. 16, no. 3, pp. 128–137, 2016.
- [55] A. K. Puszkarz, W. Machnowski, and A. Błasińska, "Modeling of thermal performance of multilayer protective clothing exposed to radiant heat," *Heat and Mass Transfer/Waerme- und Stoffuebertragung*, 2020.
- [56] A. K. Puszkarz and W. Machnowski, "Simulations of Heat Transfer through Multilayer Protective Clothing Exposed to Flame," *Autex Research Journal*, no. September, 2020.
- [57] R. Barauskas, A. Sankauskaite, V. Rubeziene, A. Gadeikyte, V. Skurkyte-Papieviene, and A. Abraitiene, "Investigation of thermal properties of spacer fabrics with phase changing material by finite element model and experiment," *Textile Research Journal*, 2020.
- [58] K. Iqbal, D. Sun, G. K. Stylios, T. Lim, and D. W. Corne, "FE analysis of thermal properties of woven fabric constructed by yarn incorporated with microencapsulated phase change materials," *Fibers and Polymers*, vol. 16, no. 11, pp. 2497–2503, 2015.
- [59] M. O. R. Siddiqui and D. Sun, "Computational analysis of effective thermal conductivity of microencapsulated phase change material coated composite fabrics," *Journal of Composite Materials*, vol. 49, no. 19, pp. 2337–2348, 2015.
- [60] M. O. R. Siddiqui and D. Sun, "Finite element analysis of thermal conductivity and thermal resistance behaviour of woven fabric," *Computational Materials Science*, vol. 75, pp. 45–51, 2013.
- [61] H. Phelps and H. Sidhu, "A mathematical model for heat transfer in fire fighting suits containing phase change materials," *Fire Safety Journal*, vol. 74, pp. 43–47, 2015.
- [62] A. Fonseca, T. S. Mayor, and J. B. L. M. Campos, "Guidelines for the specification of a PCM layer in firefighting protective clothing ensembles," *Applied Thermal Engineering*, vol. 133, no. February, pp. 81–96, 2018.
- [63] M. Venkataraman, R. Mishra, J. Militky, and B. K. Behera, "Modelling and simulation of heat transfer by convection in aerogel treated nonwovens," *Journal of the Textile Institute*, vol. 108, no. 8, pp. 1442–1453, 2017.
- [64] R. Degrave, J. Moreau, A. Cockx, and P. Schmitz, "Multiscale analysis and modelling of fluid flow within a photocatalytic textile," *Chemical Engineering Science*, vol. 130, pp. 264–274, 2015.
- [65] R. Degrave, A. Cockx, and P. Schmitz, "Model of Reactive Transport within a Light Photocatalytic Textile," *International Journal of Chemical Reactor Engineering*, vol. 14, no. 1, pp. 269–281, 2016.
- [66] M. Havlova, "Air permeability, water vapour permeability and selected structural parameters of woven fabrics," *Vlakna a Textil*, vol. 27, no. 1, pp. 12–18, 2020.
- [67] G. Zhu, Y. Fang, L. Zhao, J. Wang, and W. Chen, "Prediction of structural parameters

- and air permeability of cotton woven fabric,” *Textile Research Journal*, vol. 88, no. 14, pp. 1650–1659, 2017.
- [68] R. T. Ogulata and S. Mavruz, “Investigation of porosity and air permeability values of plain knitted fabrics,” *Fibres and Textiles in Eastern Europe*, vol. 82, no. 5, pp. 71–75, 2010.
- [69] M. Karaki, “Permeability modeling of engineering textiles used in composite materials,” Université de Technologie de Troyes, 2017.
- [70] G. O. Brown, “Henry Darcy and the making of a law,” *Water Resources Research*, vol. 38, no. 7, pp. 11-1-11-12, 2002.
- [71] A. V. Kulichenko, “Theoretical analysis, calculation, and prediction of the air permeability of textiles,” *Fibre Chemistry*, vol. 37, no. 5, pp. 371–380, 2005.
- [72] X. Xiao, X. Zeng, A. Long, H. Lin, M. Clifford, and E. Saldaeva, “An analytical model for through-thickness permeability of woven fabric,” *Textile Research Journal*, vol. 82, no. 5, pp. 492–501, 2012.
- [73] S. Sharma and D. A. Siginer, “Permeability measurement methods in porous media of fiber reinforced composites,” *Applied Mechanics Reviews*, vol. 63, no. 2, pp. 1–19, 2010.
- [74] J. . Holman, *Heat Transfer*, Sixth edit. McGraw-Hill, Inc., 1986.
- [75] P. Pettersson, T. S. Lundström, and T. Wikström, “A method to measure the permeability of dry fiber mats,” *Wood and Fiber Science*, vol. 38, no. 3, pp. 417–426, 2006.
- [76] G. Zhu, D. Kremenakova, Y. Wang, and J. Militky, “Air permeability of polyester nonwoven fabrics,” *Autex Research Journal*, vol. 15, no. 1, pp. 8–12, 2015.
- [77] G. E. r. Lamb and P. A. Costanza, “Influences of Fiber Geometry on the Performance of Nonwoven Air Filters: Part III: Cross-Sectional Shape,” *Textile Research Journal*, vol. 50, no. 6, pp. 362–370, 1980.
- [78] V. K. Kothari and A. Newton, “61—The air-permeability of non-woven fabrics,” *Journal of the Textile Institute*, vol. 65, no. 10, pp. 525–531, 1974.
- [79] G. Xu and F. Wang, “Prediction of the permeability of woven fabrics,” *Journal of Industrial Textiles*, vol. 34, no. 4, pp. 243–254, 2005.
- [80] P. C. Carman, *Flow of Gases Through Porous Media*. London: Butterworths Scientific Publications, 1956.
- [81] B. R. Gebart, “Permeability of Unidirectional Reinforcements for RTM,” *Journal of Composite Materials*, vol. 26, no. 8, pp. 1100–1133, 1992.
- [82] P. Xu and B. Yu, “Developing a new form of permeability and Kozeny-Carman constant for homogeneous porous media by means of fractal geometry,” *Advances in Water Resources*, vol. 31, no. 1, pp. 74–81, 2008.
- [83] S. Mezarciöz, S. Mezarciöz, and R. T. Oğulata, “Prediction of air permeability of knitted fabrics by means of Computational Fluid Dynamics,” *Tekstil ve Konfeksiyon*, vol. 24, no. 2, pp. 202–211, 2014.
- [84] Q. Zhu and Y. Li, “Effects of pore size distribution and fiber diameter on the coupled heat and liquid moisture transfer in porous textiles,” *International Journal of Heat and Mass Transfer*, vol. 46, no. 26, pp. 5099–5111, 2003.
- [85] A. Cay, S. Vassiliadis, and C. Provatidis, “Prediction of the Air Permeability of Woven

- Fabrics using a Modified Kozeny- Carman Relationship,” *Applied research review. Journal of the Technological Education Institute of Piraeus*, vol. Vol. XI, no. No 1, pp. 151–159, 2006.
- [86] B. Verleye, “Computation of the permeability of multi-scale porous media with application to technical textiles,” K.U.Leuven, Departement Computerwetenschappen Celestijnenlaan 200A, B-3001 Leuven, Belgi, 2008.
- [87] M. Parada, X. Zhou, D. Derome, R. M. Rossi, and J. Carmeliet, “Modeling wicking in textiles using the dual porosity approach,” *Textile Research Journal*, vol. 89, no. 17, pp. 3519–3528, 2019.
- [88] M. Nordlund and T. S. Lundström, “Effect of multi-scale porosity in local permeability modelling of non-crimp fabrics,” *Transport in Porous Media*, vol. 73, no. 1, pp. 109–124, 2008.
- [89] B. Verleye, M. Klitz, R. Croce, D. Roose, S. V. Lomov, and I. Verpoest, “Computation of permeability of textile with experimental validation for monofilament and non crimp fabrics,” *Studies in Computational Intelligence*, vol. 55, no. 1, pp. 93–109, 2007.
- [90] A. L. Berdichevsky and Z. Cai, “Preform permeability predictions by self-consistent method and finite element simulation,” *Polymer Composites*, vol. 14, no. 2, pp. 132–143, 1993.
- [91] F. R. Phelan and G. Wise, “Analysis of transverse flow in aligned fibrous porous media,” *Composites Part A: Applied Science and Manufacturing*, vol. 27, no. 1, pp. 25–34, 1996.
- [92] A. Geoffre, Y. Wielhorski, N. Moulin, J. Bruchon, S. Drapier, and P. J. Liotier, “Influence of intra-yarn flows on whole 3D woven fabric numerical permeability: from Stokes to Stokes-Darcy simulations,” *International Journal of Multiphase Flow*, vol. 129, 2020.
- [93] S. S. H. Dehkordi, M. Ghane, S. B. Abdellahi, and M. B. Soultanzadeh, “Numerical modeling of the air permeability of knitted fabric using computational fluid dynamics (CFD) method,” *Fibers and Polymers*, vol. 18, no. 9, pp. 1804–1809, 2017.
- [94] R. A. Angelova, P. Stankov, I. Simova, and I. Aragon, “Three dimensional simulation of air permeability of single layer woven structures,” *Central European Journal of Engineering*, vol. 1, no. 4, pp. 430–435, 2011.
- [95] A. K. Puszkarz and I. Krucińska, “Modeling of Air Permeability of Knitted Fabric Using the Computational Fluid Dynamics,” *Autex Research Journal*, vol. 18, no. 4, pp. 364–376, 2018.
- [96] H. Gidik, O. Vololonirina, R. M. Ghantous, and A. Ankou, “Impact of test parameters on the water vapor permeability of textiles,” *International Journal of Clothing Science and Technology*, vol. 31, no. 3, pp. 350–361, 2019.
- [97] M. O. R. Siddiqui and D. Sun, “Conjugate heat transfer analysis of knitted fabric,” *Journal of Thermal Analysis and Calorimetry*, vol. 129, no. 1, pp. 209–219, 2017.
- [98] J. Wang, J. K. Carson, M. F. North, and D. J. Cleland, “A new structural model of effective thermal conductivity for heterogeneous materials with co-continuous phases,” *International Journal of Heat and Mass Transfer*, vol. 51, no. 9–10, pp. 2389–2397, 2008.
- [99] J. Militky and D. Kremenakova, “Selected topics of textile and material science,” in *Thermal Conductivity prediction of textile materials*, D. Kremenakova, R. Mishra, J.

- Militky, and J. Šestak, Eds. Liberec: Publishing House of WBU, Pilsen, 2011, pp. 368–375.
- [100] T. Dias and G. B. Delkumburewatte, “The influence of moisture content on the thermal conductivity of a knitted structure,” *Measurement Science and Technology*, vol. 18, no. 5, pp. 1304–1314, 2007.
- [101] A. Das, R. Alagirusamy, K. Shabaridharan, and P. Kumar, “Study on heat transmission through multilayer clothing assemblies under different convective modes,” *Journal of the Textile Institute*, vol. 103, no. 7, pp. 777–786, Jul. 2012.
- [102] R. T. Oğulata, “The effect of thermal insulation of clothing on human thermal comfort,” *Fibres and Textiles in Eastern Europe*, vol. 15, no. 2, pp. 67–72, 2007.
- [103] T. Tulus, L. Simbolon, S. Sawaluddin, and T. J. Marpaung, “Optimization temperature in the room using air conditioner with finite element methods,” *MATEC Web of Conferences*, vol. 197, 2018.
- [104] S. F. Neves, J. B. L. M. Campos, and T. S. Mayor, “On the determination of parameters required for numerical studies of heat and mass transfer through textiles - Methodologies and experimental procedures,” *International Journal of Heat and Mass Transfer*, vol. 81, pp. 272–282, 2015.
- [105] P. Gibson and M. Charmchi, “The use of volume-averaging techniques to predict temperature transients due to water vapor sorption in hygroscopic porous polymer materials,” *Journal of Applied Polymer Science*, vol. 64, no. 3, pp. 493–505, 1997.
- [106] V. G. Kouznetsova, *Computational homogenization for the multi-scale analysis of multi-phase materials*, no. 2002. 2002.
- [107] W. J. Drugan and J. R. Willis, “A micromechanics-based nonlocal constitutive equation and estimates of representative volume element size for elastic composites,” *Journal of the Mechanics and Physics of Solids*, vol. 44, no. 4, pp. 497–524, 1996.
- [108] Z. Shan and A. M. Gokhale, “Representative volume element for non-uniform microstructure,” *Computational Materials Science*, vol. 24, no. 3, pp. 361–379, 2002.
- [109] S. Bargmann *et al.*, “Generation of 3D representative volume elements for heterogeneous materials: A review,” *Progress in Materials Science*, vol. 96, pp. 322–384, 2018.
- [110] H. Alotaibi, M. Jabbari, and C. Soutis, “A numerical analysis of resin flow in woven fabrics: Effect of local tow curvature on dual-scale permeability,” *Materials*, vol. 14, no. 2, pp. 1–17, 2021.
- [111] G. Ertekin and A. Marmarali, “Heat, air and water vapor transfer properties of circular knitted spacer fabrics,” *Tekstil ve Konfeksiyon*, vol. 21, no. 4, pp. 369–373, 2011.
- [112] Y. Liu and H. Hu, “Compression property and air permeability of weft-knitted spacer fabrics,” *Journal of the Textile Institute*, vol. 102, no. 4, pp. 366–372, 2011.
- [113] J. Orlik, K. Pietsch, A. Fassbender, O. Sivak, and K. Steiner, “Simulation and Experimental Validation of Spacer Fabrics Based on their Structure and Yarn’s Properties,” *Applied Composite Materials*, vol. 25, no. 4, pp. 709–724, 2018.
- [114] Y. Liu, H. Hu, L. Zhao, and H. Long, “Compression behavior of warp-knitted spacer fabrics for cushioning applications,” *Textile Research Journal*, vol. 82, no. 1, pp. 11–20, 2012.
- [115] M. Kyosov, R. A. Angelova, and P. Stankov, “Numerical modeling of the air permeability of two-layer woven structure ensembles,” *Textile Research Journal*, vol.

- 86, no. 19, pp. 2067–2079, 2016.
- [116] L. Wang, K. Zhang, F. I. Farha, H. Ma, Y. Qiu, and F. Xu, “Compressive strength and thermal insulation properties of the 3D woven spacer composites with connected spacer yarn structure,” *Journal of Materials Science*, vol. 55, no. 6, pp. 2380–2388, 2020.
- [117] A. Mountasir, G. Hoffmann, C. Cherif, A. Kunadt, and W. J. Fischer, “Mechanical characterization of hybrid yarn thermoplastic composites from multi-layer woven fabrics with function integration,” *Journal of Thermoplastic Composite Materials*, vol. 25, no. 6, pp. 729–746, 2012.
- [118] D. K. Patel, A. M. Waas, and C. F. Yen, “Direct numerical simulation of 3D woven textile composites subjected to tensile loading: An experimentally validated multiscale approach,” *Composites Part B: Engineering*, vol. 152, no. February, pp. 102–115, 2018.
- [119] Y. Liu and H. Hu, “Finite element analysis of compression behaviour of 3D spacer fabric structure,” *International Journal of Mechanical Sciences*, vol. 94–95, pp. 244–259, 2015.
- [120] K. Lotz, C. Su, Y. Zhang, and Y. Liu, “Structural analysis of three-dimensional mesh fabric by Micro X-ray computed tomography,” *Journal of Engineered Fibers and Fabrics*, vol. 14, 2019.
- [121] F. T. Peirce, 5—*The geometry of cloth structure*, vol. 28, no. 3. 1937.
- [122] J. W. Hearle and W. J. Shanahan, “11—An energy method for calculations in fabric mechanics part I: Principles of the method,” *Journal of the Textile Institute*, vol. 69, no. 4, pp. 81–91, 1978.
- [123] COMSOL, “COMSOL Multiphysics Reference Manual,” Version: COMSOL 5.5, 2018.
- [124] E. E. Swery, R. Meier, S. V. Lomov, K. Drechsler, and P. Kelly, “Predicting permeability based on flow simulations and textile modelling techniques: Comparison with experimental values and verification of FlowTex solver using Ansys CFX,” *Journal of Composite Materials*, vol. 50, no. 5, pp. 601–615, 2016.
- [125] A. Gadeikytė, A. Abraitienė, and R. Barauskas, “Prediction of air permeability coefficient and water-vapor resistance of 3D textile layer,” *Journal of the Textile Institute*, vol. 0, no. 0, pp. 1–9, 2021.
- [126] S. Elgeti and H. Sauerland, “Deforming fluid domains within the finite element method,” *Archives of Computational Methods in Engineering*, p. 4, 2014.
- [127] J. M. Martinez, “Algorithms for solving nonlinear systems of Equations,” *Algorithms for Continuous Optimization. NATO ASI Series (Series C: Mathematical and Physical Sciences)*, vol. 434, pp. 81–108, 1994.
- [128] O. Schenk, K. Gärtner, and W. Fichtner, “Scalable parallel sparse factorization with left-right looking strategy on shared memory multiprocessors,” *Lecture Notes in Computer Science (including subseries Lecture Notes in Artificial Intelligence and Lecture Notes in Bioinformatics)*, vol. 1593, no. 1, pp. 221–230, 1999.
- [129] M. G. Larson and F. Bengzon, *The Finite Element Method: Theory, Implementation, and Applications (Texts in Computational Science and Engineering)*. Springer Heidelberg New York Dordrecht London, 2013.
- [130] A. R. Scott, “Textiles in defence,” in *Handbook of Technical Textiles*, Cambridge:

- Woodhead Publishing and CRC Press LLC, 2000, p. 438.
- [131] “European Standard En 343 : 2003 – Protection Against Rain.” W.L. Gore and associates editorial support Petra Jackisch, Erkrath, Germany.
- [132] M. Relji, J. Stepanovi, B. Lazi, and D. Cerovi, “THE CHANGE OF WATER VAPOUR RESISTANCE OF MATERIALS USED,” *Advanced technologies*, vol. 5, no. 2, pp. 73–78, 2016.
- [133] P. T. Tsilingiris, “Thermophysical and transport properties of humid air at temperature range between 0 and 100 ° C,” *Energy Conversion and Management*, vol. 49, no. 5, pp. 1098–1110, 2008.
- [134] J. L. Monteith and M. H. Unsworth, *Principles of Environmental Physics. Plants, Animals, and the Atmosphere.*, 4th ed. Elsevier Ltd, 2013.
- [135] X. Xiao, A. Long, K. Qian, X. Zeng, and T. Hua, “Through-thickness permeability of woven fabric under increasing air pressure: Theoretical framework and simulation,” *Textile Research Journal*, vol. 87, no. 13, pp. 1631–1642, 2017.
- [136] H. Shen *et al.*, “3D numerical investigation of the heat and flow transfer through cold protective clothing based on CFD,” *International Journal of Heat and Mass Transfer*, vol. 175, 2021.
- [137] M. O. R. Siddiqui, “Geometrical Modelling and Numerical Analysis of Thermal Behaviour of Textile,” Heriot-Watt University, 2015.
- [138] A. Sankauskaite, V. Rubežiene, D. Kubiliene, A. Abraitene, J. Baltušnikaitė-Guzaitiene, and K. Dubinskaite, “Investigation of thermal behavior of 3D PET knits with different bioceramic additives,” *Polymers*, vol. 12, no. 6, 2020.
- [139] A. Nabovati, E. W. Llewellyn, and A. C. M. Sousa, “Through-thickness permeability prediction of three-dimensional multifilament woven fabrics,” *Composites Part A: Applied Science and Manufacturing*, vol. 41, no. 4, pp. 453–463, 2010.
- [140] S. Sundaramoorthy, P. K. Nallampalayam, and S. Jayaraman, “Air permeability of multilayer woven fabric systems,” *Journal of the Textile Institute*, vol. 102, no. 3, pp. 189–202, 2011.
- [141] H. Özdemir, “Thermal comfort properties of clothing fabrics woven with polyester/cotton blend yarns,” *Autex Research Journal*, vol. 17, no. 2, pp. 135–141, 2017.
- [142] M. Venkataraman, J. Militký, R. Mishra, and S. Jandová, “Unconventional measurement methods and simulation of aerogel assisted thermoregulation,” *Journal of Mechanical Engineering*, vol. 5, no. Specialissue5, pp. 62–96, 2018.
- [143] Y. Sun and W. J. Jasper, “Numerical modeling of heat and moisture transfer in a wearable convective cooling system for human comfort,” *Building and Environment*, vol. 93, no. P2, pp. 50–62, 2015.
- [144] K. Ghali, N. Ghaddar, B. Jones, and N. Awar, “Modeling of heat and moisture transport by periodic ventilation of cotton fibrous media,” *Proceedings of the National Heat Transfer Conference*, vol. 2, no. 2002, pp. 1245–1254, 2001.
- [145] R. Barauskas, J. Baltušnikaitė, A. Abraitene, and D. Grinevičiute, “Experimental investigations and finite element model of heat and moisture transfer in multilayer textile packages,” *Fibres and Textiles in Eastern Europe*, vol. 95, no. 6, pp. 112–118, 2012.

CURRICULUM VITAE

Personal information:

First name: Aušra

Surname: Gadeikytė

Date of Birth: 13th of September 1990

Place of Birth: Notėnai, Skuodo r., Lithuania

E-mail: ausra.gadeikyte@ktu.lt

Education:

2015–2020 Doctoral Studies in Natural Sciences, Informatics (N 009), Department of Applied Informatics, Faculty of Informatics, Kaunas University of Technology.

2013–2015 Master of Science Degree in Applied Mathematics, Faculty of Mathematics and Natural Sciences, Kaunas University of Technology.

2009–2013 Bachelor of Science Degree in Applied Mathematics, Faculty of Fundamental Sciences, Kaunas University of Technology.

Work experience:

07/01/2017–Present Lector at Kaunas University of Technology.

11/02/2016–06/30/2017 Assistant at Kaunas University of Technology.

02/01/2016–06/30/2016 Teaching practice at Kaunas University of Technology.

04/14/2015–12/31/2015 Project engineer (PP41/1507) at the Institute of Materials Science of Kaunas University of Technology.

12/16/2013–03/31/2015 Project specialist (VP131V029) at the Institute of Materials Science of Kaunas University of Technology.

Research interests:

Mathematical modeling of heat and mass transfer through textile structures, tensile tests.

ACKNOWLEDGEMENTS

The author of the dissertation would like to express gratitude to her supervisor Prof. Habil. Dr. Rimantas Barauskas for his assistance and valuable advice during the PhD studies as well as his patience, friendly guidance in reading abstracts, articles, and the final thesis.

In addition, the author of the dissertation would like to thank her family and friends for their support throughout the years of studies.

PUBLICATIONS RELATED TO THE DISSERTATION

In publications indexed in the Web of Science with Impact Factor

1.[S1; GB; OA] **Gadeikytė, Aušra**; Abraitienė, Aušra; Barauskas, Rimantas. Prediction of air permeability coefficient and water-vapor resistance of 3D textile layer // Journal of the Textile Institute. Abingdon: Taylor & Francis. ISSN 0040-5000. eISSN 1754-2340. 2021, vol. 00, p. 1-9. DOI: 10.1080/00405000.2021.1883237. [Science Citation Index Expanded (Web of Science); Scopus] [IF: 1,239; AIF: 2,536; IF/AIF: 0,488; Q2 (2019, InCites JCR SCIE)] [Field: N 009]

2.[S1; GB] Barauskas, Rimantas; Sankauskaite, Audrone; Rubeziene, Vitalija; **Gadeikyte, Ausra**; SkurkytePapieviene, Virginija; Abraitiene, Ausra. Investigation of thermal properties of spacer fabrics with phase changing material by finite element model and experiment // Textile research journal. London: SAGE. ISSN 0040-5175. eISSN 1746-7748. 2020, vol. 90, iss. 15-16, p. 1837-1850. DOI: 10.1177/0040517520902063. [Science Citation Index Expanded (Web of Science); Scopus] [IF: 1,926; AIF: 2,536; IF/AIF: 0,759; Q1 (2019, InCites JCR SCIE)] [Field: N 009, T 008]

In publications indexed in the Web of Science without Impact Factor

1. [S1; LT; OA] **Gadeikytė, Aušra**; Barauskas, Rimantas. Investigation of influence of forced ventilation through 3D textile on heat exchange properties of the textile layer // Journal of Measurements in Engineering. Kaunas: JVE International. ISSN 2335-2124. eISSN 2424-4635. 2020, Vol. 8, iss. 2, p. 1-7. DOI: 10.21595/jme.2020.21555. [Emerging Sources Citation Index (Web of Science); Scopus; DOAJ] [Field: N 009]

2. [P1a; CH] **Gadeikytė, Aušra**; Barauskas, Rimantas. Computer simulation of heat exchange through 3D fabric layer // Numerical methods and applications: 9th international conference, NMA 2018: revised selected papers / Nikolov G., Kolkovska N., Georgiev K. (eds). Cham: Springer, 2019. ISBN 9783030106911. eISBN 9783030106928. p. 392-399. (Lecture notes in computer science, ISSN 0302-9743, eISSN 1611-3349; Vol. 11189). DOI: 10.1007/978-3-030-10692-8_44. [Conference Proceedings Citation Index - Science (Web of Science); Scopus] [Field: N 009]

Presentation of research results at the international conferences

1. [T2; GB] **Gadeikytė, A.**; Barauskas, R. Numerical simulation of air permeability coefficient of 3D textile layer // COMSOL Conference 2019 Cambridge, September 24-26. [Cambridge]: [s.n.]. 2019, p. [1]. [Field: N 009]

2. [T2; BG] **Gadeikytė, Aušra**; Barauskas, Rimantas. Computer simulation of heat exchange through 3D fabric layer // Numerical methods and applications: 9th international conference, NM&A'18, August 20-24, 2018, Borovets, Bulgaria: program, abstracts, participants. Sofia : Sofia University "St. Kliment Ohridski". 2018, p. 47- 48. [Field: N 009]

3. [T1e; LT] **Gadeikytė, Aušra**; Barauskas, Rimantas. Modelling and simulation of heat and moisture transport in 3D fabric layer // Advanced materials and technologies: book of abstracts of the 19th international conference school, 27-31 August 2017, Palanga, Lithuania. Kaunas: Kaunas University of Technology. ISSN 1822-7759. 2017, P88, p. 115. [Field: N 009]

4. [T1e; LT] **Gadeikytė, Aušra**; Barauskas, Rimantas. Finite element analysis of coupled heat transfer and water vapor exchange in 3D textile layer // Mathematical modelling and analysis: 22nd international conference, May 30–June 2, 2017, Druskininkai, Lithuania:

abstracts. Vilnius: Technika, 2017. ISBN 9786094760228. eISBN 9786094760211. eISSN 2351-5740. p. 17. [Field: N 009]

List of other publications and conferences not related to the dissertation

1. [S1; GB] Antanavičiūtė, Ieva; Šimatonis, Linas; Ulčinas, Orestas; **Gadeikytė, Aušra**; Abakevičienė, Brigita; Tamulevičius, Sigitas; Mikalayeva, Valeryia; Skeberdis, Vytenis Arvydas; Stankevičius, Edgaras; Tamulevičius, Tomas. Femtosecond laser micro-machined polyimide films for cell scaffold applications // Journal of tissue engineering and regenerative medicine. Chichester: John Wiley & Sons. ISSN 1932-6254. eISSN 1932-7005. 2018, vol. 12, iss. 2, p. 760-773. DOI: 10.1002/term.2376. [Science Citation Index Expanded (Web of Science); Scopus; MEDLINE] [IF: 3,319; AIF: 4,442; IF/AIF: 0,747; Q2 (2018, InCites JCR SCIE)] [Field: N 011, T 007, T 008]

2. [T2; FR] Abakevičienė, Brigita; Lukauskas, Mantas; Norkus, Skirmantas; **Gadeikytė, Aušra**; Jucius, Dalius; Lazauskas, Algirdas; Grigaliūnas, Viktoras. Microtensile testing of fluoropolymer films // E-MRS Spring Meeting 2017, May 22-26, Strasbourg, France. Strasbourg: European Materials Research Society. 2017, W.P13.0, p. 1. [Field: N 002, T 008]

Appendix 1. The case study of *Model 1_a*

Model 1_a represents a one-layer woven structure with a structural density of 22/15. Fig. 1. illustrates the 3D air flow through the thickness (z-direction) of RVE. The red arrows represent the 3D vector field of velocity for the Navier–Stokes and Brinkman flow. The length of the arrows is proportional to the magnitude of velocity quantity [123]. On the right side, there is depicted a grid of the RVE that consists of 27,075 elements on the air domain and 12,322 elements on the textile domain. The minimum element quality of all domains is 0.1006, and the average element quality is 0.6484. The minimum and average element quality of the textile domain is 0.1006 and 0.6034, respectively, while the air domain, 0.189 and 0.6688. The legend depicts the air velocity (air permeability coefficient), mm/s.

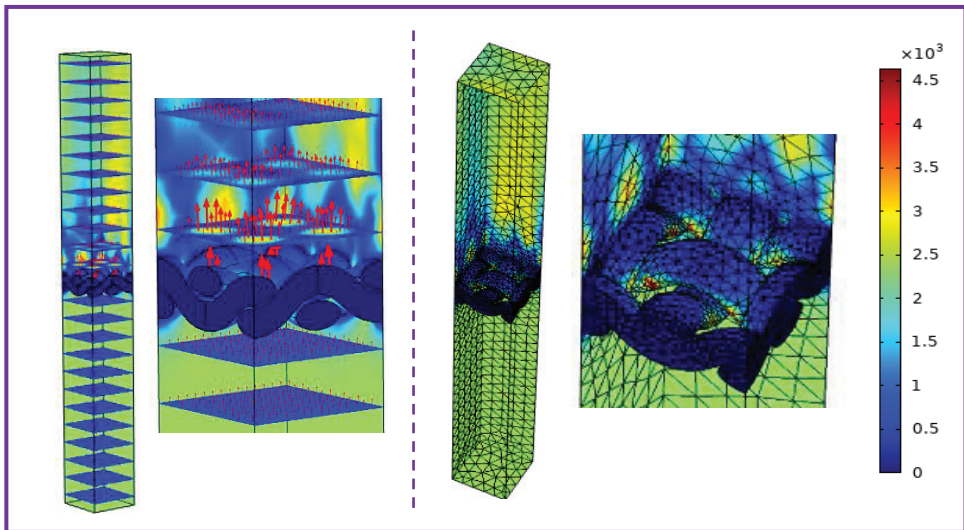


Fig. 1. The 3D velocity field and mesh of the *Model 1_a*

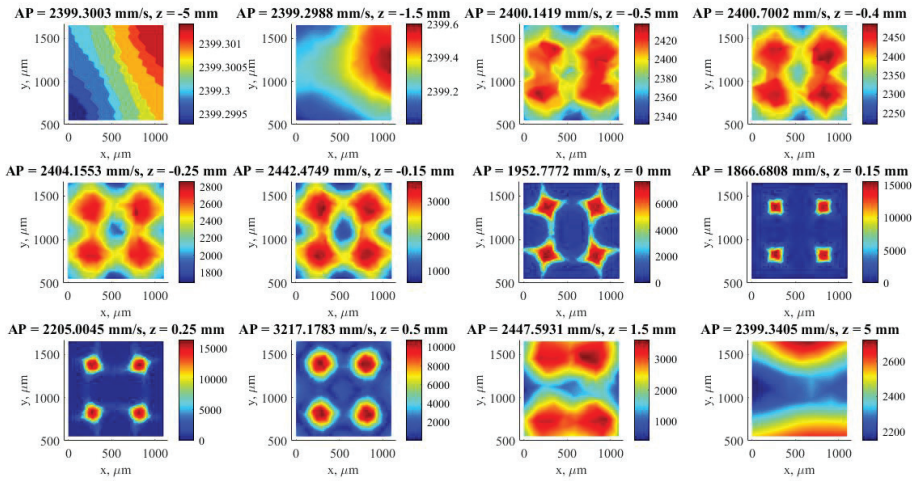


Fig. 2. The 2D velocity distribution of the *Model 1_a* at a fixed height (z position)

Fig. 2. portrays the air flow distribution through the thickness, AP indicates the average velocity of the cross-section at different z positions (height). Fig. 3. represents the average AP value, using 0.25 mm step in the z -direction, average pressure, and inner errors (residual) plot.

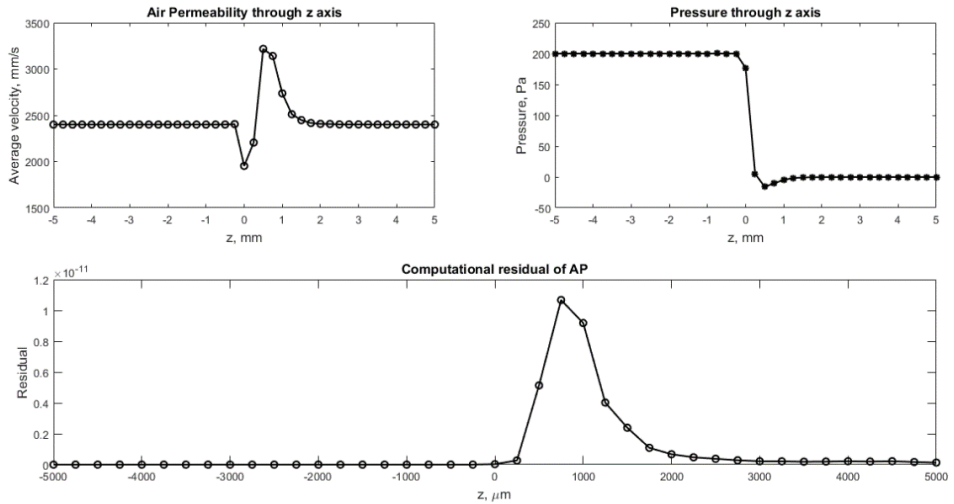


Fig. 3. The average air flow, pressure, and residual of the *Model 1_a* at different height (z position)

UDK 004.94+677.017.56](043.3)

SL344. 2022-02-14, 15,5 leidyb. apsk. I. Tiražas 14 egz. Užsakymas 27.
Išleido Kauno technologijos universitetas, K. Donelaičio g. 73, 44249 Kaunas
Spausdino leidyklos „Technologija“ spaustuvė, Studentų g. 54, 51424 Kaunas

